UNIVERSITA` DEGLI STUDI DI MILANO-BICOCCA
Facoltà di Scienze Matematiche, Fisiche e Naturali
Scuola di Dottorato in Biologia

Investigating the biological activity of proteins immobilized on colloidal nanoparticles

Tutor: Prof. Paolo TORTORA
Cotutor: Dr. Davide PROSPERI

Tesi di dottorato di:
Elisabetta GALBIATI
Matr. 076879

Ciclo XXVI

A Michele e Tommaso

List of abbreviations

ATF	Amino terminal fragment
AuNP	Gold nanoparticle
Au-peptide NP	Gold nanoparticles functionalized with peptide
AuScr	Gold nanoparticles functionalized with scrambled peptide
AuU11	Gold nanoparticles functionalized with U11 peptide
BSA	Bovine serum albumin
CUT	Cutinase
CUT-U11	Cutinase fused with U11
DAPI	4′,6-diamidino-2-phenylindole
DiD	4′,6-diamidino-2-phenylindole
DLS	Dynamic light scattering
DMF	Dimethyl formamide
DMSO	Dimethyl sulfoxide
DMEM	Dulbecco's modified eagle's medium
DTT	Dithiothreitol
EDBE	(2,2-(ethylenedioxy)bisethylamine
EDC	1-Ethyl-3-(3-dimethylaminopropyl)carbodiimide
EDTA	Ethylenediaminetetraacetic acid

EGFR	Epidermal growth factor receptor
EPR	Enhanced permeation and retention effect
FACS	Fluorescence Activated Cell Sorting
FDA	Food and drug Administration
FBS	Fetal Bovine Serum
Fe_3O_4	Magnetite
γ-Fe_2O_3	Maghemite
FITC	Fluorescein isothiocyanate
FTIR	Fourier Transform Infra-Red spectra
GFD	Growth factor domain
HALO	Haloalkane dehalogenase
HALO-U11	Haloalkane dehalogenase fused with U11 peptide
HER2	Human Epidermal growth factor receptor 2
His-tag	Oligohistidine affinity tag
HRP	Enzyme horseradish peroxidase
HSA	Human Serum Albumin
IPTG	Isopropil-β-D-1-tiogalattopiranoside
mAb	Monoclonal antibody
MAPK	Mitogen-activated protein kinase
MFN	Magneto-fluorescent nanoparticles
MNC	Magneto nanocristals
MNP	Multifunctional-nanoparticles
MNP-CUT	Cutinase functionalized nanoparticles
MNP-CUT-U11	Cutinase-U11 functionalized nanoparticles
MNP-H11	HALO-U11 functionalized nanoparticles
MNP-U11	U11 peptide functionalized nanoparticles
MRI	Magnetic resonance imaging
MTT	3-(4,5-dimethylthiazol-2-yl)-2,5-diphenyltetrazolium bromide
NHS	N-hydroxysuccinimide
NPs	Nanoparticles
NTA	Nitrilotriacetic acid
PBS	Phosphate buffer solution
PEG	Poly ethylene glycol

PMA	Poly(isobutylene-alt-maleic anhydride
RT	Room temperature
SBB	Sodium borate buffer
ScFv	Single-chain variable fragment
SDS	Sodium dodecyl sulphate
SSMFN	ScFv-SNAP functionalized nanoparticles
TEM	Trasmission electron microscopy
TMNP	TZ functionalized nanoparticles
TZ	Trastuzumab
uPA	Urokinase plasminogen activator
uPAR	Urokinase plasminogen activator receptor
U11	Eleven amino acid fragment: SNKYFSNIHW

Table of contents

Abstract

Currently, nanoparticles (NPs) play an increasing role in biomedical research and clinical applications, thanks to their peculiar optical, physical and chemical properties. A great challenge in nanodiagnostics is the development of new nano-sized devices aimed to optimize the detection of primary cancer cells and metastases. The design of ideal nanoconjugates, containing bioactive ligands specific for targeting cancer cell, requires optimization of fundamental parameters involved in conjugation reactions: both functional conformation and proper orientation must be preserved. This characteristic determines bioactivity, avidity and targeting efficiency of the functionalized NPs.

In the context of this thesis, different conjugation strategies were analyzed, focusing on the improvement of the biological activity of the immobilized protein. First of all, trastuzumab-functionalized pegylated iron oxide nanoparticles were synthetized and protein conformation analyzed using FTIR spectroscopy. This technique provides direct evidence of the extent of native structure preservation of the immobilized protein, in dependence of the conjugation strategy. Moreover, the possibility to control the ligand/peptide orientation on the nanoparticle surface is a fundamental step to optimize receptor recognition. An elegant strategy involves the use of fusion proteins containing a small enzyme (defined “capture protein”) capable of irreversibly cross-coupling with a suicide inhibitor anchored to the solid surface. Three different approaches have been analyzed: SNAP (O_6-alkylguanine-DNA-transferase), HALO (haloalkane dehalogenase) and cutinase enzymes fused with specific proteins or small peptides for the selective targeting of breast cancer cells. Although targeted therapy with monoclonal antibody, or small portion of these proteins, is a major treatment currently employed in many cancers, the use of short peptides as targeting moieties of tumor receptors have several

advantages. The possibility to exploit gold nanoparticles (AuNPs) properties, to form a self-assembled monolayer on AuNPs surfaces, allows to increase ligand-receptor target affinity/recognition. The capability of all these bioconjugation methods to specifically and selectively target breast cancer cells, was confirmed by flow cytometry (FACS), confocal laser scanning microscopy and transmission electron microscopy (TEM).

Introduction

1. Nanomedicine

In recent years, nanoparticles (NPs) have played an increasing role in biomedical research and clinical applications. The use of nanotechnology is gaining interest in biology and medicine and the unique chemical/physical properties of nanomaterials are being exploited in the field of nanomedicine for basic research investigations, as well as in clinical practice for both diagnosis and treatment of several diseases. Possible applications include drug delivery nanosystems and cell targeting, magnetic resonance imaging (MRI) contrast enhancement, gene therapy, biomarker identification, targeted hyperthermia and many others (**Fig. 1**).[1-5]

The field of nanomedicine exploits the properties and physical characteristics of nanomaterials for the diagnosis and treatment of diseases at the molecular level.

1.1 Nanomaterials for in vivo investigation

A handful of nanomaterials are being studied in clinical trials or have already been approved by the FDA for use in humans,[7-9] and several proof-of-concept studies of nanomaterials in cell culture and small animal models for medical applications are underway (**Fig. 2**).[10-12] A number of these nanomaterials are designed to target tumors in vivo and are intended for use either as drug carriers or as contrast agents for molecular imaging. Nanomaterials infused into the bloodstream can accumulate in tumors owing to the “enhanced permeability and retention” (EPR) effect, as the vasculature of immature tumors presents fenestrations with pores ranging from 200 to 600 nm, allowing for the extravasation of nanoparticles from the blood into the tumor tissue.[13]

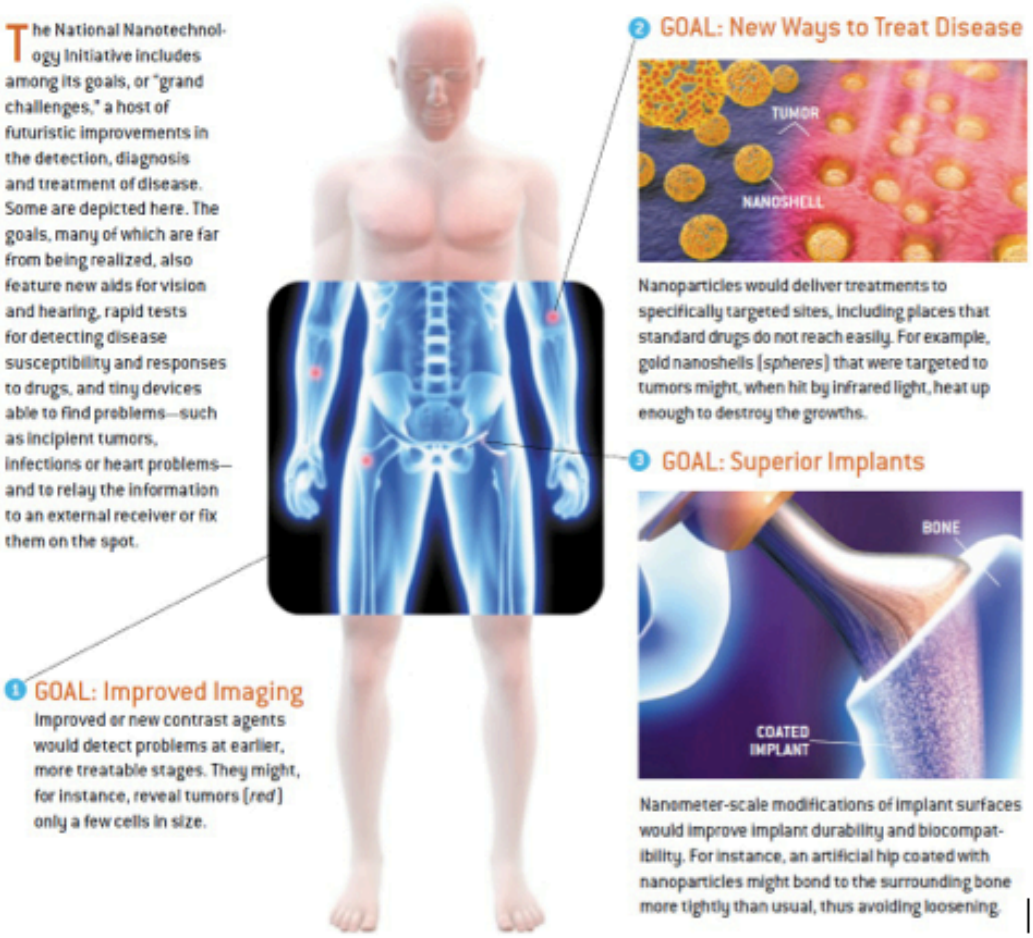

Fig. 1: Potential of nanomedicine.[6]

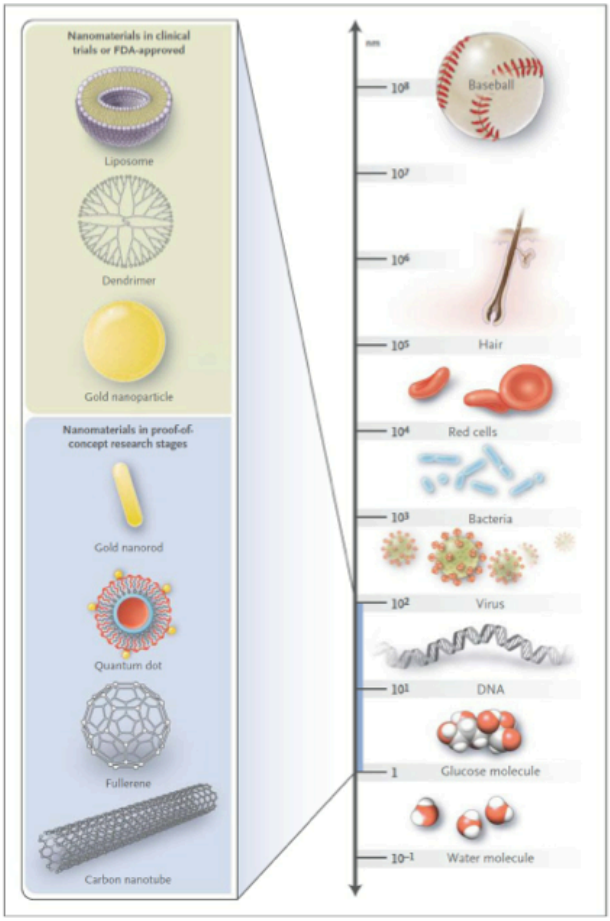

Fig. 2 Nanomaterials commonly used in medicine. Liposomes contain amphiphilic molecules, which have hydrophobic and hydrophilic groups that self-assemble in water. Dendrimers are branched nanostructures; each terminus contains reactive chemical functional groups that allow the addition of multiple monomers to increase the size of the nanostructure. Gold nanoparticles are solid metal particles that are conventionally coated with drug molecules, proteins, or oligonucleotides. Quantum dots are semiconductor nanocrystals endowed with strong photoluminescence usually consisting of a core-shell structure (*e.g.*, CdSe coated with zinc sulfide with a stabilizing molecule and a polymer layer coated with a protein). Fullerenes and carbon nanotubes have only carbon-to-carbon bonds. These nanostructures are commonly named according to the number of carbon atoms that form the structure (*e.g.*, a C60 fullerene contains 60 carbons).[1]

The infusion of antineoplastic drugs exploiting nanomaterials as carriers results in an increased accumulation of drugs at the tumor, as compared with conventional administration. In addition, the high ratio of surface area to volume favors high surface loading of therapeutic agents; when using organic nanomaterials, their hollow or porous

core allows the encapsulation of hundreds to thousands of drug molecules within a single carrier nanoparticle. As the carrier degrades to some extent, the drug molecules are released, and the rate of degradation can even be controlled and finely tuned according to the polymer or coating composition. These delivery nanovehicles can also be coated with polymers, such as polyethylene glycol, to increase their half-life in the blood circulation, to prevent opsonins from adhering to the nanomaterial surface, and reduce the rapid metabolism and clearance of the nanoparticulate. Moreover, the use of nanomaterials for drug delivery may minimize adverse effects by preventing the nonspecific uptake of therapeutic agents from healthy tissues.[14,15] Nanoparticles are further attractive as sensitive contrast agents for cancer imaging. For instance, in magnetic nanoparticle-enhanced MRI, there is a contrast between tissues which captured superparamagnetic iron oxide nanoparticles and those which don't have, owing to a difference in the precession frequency of the water protons in proximity of paramagnetic nanodipoles. The use of magnetic nanoparticles as contrast agents for MRI, as compared with conventional MRI, was associated with substantial increases in both diagnostic sensitivity (90.5% vs. 35.4%) and specificity (97.9% vs. 90.4%) in the detection of metastatic tumors.[18] Magnetic nanoparticles are also being studied in clinical trials for imaging of hyperplasia, adenoma, and more specifically, primary lung cancer, in which a decrease in the function of the reticuloendothelial system affects the amount of nonspecific phagocytic uptake.

Nanoparticles can be also employed as labels for measuring molecules of interest in biological samples. To this aim, nanomaterials can be used to either simplify/amplify the readout or to lower substantially the detection threshold of a diagnostic device. Nanoparticles are used in lateral-flow in vitro diagnostic assays (LFA), such as the urine pregnancy test, for detecting protein markers (*e.g.*, human chorionic gonadotropin [hCG]).[16] This allows an easier readout of the signal at the point of care without the need for a more complex instrumentation. A number of FDA-approved LFAs for measuring human immunodeficiency virus (HIV), malaria, and cardiac markers are also available. Although this technique is simple to use and can be carried out rapidly (one complete assay takes less than 1 h), it suffers from poor detection sensitivity (millimolar to micromolar, depending on the biomarker). Gold nanoparticles are also used in high throughput genomic detection devices without the need for polymerase chain reaction (PCR) amplification but with a sensitivity on the same order of that of PCR-based assays

(**Fig. 3**).[17] This technology has been approved by the FDA for genetic screening to determine drug sensitivity and to detect genetic mutations. This approach does not suffer from the problems often associated with conventional fluorescent probes for microarray labeling, such as photobleaching (a loss of signal after exposure to light), and can detect multiple markers with a high sensitivity (95%) and low detection threshold (down to 10^{-18} M). A modification of this approach called the bio-barcode assay is currently being validated for the detection of proteins associated with prostate cancer.[18]

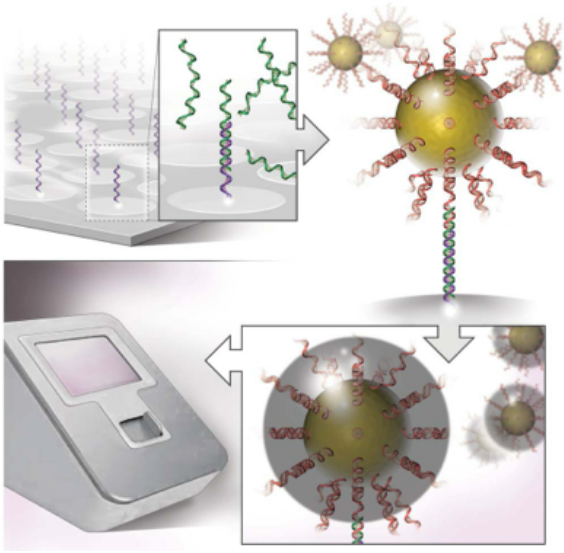

Fig. 3 Nanomaterials used as labels to amplify detection signals in diagnostic devices. Nanomaterials such as gold nanoparticles can be coated with biorecognition molecules to target either a patient's DNA or a protein sample. In this picture, gold nanoparticles are coated with a complementary oligonucleotide (single-stranded DNA) that recognizes the variant gene sequence captured on a surface. Once nanoparticles are bound to the surface, the detected signal (*e.g.*, RAMAN absorption) associated to bimolecular counterparts is amplified by means of a silver nitrate reduction reaction. This technique, commonly referred to as Surface Enhanced Raman Scattering (SERS),[19] has been reported to have sensitivity equivalent to that of the polymerase chain reaction assay for genic analysis.[1]

1.2 Nanomaterials for theranostics

The term "theranostic" defines the combination of diagnostic and therapeutic capabilities into a single agent, and identifies the ongoing efforts in clinics to develop more specific and personalized therapies for various diseases.[20] The rationale arose

from the fact that several diseases are broadly heterogeneous and all existing treatments are effective for only limited patient subpopulations and at selective stages of disease development. The close marriage between diagnosis and therapy could provide therapeutic protocols that are more specific to individuals and, therefore, more likely to offer improved prognoses. The emergence of nanotechnology has offered an unprecedented opportunity to draw diagnosis and therapy closer. Nanoparticle-based imaging and therapy have been investigated separately, and understanding of them has now evolved in nanoplatforms that can codeliver therapeutic and imaging functions. These nanoparticles possess unique optical or magnetic properties and have been previously studied in the imaging setting, and are achieving successful outcomes under several circumstances. These have laid the foundations for the current applications, since the imaging probes can be easily upgraded when loaded with appropriate therapeutics. It has been shown that various kinds of therapeutics, including those based on small molecules, proteins and nucleotides can be conveniently tethered onto nanoplatforms. The large capacity even allows for the loading of a second or third functionality, a feature that encourages the formation of an all-in-one nanosystems with comprehensive features (**Fig. 4**).

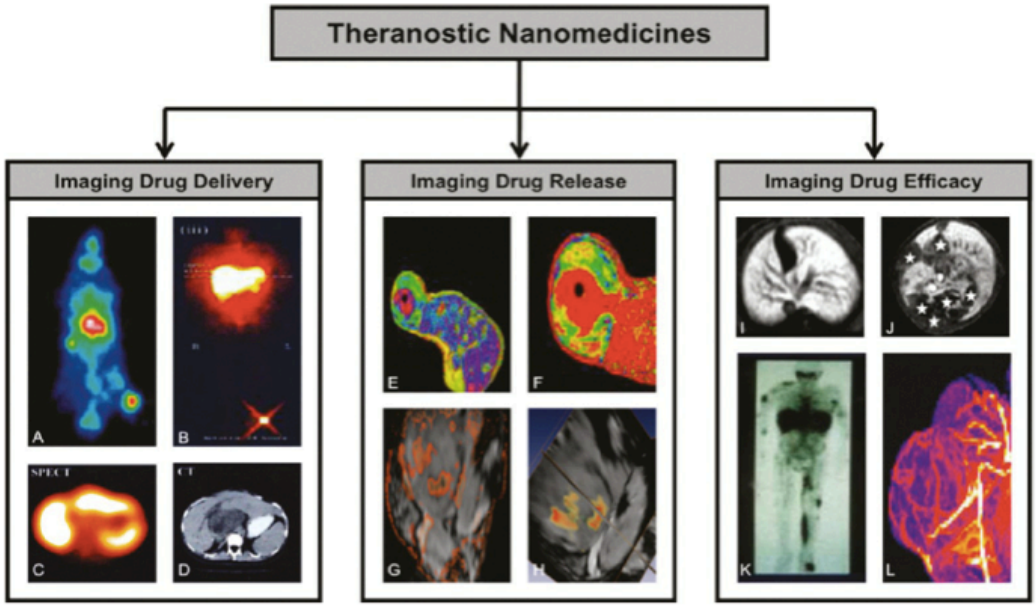

Fig. 4 Applications of theranostic nanomedicine formulations. Theranostic nanomedicines can be applied for various different purposes, most notably for imaging drug delivery (A-D), drug release (F-H), and drug efficacy (I-L). (A) Gamma camera imaging of biodistribution and tumor accumulation of a passively tumor-targeted iodine^{131}-labeled HPMA copolymer in a Copenhagen rat bearing a Dunning AT1 tumor in its right hind limb. (B) Gamma camera image showing effective active drug targeting to the liver using an iodine^{123}-labeled galactosamine-modified HPMA copolymer containing doxorubicin *(i.e.,* PK2) in a patient suffering from hepatocellular carcinoma. (C,D) Functional SPECT imaging (C) of the tumor and liver localization of iodine^{123}-labeled PK2 combined with anatomical CT imaging (D), exemplifying that the majority of the liver-targeted polymeric prodrug does not localize to the (dark) tumorous region in the middle of the SPECT and CT image. (E,F) MR-based visualization and quantification of manganese and doxorubicin release from temperature-sensitive liposomes (TSL). The color-coded Mn2þ-enhanced T_1 map obtained at 45 min after the i.v. injection of TSL into a rat bearing a preheated fibrosarcoma tumor is shown in (E). (F) Amount of released doxorubicin calculated and correlated on a pixel-by-pixel basis from the image in (E), exemplifying release in the periphery of the tumor. (G,H) Release of Gd-DTPA from PLGA-based nanoparticles containing iron oxide, Gd-DTPA and 5-FU. (G) Subtraction image of precontrast minus postcontrast T_1-map (in red; showing Gd-DTPA release; note that the Gd-DTPA-signal is quenched in close proximity to iron oxide), overlaid on a T_2*-weighted image, showing the tumor accumulation of the particles (in black). (H) A 3D image depicting T_2*-weighted signals overlaid with quantitative T_1 values (yellow, 50 μM; red, 500 μM), enabling quantification of drug release. (I,J) Accumulation of Gd-labeled polypropylene diaminobutane dendrimers in a healthy mouse liver (I) and in a liver containing several metastatic lesions (J), exemplifying the suitability of these particles to visualize liver metastases. (K) Biodistribution of indium^{111}-labeled PEGylated liposomes in a Kaposi sarcoma patient. Localization to a large tumorous mass in the lower left leg and to several metastatic lesions can be clearly observed, exemplifying the possibility of such formulations for predicting and monitoring treatment responses. (L) Maximal intensity projection of an MR angiography scan of a Dunning AT1 tumor obtained at 30 min after the i.v. injection of a 25 kDa sized gadolinium-labeled HPMA copolymer. Such MR angiography-based approaches are considered to be highly useful for noninvasively assessing the efficacy of nanomedicine based antiangiogenic interventions.[20]

1.3 Colloidal nanoparticles in nanomedicine

Various types of colloidal nanoparticles are available, including quantum dots (QDs), magnetic NPs (MNPs), gold NPs (AuNPs) and silica NPs (SiNPs) which could be used for biological and medical applications.

QDs exibit extraordinary photostable fluorescent signals and resistance to photobleaching. These NPs consist of a typical core/shell structure composed of heavy metals;[21-23] in many cases QDs include a cadmium selenide or cadmium sulfide core, coated with a zinc sulfide shell. It is possible to modulate their size or change the nature of their metal core in order to vary their emission area in the range 450-850 nm. They are generally synthesized in high-boiling non-polar organic solvents. Thus, to be solubilized in

aqueous buffers, their hydrophobic surface ligands must be replaced by suitable amphipathic ligands.

Superparamagnetic iron oxide NPs are typically composed of magnetite (Fe_3O_4) or maghemite (γ-Fe_2O_3) nanocrystals; they have a spinel crystal structure with oxygen ions forming a close-packed cubic lattice and iron ions located at interstices. MNPs have potential applications in the biomedical field, including use as contrast agents for magnetic resonance imaging (MRI), for their ability to decrease T_2 relaxation time of water protons, drug delivery systems (DDS), magnetic bioseparations and magnetic force-based heating mediators for hyperthermia.[24-28]

AuNPs and gold nanorods (AuNRs) are under exploration in biomedicine since gold has been approved for optical detection and thermal therapy of tumors. These NPs are rapidly synthesized and their surface can be easily functionalized with targeting molecules and ligands by thiol chemistry.[29,30] Many surfactants have been described in literature, including citric acid and polyethylene glycol (PEG), which are able to maintain the post-synthetic colloidal stability in aqueous physiological solutions.

Proper silica nanoparticles (SiNPs) design and functionalization yields particularly stable colloids, even under physiological conditions, and provides them with multiple functions. A suitable choice of dyes could be coupled with SiNPs trough different synthetic strategies yielding a very bright and stable nanoconstruct. Silica-based NPs have a dominant role because of their fundamental characteristics, such as size (generally from 5 to 1000 nm), unique optical properties, low density, adsorption capacity, capacity for encapsulation and low toxicity.[31] Consequently, intensive research has been performed to use SiNPs in diverse biomedical applications for diagnosing and controlling diseases, identifying and correcting genetic disorders and, most importantly, increasing longevity. Thus, SiNPs offer considerable advantages and have opened new avenues of biomedical research in numerous leading edge applications, such as biosensors,[32] controlled drug release and cellular uptake.[33]

2. Innovative role of colloidal nanoparticles in biology and medicine

Nanomaterials are now being designed to aid the transport of diagnostic or therapeutic agents through biological barriers, to gain access to specific functions, to

mediate molecular interactions, and to detect molecular changes in a sensitive and high throughput manner. In contrast to atoms and macroscopic materials, nanomaterials have a high ratio of surface area to volume as well as tunable optical, electronic, magnetic, and biological properties. In addition, they can be engineered to have different sizes, shapes, chemical compositions, surface chemical characteristics, and hollow or solid structures. These properties are being incorporated into a new generation of drug delivery vehicles, contrast agents, and diagnostic devices, some of which are currently undergoing clinical trials or have been approved by the Food and Drug Administration (FDA) for use in humans; others are in the proof-of-concept stage in research laboratories.

Nanomaterials generally consist of metal atoms, nonmetal atoms, or a mixture of metal and nonmetal atoms, commonly referred to as metallic, organic, or semiconducting nanostructures, respectively. The surface of nanomaterials is usually coated with polymers or biorecognition molecules to achieve an improved biocompatibility and selective binding with biological molecules. The final size, composition, shape (spherical, rod-like, star-like, wires, octahedral, cubic, etc.) and morphological characteristics (full, hollow, porous, etc.) of nanomaterials depend on the salt and surfactant additives, reactant concentrations, reaction temperatures, and solvent conditions used during their synthesis. A common feature of all nanomaterials is their large ratio of surface area to volume, which may be orders of magnitude greater than that of macroscopic materials. For example, cutting a 1 cm cube into 10^{21} cubes that are each 1 nm on a side will result in the same overall volume and mass, but the surface area will be increased by a factor of 10 million. Thus, the advantage of using nanomaterials as carriers is that their surface can be coated with a large number of active molecules, which can be delivered using only small volumes of formulation.[34]

Colloidal nanoparticles may offer unique binding opportunities thanks to their inorganic surfaces, which enable ion complexation, metal coordination, and electrostatic or van der Waals interactions. The designing of high quality colloidal nanoparticles, offers promising new tool for the development of a novel generation of diagnostic and therapeutic agents for biosensing, preclinical investigation, and clinical care.[35]

A list of colloidal nanoparticles suitable for conjugation with protein and other biomolecules is in **Table 1.**

Table 1 Selected colloidal nanoparticles for biomedical application.

Type of nanoparticle	Typical size range (nm)	Properties	Benefits	Applications
Metallic Au, Ag, Cu	3–100	Tunable surface plasmon resonance as a function of composition, size and shape; surface enhanced Raman scattering; stable covalent bond with thiols	Facile synthesis over a broad range of sizes and shapes (e.g., rods, spheres, core–shell); easy functionalization; biocompatibility; low cytotoxicity *in vivo* and *in vitro*; higher intensity in dark-field microscopy compared to fluorescent labels	Cell labeling; gene therapy; nucleotide delivery; *in vitro* diagnostics; Alzheimer detection; cell surface detection
Magnetic Fe, Mn, Ni, Co, and their oxides	5–200	Ferromagnetic and superparamagnetic	Biocompatibility; low cytotoxicity; high level accumulation in the target tissue	MR images; recyclable biocatalyst; gene therapy; hyperthermia
Quantum dots III-V (GaN, GaP, GaAs, InP, or InAs) or II-VI (ZnO, ZnS, CdS, CdSe, or CdTe) semiconductors	2–10	Tunable and stable emission; narrow emission band and broad excitation in a broad range of wavelengths	Size-dependent fluorescence; 10–100 times brighter and 100–1000 times more stable against photobleaching than organic dyes; large interval of emission from UV to mid-IR	Sensors; *in vivo* imaging
Upconvertion nanocrystals Ln-doped fluoride nanocrystals, rare earth-doped oxidic nanomaterials	30–100	Inert host material doped with optically active sensitizer and activator ions	Intense luminescence when excited by near-IR radiation; high tissue penetration capability	Cellular imaging, biosensing, multiphoton analysis in living cells; near IR-based *in vivo* tracking; high resolution; real-time images of transplanted cells
Silica SiO_2	5–1000	Optical properties; low density; adsorption capacity	Capability of molecule encapsulation; biocompatibility and low toxicity	Drug/gene delivery; controlled drug release; bioanalysis; fluorescence imaging; biosensors; enzyme supporters

2.1 Drug delivery

NPs are found to be attractive platforms for the delivery of increasingly potent, selective, and multifunctional anti-cancer drug conjugates.[36,37] Drug delivery systems (DDSs) can improve several crucial properties of ‘‘free’’ drugs, such as solubility, in vivo stability, pharmacokinetics, and biodistribution, enhancing their efficacy. Moreover, nanoparticles can provide effective carriers for biomolecules such as DNA, RNA, or proteins, protecting these materials from degradation and transporting them across the cell-membrane barrier. Colloidal NPs functionalized by tumor therapeutic agents such as paclitaxel,[37,38] anthracycline,[39] doxorubicin were proved to be efficiently delivered into

cancer cells.[40-45] For successful delivery, carriers must: (a) form condensed complexes with biomolecules, (b) facilitate penetration of the cell membrane after complexation, and (c) unload their payloads inside cells.

Two approaches to serve this purpose are ‘‘passive’’ and ‘‘active’’ targeting. The passive targeting route takes advantage of the biological function of the reticuloendothelial system (RES), a cell family of the immune system comprising circulating monocytes, bone marrow progenitors and tissue macrophages, which are deputed to the first clearance activity in mammalian organisms. Once unprotected particles are immersed in the blood stream, an array of plasma proteins recognizes them as invading entities and immediately adsorb on their surface. The parameters affecting the extent of opsonization are essentially related to the physical properties of the nanoparticle surface, including size, shape, charge and aggregation state. Large objects are rapidly cleared and highly charged particles have a tendency to attract opsonins. Consequently, nanoparticles coated by these plasma proteins are rapidly endocytosed by the RES cells, resulting in their removal from circulation and accumulation in organs with high phagocytic activity, such as liver and spleen. Particle size is a key parameter as magnetic particles smaller than 4 mm accumulate in the liver (70-90%) and spleen (3-10 %) quickly. Particles larger than 250 nm are usually filtered to the spleen; particles in the range 10-100 nm are mainly phagocytosed through liver cells, while nanoparticles below 5.5 nm can be cleared by renal route.[46] Therefore the optimal particle size for drug delivery treatments ranges between 10 to 100 nm, as these will have the longest blood circulation time. It has been suggested that also the shape can play a role.[47] Hence, passive nanocarriers can be used to deliver drugs for the treatment of hepatic diseases, such as liver metastases, and to favor the internalization of antibiotics by phagocytic cells of the RES for the treatment of intracellular infections.

On the other hand, active targeting relies on specific recognition of the ligands that are displayed on delivery vehicles by cell surface receptors. The ligand used for active targeting can be a small molecule, or a peptide or protein.[48] A key goal of delivery systems is to discharge their payloads specifically at the diseased tissue. The release could be triggered by internal (e.g. glutathione (GSH)), or pH or external (e.g. light) stimuli. Significantly the internal stimuli operate in a biologically control manner, whereas the external stimuli provide spatio-temporal control over the release.[49]

2.2 Thermal therapy

Another interesting application of magnetic and gold nanoparticles is in cancer thermotheraphy, which is considered as a supplementary treatment associated with chemotherapy, radiotherapy, and surgery.[50] The idea of using magnetic induction hyperthermia is based on the fact that when magnetic nanoparticles are exposed to a variable magnetic field, heat is generated by the magnetic hysteresis loss. The amount of heat generated depends on the nature of magnetic material and of magnetic field parameters. Magnetic particles embedded around a tumor site and placed within an oscillating magnetic field will heat up to a temperature dependent on the magnetic properties of the material, the strength of the magnetic field, the frequency of oscillation and the cooling capacity of the blood flow in the tumor. Cancer cells are sensitive to temperature increase and are killed when the temperature raises above 43 °C, whereas the normal cells can survive at higher temperature values. Heat could be generated by applying an appropriate magnetic field. The size of the magnetic crystals commonly employed in hyperthermia is submicrometric, thus the powders or bulk of these biomaterials have comparable properties. These materials are not only biocompatible, but also bioactive and could be useful for bone tumors. Choosing high-power magnetic nanocrystals combined with appropriate external magnetic field, very small amounts of nanoparticles in the order of tenth of milligram may easily be used to raise the temperature of biological tissue locally up to cell necrosis.

Also gold NPs can reasonably used for hyperthermia cacer treatment. AuNPs can absorb and scatter incident light upon excitation of their surface plasmon oscillations typically in the visible range, with their absorption cross sections orders of magnitude larger than those of strongly absorbing organic molecules. In addition, photon energies that are absorbed by AuNPs can be efficiently converted into heat on a picosecond time scale, as a result of electron-phonon and phonon-phonon processes. Thus, AuNPs can be a highly potent photothermal therapeutic agent, by exploiting their strong absorptions and efficient heat conversions.[51-54] Photothermal therapy using spherical AuNPs can be achieved with pulsed or cw (continuous wave) visible lasers due to the SPR absorption in the visible region and thus such treatment is suitable for shallow cancer (e.g. skin cancer). The first thorough study using pulsed laser and gold nanospheres was performed in 2003 by Lin and co-workers for selective and highly localized photothermolysis of targeted lymphocyte cells.[55] Lymphocytes incubated with AnNPs

conjugated to antibodies were exposed to nanosecond laser pulses and showed cell death with 100 laser pulses. Adjacent cells just a few micrometers away without nanoparticles remained viable. Their numerical calculations showed that the peak temperature lasting for nanoseconds under a single pulse exceeds 2000 K with a heat fluid layer of 15 nm. The cell death is attributed mainly to the cavitation damage induced by the generated micro-scale bubbles around the nanoparticles. So far, the use of spherical AuNPs in such an application has not been made, first of all because of their limited tissue penetration, which confines their applicability mostly to melanoma. However, the AuNPs of different forms, such as core-shell nanoparticles with ferromagnetic properties,[56] nanorods,[57] nanocages,[58] nanostars and even popcorn-shaped gold nanoparticles are being tried to be used as photothermal therapy agents using different cancer cell lines.[59,60]

It has been shown that hyperthermia greatly enhances cytotoxicity of radiation and drug treatment with brain tumor cell lines, which were also confirmed in vivo by multimodel hyperthermia studies with rats, rabbits and dogs.[61]

2.3 Iron oxide and gold nanoparticles for medical imaging

In vivo molecular imaging has been identified by the National Cancer Institute of the United States of America as an outstanding opportunity for studying diseases noninvasively at the molecular level.[62] The aim is to visualize molecular characteristics of physiological or pathological processes in living organisms before they manifest in form of anatomic changes.

Superparamagnetic iron oxide nanoparticles can play an important role as MRI contrast agents, to better differentiate healthy and pathological tissues.[63] MRI offers several advantages over alternative techniques, including lack of irradiation, possibility to generate 3D images, excellent spatial resolution with optimal contrast within soft tissues, and a very good signal-to-noise ratio. Paramagnetic (*e.g.,* gadolinium, europium, neodynium, and manganese-containing materials) and superparamagnetic (iron oxide nanocrystals in the form of g-Fe_2O_3, and Fe_3O_4) compounds can be used as MR contrast materials. A first important difference between these two classes of contrast enhancers is that while paramagnetic species enhance the signal in T_1-weighted images resulting in a positive contrast, magnetic nanoparticles provide strong signal enhancement in T_2-weighted images (negative contrast), owing to a different contrasting mechanism.[64,65]

Unfortunately, in most cases, antibody-conjugated gadolinium complexes proved to be largely unsuccessful due to the relatively low sensitivity of MRI and the low density of cell target receptors, thus requiring administration of excessive gadolinium doses. However, Gd-contrast materials may induce severe adverse effects with lethal outcome that have been observed in patients with compromised renal function and subsequent deposition in different organs/tissues and release of highly toxic Gd^{3+} leading to a nephrogenic systemic fibrosis. This drawback can be partially overcome by using magnetic nanoparticles based on iron oxide, which have been demonstrated to induce large increments in transverse relaxation rate upon binding with a 10^6 signal amplification over Gd-DTPA.[66] For this reason, superparamagnetic iron oxide nanoparticles are gaining much attention in view of their usefulness as contrast agents for MRI. The first and major prerequisite of targeted contrast agents is the identification of cell- and/or disease- and/or function-specific biomarkers. Ideally, the biomarkers should be solely and abundantly expressed on the desired cell types. Furthermore, disease-specific biomarkers should be clearly different from healthy status. Biomarkers for targeted contrast agents are cell surface receptors, phospholipids of the outer leaflet of the cell membrane, and enzymes. Targeted magnetic nanoparticles are composed of at least two components: 1) the magnetic iron oxide core represents the imaging or sensing component and 2) the attached molecules represent the targeting or affinity component. Magnetic nanoparticles without targeting components are rapidly engulfed by monocytes and macrophages. Thereby, they can be used to image monocytes and macrophages and their phagocytic aptitude in vivo.

Also gold nanoparticles can be used as contrast agents for in vivo imaging, but exploiting their scattering properties. The scattering properties of gold colloids depend on size, shape and structure of the nanoparticles. Typically, particles of 30–100 nm diameters scatter intensely and can be easily detected by a commercial microscope under dark-field illumination conditions. In fact, 40 nm AuNPs can be easily detected by eye down to a particle concentration of 10^{-14} M. Likewise, the scattering from a 60 nm AuNPs is 10^5 stronger than the emission of a fluorescein molecule.[67] The high scattering cross-sections of AuNPs together with their superior photostability (as compared to organic dyes) make them extremely promising for cellular imaging.

Standard clinical imaging modalities such as X-ray based computer tomography (CT), magnetic resonance imaging, and ultrasound are able to provide basic information

regarding tumor location, size and spread. However, these methods are not efficient in detecting tumors and metastases smaller than 0.5 cm and they can barely distinguish between benign and cancerous tumors.[68]

Present CT contrast agents based on iodine containing molecules are effective in absorbing X-rays, however, they have a number of limitations: nonspecific targeting, because of their inability to be conjugated to most biological components or cancer markers; they allow only very short imaging times due to rapid clearance by the kidneys. On the other hand, gold induces a strong X-ray attenuation, having unique physical, chemical, and biological properties, which make them an ideal candidate for CT contrast agents.[69,70] In addition, AuNPs provide a high degree of flexibility in terms of functional groups for coating and targeting and have also proved to be nontoxic and biocompatible *in vivo*.

The feasibility of AuNPs for cancer imaging has been demonstrated in recent years. In the earlier attempts by Sokolov *et al*, the scattered light is collected in a reflection mode under single laser wavelength excitation using a confocal microscope or simply a laser pen.[71] An improvement of the cancer imaging based on the scattering properties of AuNPs was made by El-Sayed *et al.* using dark field microscopy in 2005.[72] In this case, the nanoparticles are excited by the white light from a halogen lamp which is also the same lamp used for bright field imaging. As the nanoparticles scatter light most strongly at the wavelength of the SPR maximum, the nanoparticles appears in brilliant colour that depends on the size and shape of the particles.[73] Bischof *et al.* demonstrated the use of confocal Raman microscopy to measure the localization of AuNPs with nanoscale resolution. Raman laser interaction with AuNPs inside cells shown unique spectroscopic features corresponding to the different intracellular localizations of AuNPs, proving to be a potential technique for cancer cells imaging.[74]

3. Importance of biofunctionalization of colloidal nanoparticles

The development of NPs for medical and biological applications, demands surface modification and conjugation steps to some extent. In fact, in most cases, the native structure of a biomolecule must be engineered to provide functional groups at their surface. The most widely utilized molecules for nanoparticle functionalization include:

peptides, proteins, and antibodies; enzymes and ribozymes, oligonucleotides and aptamers; carbohydrates, lipids, drugs, or other biologically active small molecules; reporter molecules or contrast agents, including MRI labels, radiolabels, and fluorescent dyes. For this reason, the studies of nano-bio interface have influenced nanomaterials design for biomedical applications. In particular, three different generations of nanoparticles can be identified, which have been engineered for this purpose (**Fig. 5**).

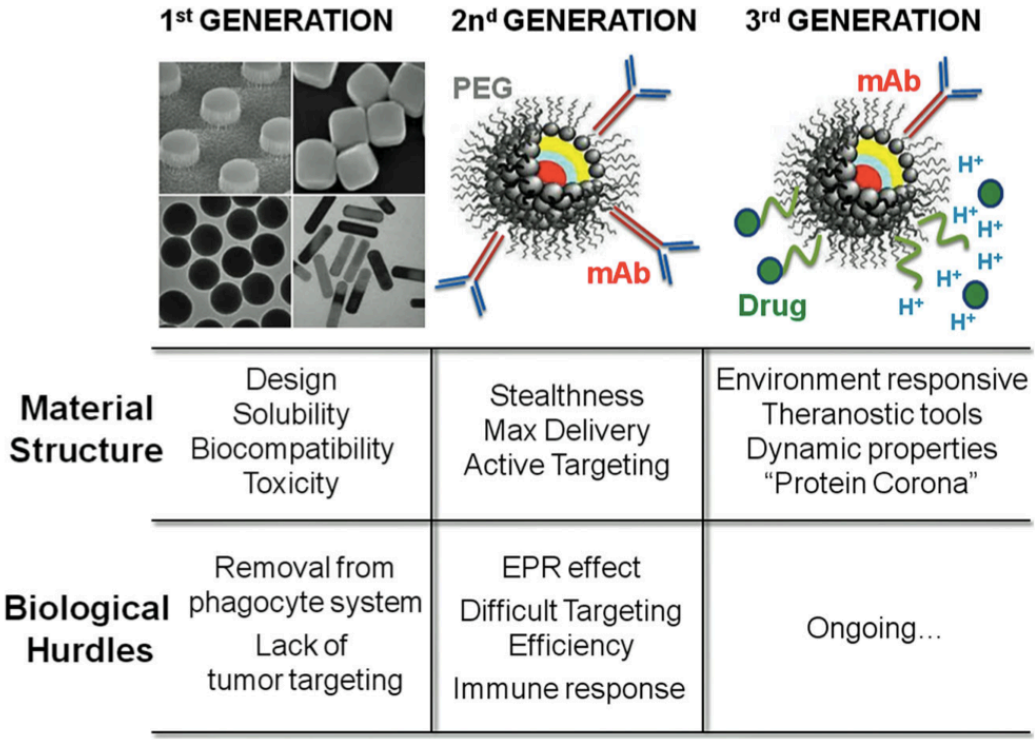

Fig. 5 The evolution of nanomaterials and their biological challenges.

The first generation consists of NPs functionalized through basic surface chemistries to access biocompatibility, enhance cellular uptake, and reduce toxicity. The second generation is represented by nanomaterials with optimized surface outlines to improve their stability and targeting in biological systems.[75-79] These NPs were characterized by two important features: "stealthiness" and active targeting. The aim to develop "stealth" NPs is to maximize blood circulation half-life to enhance the delivery of NPs into the target tissue via a leaky vasculature, exploiting the so-called tumor "enhanced permeability and retention" (EPR) effect. Polyethylene glycol (PEG), an

amphiphilic polymer that can be used for coating NPs surface, represents one strategy to minimize nonspecific interactions. In this context, the overall PEG chain length and its density on the surface strongly affect NPs stability over time.[80] When bound to NP surface, ligands display high local concentration which is a main advantage compared to free molecules. This effect is named “tailoring” and is associated with an avidity increase towards the membrane receptor, with resulting clustering effects at the cell surface.[81]

The third generation of NPs, defined “environment-responsive”, is in continuous evolution. These dynamic NPs take advantage of a combination of physical, chemical, and biological properties. These properties are derived from intrinsic features or arise from the interaction of the NPs with a specific environment they are in contact with, in order to maximize their effect onto targeted subcellular compartments.[82,83] Cellular delivery based on these more sophisticated nanomaterials remains a great challenge in the design of effective nanodrugs. An understanding of how cells traffic their constituents to the appropriate place inside or outside the cell could provide valuable information to improve the targeting efficiency and to reduce the toxicity of the system.

3.1 Tumor targeting

To be successfully used for tumor targeting, the nanoconjugates should (a) be biocompatible and easily functionalized via different bioconjugation techniques, (b) be resistant to the nonspecific protein adsorption via passivation by PEG or polymers, (c) contain a fluorescent/bioluminescent label for imaging purposes, (d) be stable in biological environment and (e) maintain the biological activity of the targeting ligand when bound to nanoparticles.

The development of long-circulating nanoparticles is the first requirement for active targeting. The most satisfactory strategy consists in using macrophage-evading nanoparticles, with long plasma half-life in order to increase the probability of attaining the desired target. The design of such “stealth” nanoparticles requires the consideration of a multitude of physico-chemical and physiological factors, affecting circulation time. In particular, their surface protection by a barrier of hydrophilic oligosaccharide groups is thought to prevent the opsonin adsorption and therefore to avoid the macrophage recognition. Among the physico-chemical factors, which are known to have an effect on the opsonization process, the size, the surface charge density and the hydrophilicity/hydrophobicity balance have been widely investigated, either in liposome or

in polymeric nanoparticle systems.[84] The main conclusion is that the smaller, the more neutral and the more hydrophilic the carrier surface are, the longer its plasma half-life. Concerning the size effect, the available data suggest that surface curvature changes may affect the extent and/or the type of opsonin adsorption. It is generally assumed that surface features are more important than those related to the core, because the surface is in direct contact with blood and organs. For hydrophobic carriers, many studies have concerned the development of core-corona structures where the corona is made of hydrophilic macromolecules for creating polymer brushes, acting as a steric surface barrier and reducing opsonin adsorption. Among the natural or artificial macromolecules, linear dextrans, PEG and their derivatives are widely used. Linear dextrans have been used frequently as plasma expanders in medicine: drugs conjugated to dextran remain in the blood circulation for extended periods of time, proportional to the average molecular weight of the macromolecule. The clearance rate of dextran-coated liposomes is dependent on the density of dextran molecules. Other biological macromolecules have been investigated, *e.g.,* polysialic acid, heparin and heparin-like polysaccharides, but, because of their high cost and/or the possible immunological consequences associated with bacterial-made macromolecules, efforts have been directed to the design of synthetic hydrophilic macromolecules, including “block copolymers”. The strength of polymer adsorption and the resultant polymer conformation is dependent on the proportion and on the size of the hydrophobic block (*e.g.*, polypropylene oxide, PPO) that is flanked on both sides by two hydrophilic chains of polyethylene oxide (PEO) block.[85] In addition, the physico-chemical properties and the curvature of the nanoparticle surface play a role. The nanoparticle stealth behaviour is believed to be a function of the thickness and of the density of the PEO layer. Nevertheless, in order to avoid the possible depletion of copolymers in the blood compartment, great efforts have dealt with the covalent anchorage of PEO macromolecules onto the carrier surface. Such a route is well known in galenical pharmacology, where drugs (small molecules, peptides, proteins, antibodies and oligonucleotides) are conjugated to PEO macromolecules in order to improve their circulation lifetime and bioavailability and decrease their immunogenicity, renal clearance rate and dosing frequency. This process is so widely used that it is called PEGylation. Polyethylene glycol (PEG) is the α,ω-dihydroxyl derivative of PEO and is a flexible polyether, hydrophilic (but also soluble in some organic media), not biodegradable and easily excreted from living organisms by physiological routes. Its functional end-

groups are available for derivatization leading to numerous possibilities for covalent attachment onto preformed functional surfaces or anchoring during the synthesis of polymeric particles. PEG has been shown to be the most effective polymer for suppressing protein adsorption, the optimal molecular weight varying between 2000 and 5000 Da. Lastly, regardless of the active targeting strategy, long circulating carriers present also a great interest as circulating reservoirs for drugs or therapeutic agents with short elimination half-lives or for blood-pool imaging in nuclear medicine. Moreover, long-circulating particles escape from the circulation is normally restricted to sites where the capillaries have open fenestrations, such as in the sinus endothelium of the liver, or when the integrity of the endothelial barrier is perturbed by inflammatory processes (*e.g.,* rheumatoid arthritis, infarction, infections) or by some kinds of tumors. Therefore the idea of exploiting such vascular abnormalities for extravasating and accumulating nanoparticles in these inflammatory sites or tumors is particularly attractive. Such a strategy can be considered both as an active and a passive targeting strategy, as it is independent of the mononuclear phagocyte system mediation.

Ligand conjugation is the second requirement for active targeting. To increase the probability of redirecting long-circulating nanoparticles to the desired target site, their surface has to be modified with ligands that specifically bind to surface epitopes or receptors present on the target cells, for istance, by molecular recognition processes involving antibody-antigene interactions. In principle, these ligands have to be not macrophage-recognizable and coupled to the surface of stealth carriers. Such a strategy should open the possibility of targeting specific cell types or subsets of cells within the vasculature and even elements of vascular emboli and thrombi. In cancer therapy, active targeting could allow for the selective destruction of cancer cells. Among these ligands, often recurring are oligosaccharides, oligopeptides, folic acid, antibodies and their fragments. Due to the unique specificity of monoclonal antibodies for their molecular counterparts and to the possibility to produce immunoglobulins for almost every known marker receptor, this class of proteins is usually considered the preferred choice for active targeting and grate effort has been devoted to the development of antibody-functionalized nanocarriers. However, antibody coupling has at least two drawbacks: 1) the overall size of the antibodies (typically in the range 15-20 nm), which cause particles to diffuse poorly through biological barriers, and 2) their immunogenicity, *i.e.* the property of being able to elicit an immune response within an organism. For this reason, the

coupling of small non-immunogenic ligands to polymeric carriers has been also investigated. Therefore, for tumor targeting, folic acid, antibodies or peptides could be grafted to PEGylated nanoparticles in order to take advantage of the frequent overexpression of the specific receptors onto the surface of human cancer cells. Interestingly, as mentioned above, nanoparticles conjugated with antibodies appeared to interact more efficiently with their receptors than free antibodies. Thus, not only do nanoparticles conjugated with biological molecules selectively target cancer cells, but they could also improve the internalization of the encapsulated drugs into the targeted cancer cells.

3.2 Ligand tailoring and multivalency

The structure of targeting molecules, their valency, and distribution on the nanoparticle surface, as well as the cooperative effects of different molecules are some of the factors that contribute to the effectiveness of targeting.[86] A multivalent interaction is defined as the simultaneous binding of multiple ligands to multiple receptors in biological systems in order to promote targeting to specific cancer cells. Design of multivalent nanosystems can be accomplished through conjugation of multiple recognition units onto an appropriate polymer, dendrimer, micelle, or nanoparticle scaffold.[87] The multivalency effect can enhance the overall affinity of a nanoparticle containing low affinity ligands for cancer cell receptors by expanding the number of molecules used as targeting agents. In normal cells the receptor surface density is low and a single targeting molecule can give rise to an individual ligand-receptor interaction. By contrast, cancer cells express high levels of surface receptors, and thus the conjugation of multiple targeting molecules to a nanoparticle allow simultaneous engagement of numerous receptors, which enhances specificity and efficacy.[88] In particular, multivalent peptides work better than monomeric ones under entropically unfavorable conditions.[89] In this case, particle curvature also plays an important role, with greater curvature allowing a greater number of molecules to be exposed to the cell surface, thus increasing the local concentration of ligands (**Fig. 6**).

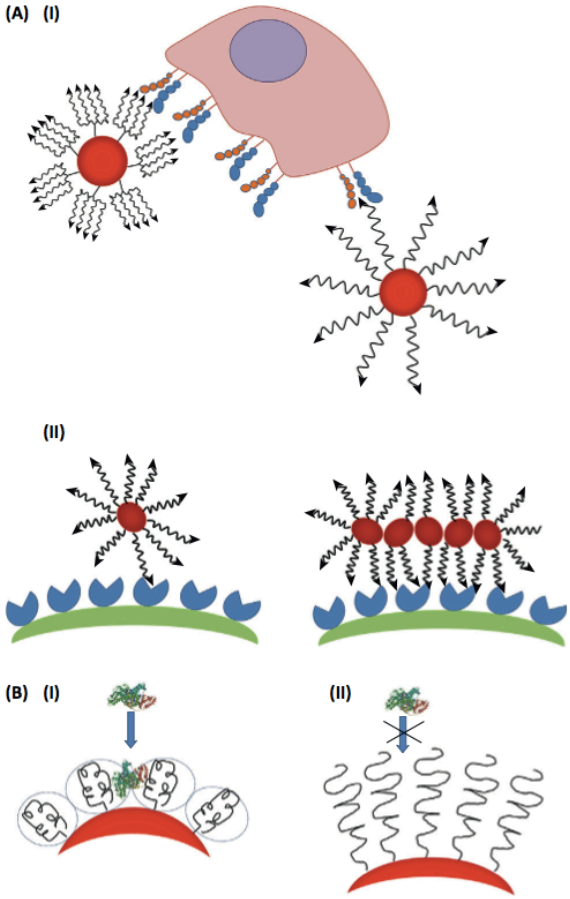

Fig. 6 (A) Schematic representation of a multivalent interaction between differently functionalized nanoparticles and cancer cell receptors: (I) multivalent ligands bind more efficiently than monovalent ligands, improving targeting yield; (II) impact of the shape of nanoconjugates on targeting efficiency: nanoworms bind with higher efficiency compared to a spherical nanoparticles due to multivalent interactions. (B) Polyethylene glycol (PEG) conformation depends on nanoparticle size: (I) PEG molecules assume a mushroom conformation on high-curvature surfaces, and (II) brush configuration when the curvature is low. Nonspecific protein adsorption highly depends on the structure of the PEG layer: when PEG is in the mushroom conformation, adsorption is favored, whereas the tight brush structure inhibits undesirable protein adsorption.

3.3 Interactions of nanoparticles with mammalian cells

At the cellular level, there are several biological barriers that nanoparticles must face to reach their destination and the cell membrane is the first. The plasma membrane has a hydrophobic nature, due to its lipid bilayer, which prevents the diffusion of polar complexes larger than 1 kDa.[90] Usually NPs have the same size range of large proteins

and of cellular and extracellular components. For this reason they can penetrate living cells by exploiting the ordinary cellular endocytic mechanisms.

Small and positively charged NPs can pass the plasma membrane by passive diffusion mechanism,[91] but most of them are internalized by active processes, as phagocytosis (or “cell eating”) and pinocytosis (or “cell drinking”). Phagocytosis is conducted by specialized cells, including macrophages, monocytes and neutrophils, whereas pinocytosis is more general and may occur in all cell types by at least four basic mechanisms: macropinocytosis, clathrin-mediated endocytosis, caveolae-mediated endocytosis, and clathrin- and caveolae-independent endocytosis.

At the interface between nanomaterials and biological systems, NPs uptake depends from several factors related to NPs properties, including size, shape, surface charge and coating. Some types of NPs, due to their size, can cross the membrane in a receptor-mediated way under normal conditions, however, in a biological environment, they can be subjected to destabilizing forces and be endocytosed by the cells as aggregates.[92,93] The effect of shape on cellular uptake is principally due to two causes: 1) specific functional groups protruding from the NPs with directionalities that are affected by the surface geometry and 2) different surface geometries often lead to dissimilar uptake profiles, which may be due to the orientation of the NPs at the cellular interface.[94] Finally, surface coating, especially in terms of charge, has a significant role in NPs translocation into cells. In literature are reported models in which NPs coated with amphiphilic molecules in an ordered ribbon-like alternating arrangements should be able to cross the cell membrane, whereas NPs bearing molecules presented in a random arrangement are taken up by the endocytosis pathway.[95] Simplifying, due to the negative charge of phospholipids bilayer, NPs with a surface charge of the same sign of the membrane basically present no contact, NPs with neutral net surface charge show a minimal interaction with cells, while strong interaction is achieved using positively charged NPs.[96] Further complexity is originated from the heterogeneity of cell membrane.[97] Other cell features can affect NPs cellular uptake. One is the cell type: there are uptake differences between polarized and non-polarized cells because the endocytic properties of apical and baso-lateral cell side are different. In fact, while in non-polarized cells nanoparticles are mainly internalized via macropinocytosis, in polarized cells, the same NPs can be incorporated both by macropinocitosis and clathrin-mediated endocytosis.[95-98] NPs entry is also dependent on the contingent state of the cell. For

example, cells can be closely packed in a compact barrier rather than isolated or fluctuating in a medium. Also relevant is how old are cell and in which phase of the cell cycle they are because of the different protein and lipid expression.[99]

3.4 Breast cancer cells

Breast cancer is a heterogeneous group of neoplasms originating from the epithelial cells coating the milk ducts. Breast tumor presents a large cellular heterogeneity, that has been reported in histology and clinical.[100] However, heterogeneity in cancer cell phenotypes and dynamic plasticity of the tumor, make tumor categorization a demanding task, especially as it relates to therapeutic responses and disease progression. In this context, breast cancer is one of the few tumor types in which molecular classification has successfully been used for the design of individualized therapies, leading to significant improvements in disease-specific survival.[101] Based on gene expression profiling, breast tumors are classified into three major subtypes: luminal, human epidermal growth factor receptor 2^+ ($HER2^+$), and basal like.[102,103] Each of these tumor types has different risk factors as response to treatment, risk of disease progression, and preferential organ sites of metastases. Luminal tumors are positive to estrogen and progesterone receptors, whereas $HER2^+$ tumor have amplification and overexpression of the ERBB2 oncogene and can be effectively controlled with a diverse array of anti-HER2 therapies. Basal-like tumors generally lack hormone receptors and HER2; thus, the majority of these tumors are also called triple–negative breast cancer (TNBC).

As in many cancers, the main hurdle that has been affecting the development and treatment of breast cancer is the incomplete understanding of the molecular biology of the disease. Hence, currently rigorous research is underway examining the molecular biology that may contribute to the disease, and with time better prognosis and therapies will be forthcoming.

In this thesis work we focused on two breast cancer models: a $HER2^+$ and the urokinase plasminogen activator (uPA) system.

3.4.1 HER2 receptor and its role in cancer

The human epidermal growth factor receptor 2 (HER2) is a transmembrane protein composed of an extracellular domain involved in ligand binding, and of an intracellular

domain, the tyrosine kinase domain, which is responsible for signal transduction pathway. Binding between ligand and receptor induces a conformational change that cause the dimerization of the receptor. This phenomenon is responsible for kinase domain transphosphorilation and allows intracellular signal transduction patway activation. HER2 can form homodimer or heterodimer with EGFR, HER3 or HER4 and takes part in the regulatory pathway of fundamental cellular processes like proiferation and survival.[104-107] HER2 is overespressed or constitutively activated in several (25-30%) breast cancer cells and stimulates a great number of intracellular signal proteins and different physiological pathways as MAPK (Mitogen-Activated Protein Kinase), PI3K/Akt (Phosphoinositide 3 kinase/Ak transforming factor), mTOR (mammalian Target Of Rapamycin), kynases Src (tyrosine kinase encoded by Src (sarcoma) proto-oncogene family), and transcriptional factors STAT (Signal Transducers and Activators of Transcription).[104,108,109] The disease breaks out when the loop usually acting as negative regulator is damaged. The two main trasductional signal pathway activated from the ErbB family receptors are the MAPK and PI3K/Akt. The first one stimulate cellular proliferation, while the second promotes cellular survival. ErbB is the family of four structurally related receptor tyrosine kinases. In humans it includes HER1 (EGFR, ErbB1), HER2 (Neu, ErbB2), HER3 (ErbB3) and HER4 (ErbB4). The symbol ErbB derives from the name of the viral oncogene to which these receptors are homologous: Erythroblastic Leukemia Viral Oncogene.

Extracellular domain of HER2 has been the target of several monoclonal antibodies created in order to inhibit proliferation of human cancer cells. The most popular Trastuzumab is a humanized monoclonal antibody consisting of two antigen-specific sites that bind to the juxtamembrane portion of the extracellular domain of the HER2 receptor, preventing the activation of its intracellular tyrosine kinase (**Fig. 7**).[110]

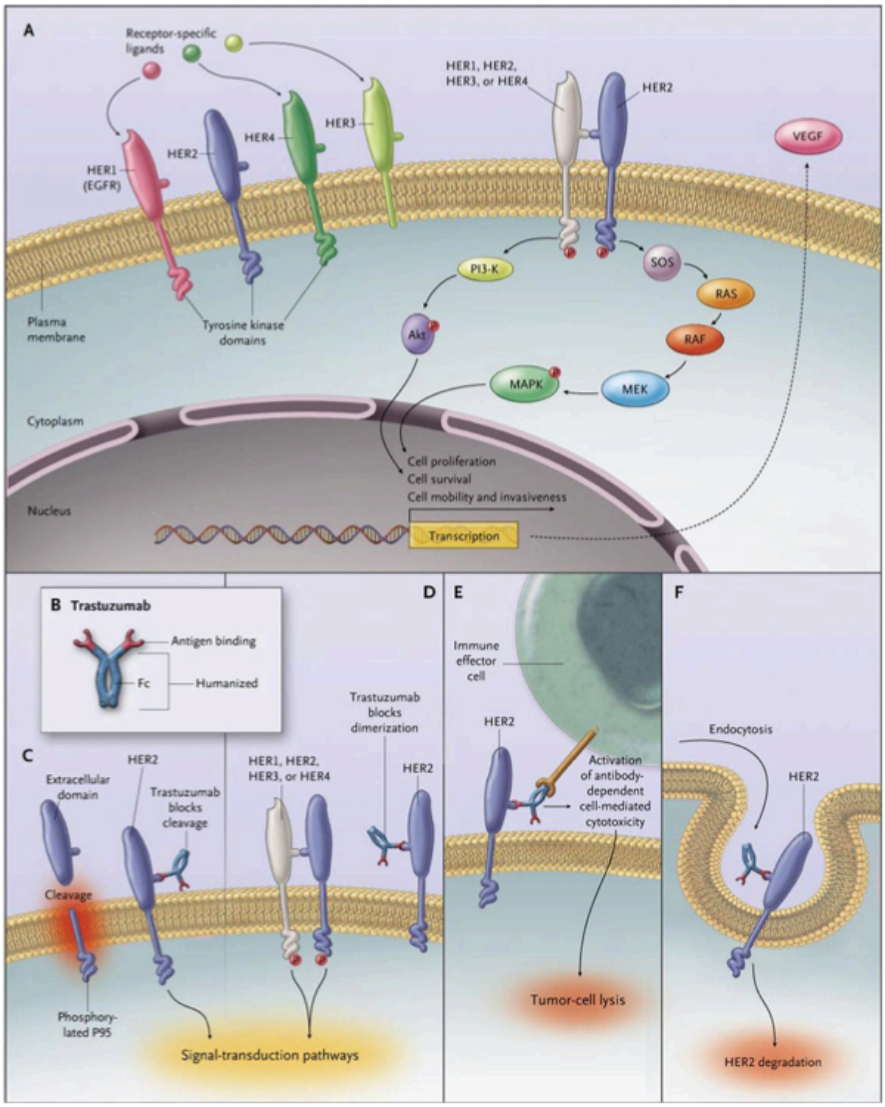

Fig. 7 Transductional signals by ERBB family and TZ action mechanism. The four members of ERBB family: HER1, HER2, HER3 e HER4 (panell A). Each receptor has a specific ligand. All the ERBB family receptors have a intracellular tyrokinasic domain except for HER-3. The homodimerization or the heterodimerization induces the fosphorilation of the tyrosikinasic domain by the activation of the signals of proliferation and survival. The potential action mechanism of trastuzumab is figured in panel B-F. The panel C shows the HER2 extracellular domain cut by MMP-2 (matrix metalloproteinase-2) that cause the production of the phosphoriled domain p95 anchored to the membrane able to active the transduction signal pathway. Trastuzumab induces a signal that reduces the expansion of the extracellular domain or reduce the signal from HER2 by the physic inhibition of homodimerization or heterodimerization. (panel D). TZ can recruit effectors cells of immunological system able to bind Fc and other cytotoxic antibody dependent components that bring to the death of tumor cells (panel E). Over mechanism as the downregolation of HER2 by endocytosis are supposed.[111]

3.4.2 uPA receptor and its role in cancer

Urokinase plasminogen activator receptor (uPAR) is a serine protease of about 50 kDa and it is overexpressed on a variety of cancer cells, such as those of the prostate and the breast.[112-114] Urokinase plasminogen activator (uPA) interacts with uPAR, to form a uPAR-uPA conjugate that enters cells by clathrin-coated, receptor-mediated endocytosis.[115] The uPAR-uPA conjugate is subsequently involved in stimulating various cellular activities such as extracellular matrix invasion,[116,117] plasminogen activation,[118] cell adhesion, and metastasis.[119,120] The uPA ligand is composed of three independent regions: an amino-terminal growth factor domain (ATF or GFD; growth factor domain), a kringle domain, and a carboxy-terminal domain, the region in which uPA exhibits catalytic properties.[121,122] Crystallographic studies of the uPAR-uPA conjugate have revealed that the binding region of uPA for uPAR is localized at the tip of a β-hairpin loop within the GFD.[123] There are two looped structures, one composed of seven amino acid residues (U7) and another of eleven amino acid residues (U11). The second loop, U11, seems to be the motif involved in uPAR binding.[124,125] In literature is reported that the interaction of U11 peptide with uPAR is characterized by an equilibrium dissociation constant, K_d, of 1.3-1.4 μM.[126] Considering the binding affinity along with the uPAR-uPA complex, our expectation is that the uPAR-uPA receptor-ligand system could hold potential for the targeting of synthetic nanoparticles, bearing therapeutic nucleic acids to either prostate or breast cancer (**Fig. 8**).

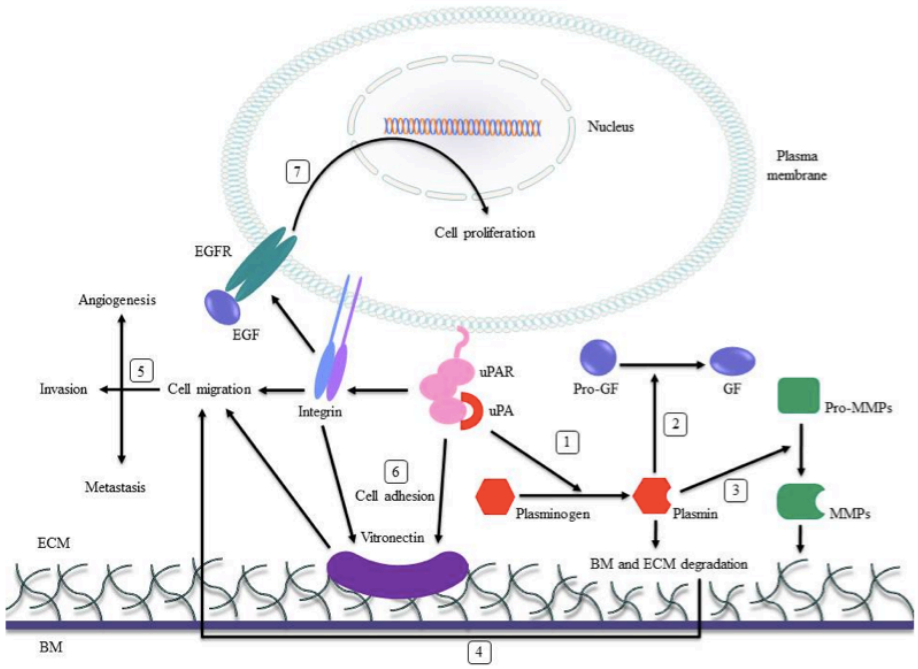

Fig. 8 The urokinase-type plasminogen activator (uPA) system. The membrane anchored receptor (uPAR) binds its extracellular ligand (pro-uPA), causing activation of pro-uPA to uPA which then activates plasminogen to plasmin [1]. Plasmin afterward activates latent growth factors (GF) [2], Matrix metalloproteases (MMPs) [3]. Plasmin and activated MMPs breaks up the basement membranes (BM) and extracellular matrix (ECM) which allows endothelial cells to migrate [4] and to form new vasculature (angiogenesis). In addition, breaking up of ECM allows migration, invasion and metastasis of tumor cells [5]. uPAR also regulates cellular adhesion and migration via interaction with integrins and vitronectin [6]. Interaction between uPAR and integrins has been linked to EGFR- dependent cell proliferation [7].

4. Protein immobilizing

The mode of protein conjugation is of primary importance for retaining the capability of the conjugates to bind effectively to target molecules: both functional conformation and proper orientation must be preserved. This can be achieved by one of three approaches: adsorption, nonspecific covalent conjugation, and selective, orientation-controlled conjugation. Only the latter ensures an optimal outcome in terms of protein binding capacity; with the other two approaches, results are largely unpredictable.

Igor Medintz developed “universal” criteria for the attachment of proteins to surfaces or nanoparticles (**Fig. 9**).[127] An ideal set of such tools would allow: (1) any protein to be attached to any nanoparticle/surface material, (2) in a homogenous manner,

(3) with control over the final orientation of the protein, (4) control over its distance from the surface, (5) control over its density on the nanoparticle/surface and (6) control over its affinity to that surface.

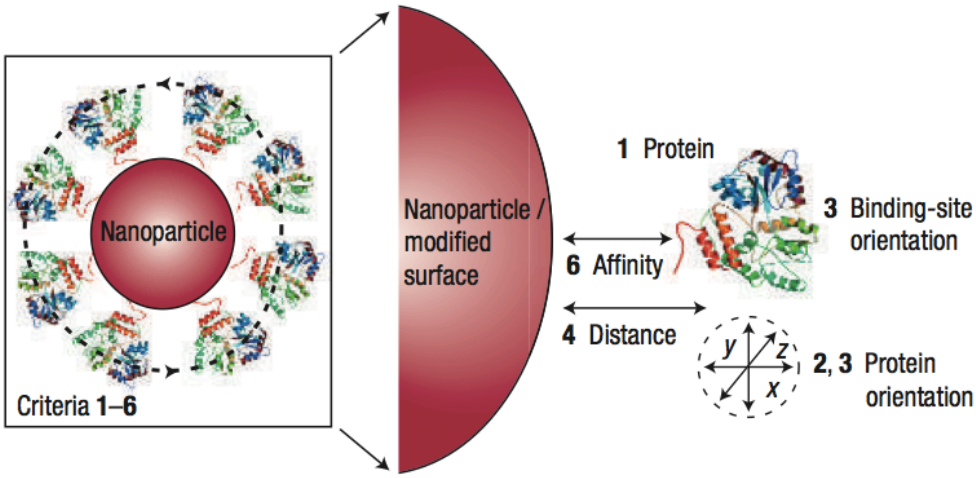

Fig. 9 Schematic representation of the six criteria (see text) for a universal 'toolset' that would allow controlled attachment of any protein to any nanoparticle or surface. In this example, the proteins would cover the nanoparticle surface in three dimensions and could still have some rotational freedom around the axis connecting them to the nanoparticle while still fulfilling the criteria. These criteria can be extended to the interaction of any biosensing molecule with the solid-state components of any biosensing device.

4.1 Binding by adsorption

Generally, protein stability is compromised by many interactions that can cause significant structural distortions or denaturation.[128] The reason is that noncovalent interactions involved in nanoparticle-protein association are of the same nature as interactions responsible for protein structure stabilization: hydrophobic and polar (electrostatic and hydrogen binding). The impact of nanoparticle-protein interactions on protein structure and stability is variable. However, experimental data suggest that hydrophobic surfaces are more likely to adsorb and destabilize proteins.[129] Consistent with these predictions, it was recently reported that the globular Josephin domain of ataxin-3 undergoes misfolding when interacting with a hydrophobic gold surface, but not with hydrophilic surfaces.[130] However, the effect is strongly dependent on the protein species. For instance, the interaction of ribonuclease A with polar silica nanoparticle surfaces leads to significant loss in thermodynamic stability, as assessed in urea

denaturation profiles, although the overall structure was only marginally affected.[131] By contrast, in other cases, interaction with silica leads to partial or complete loss of activity, as reported for lysozyme and cytochrome C, respectively. Also, gold nanoparticles are polar and negatively charged. For instance, adsorption of lysozyme or chymotrypsin on gold nanorods or nanospheres resulted in a complex mode of interaction, strongly affected by nanoparticle morphology.

Nanoparticle surface curvature is another property to be taken in account. In literature data are reported suggesting that adsorption on flat surfaces causes greater changes in protein conformation than adsorption onto curved surfaces. These results may be explained by the fact that proteins adsorbed on a flat surface can interact with a large part of it. They can form stronger interactions and undergo greater structural perturbations, and also lose their biological activity.[132]

4.2 Nonspecific covalent conjugation

This conjugation procedure requires synthetic chemistry protocols that link functional groups of proteins to those of nanoparticles. Most often, covalent conjugation in based on carbodiimide chemistry, which allows condensation of amino and carboxyl groups. Also glutaraldehyde may be used as a crosslinking agent. Another biofunctionalization procedure is based on the capability of gold to form Au-S bonds with thiol groups, so proteins with cysteine residues can be directly coupled on gold nanoparticle surfaces.[133] The advantage of covalent conjugation, as compared to adsorption, is that it produces a permanent bond between proteins and nanoparticles.[134] Another advantage is that covalent conjugation may prevent protein denaturation due to the direct interactions with nanoparticle surfaces.

The main disadvantage of this conjugation method is the lack of control over protein orientation, the impact of chemical modifications on biological activity, and the possible structural distortions resulting from interactions with the surface of the nanoparticles, which may also lead to activity impairment. The latter may be circumvented by using a spacer (tipically PEG), as in the case described above.

4.3 Selective, orientation-controlled conjugation

This approach represents the most effective strategy currently available. It includes several methods that allow to finely control the spatial arrangement of proteins or homing

peptides on the surface of nanoparticles.[127] In order to maintain the optimal functionality of nanoconstructs, the number of bioligands contained in the nanoparticle architecture needs to be minimized. It requires an approach to adjust the positioning of complex biomolecules at the nanoparticle interface.[135]

To maximize targeting efficiency of the functionalized nanoparticle the following is required: (1) a tight irreversible linkage to reduce the system free energy; (2) site-specific binding; and (3) controlled spatial orientation of the biomolecule to make all ligands virtually active.

Classical and nonclassical protein conjugation strategies are described in literature. Classical approaches are divided into two main categories: (1) non-covalent methods take advantage of specific interactions between well-established counterparts, including streptavidin/biotin,[136,137] and polyhistidine/Ni-nitrilotriacetic acid (NTA);[138] and (2) covalent conjugation methods exploit specific chemical reactions as: thiol chemistry, the “click” reaction and and relative bio-orthogonal variants, the Staudinger ligation, and the enzyme-mediated ligation.

Nonclassical methods take advantage of recombinant protein engineering to add selective ligation sites to the peptide sequence, without affecting the recognition efficiency of the immobilized protein for the specific cellular receptor. Three main approaches have been developed: (1) the use of a selectively reactive sequence (SRS) introduced into the conjugation protein by site-directed mutagenesis. This approach may be pursued by conventional reactions or adopting protein engineering procedures by integrating a specific small peptide or even a single amino acid to orient nanoparticle conjugation. A recent example exploits the intentional incorporation of one Cys and one hexaHis residues at different positions to induce different arrangements of a targeting scFv on multifunctional nanoparticles.[139] (2) In the so called bio-click reaction,[140] bimodular fusogenic peptides, consisting of a targeting sequence linked to an affinity tag (capture enzyme), are encoded to bind to a small molecule previously immobilized on the nanoparticle. This molecule acts as a suicide inhibitor by covalently binding to the active site of the capture enzyme. (3) The use of small protein biolinkers, including protein A and G or their variants, provides a universal tool for the oriented immobilization of human IgGs on nanoparticles.

An exhaustive list of all classical and nonclassical bioconjugate approaches, with their advanyages and drawbacks, is reported in **Table 2**.

Table 2 Advanced methods for protein conjugation to nanoparticles: advantages and disadvantages.

	Bioconjugation strategy	Advantages	Disadvantages
Classical approaches	Streptavidin/biotin	Highly stable interaction: one of the highest affinities in biology	Poor control on binding site; heterogeneity in labeling
	Polyhistidine/Ni-NTA	His tag can be easily introduced into nascent peptides or genetically engineered into expressed proteins; K_d on the order 10^{-13} M.	Noncovalently bound proteins could dissociate undesirably; low affinity between the tagged peptide and nanomaterials
	Disulfide bond	Spontaneous reaction occurring without catalytic activation; stable and broadly applicable	Structural alterations and interference from multiple cysteine residues at different positions
	Michael addition	Cysteine can be easily introduced into peptide sequences via site-directed mutagenesis for selective immobilization; spontaneous reaction	Protein structure may be altered during mutagenesis; immobilization cannot be specific if the polypeptide sequence contains multiple cysteine residues
	Soft–soft thiol	Fast and tight immobilization with minimal increase in size	Structural alterations and interference from multiple cysteine residues at different positions; effect of surface rigidity on protein functionality
	Native chemical ligation	It can be performed in aqueous media without protection of any other amino acid including the cysteine residues	The replacement of a nitrogen with a sulfur atom can result in problems in protein folding
	Staudinger ligation	It does not necessitate the use of catalysts	Slow and does not run to full conversion
	Enzyme-mediated ligation	Specific and mild; no extra steps are required to add ligands to target proteins	If the enzyme has broad substrate specificity, it may catalyze the aggregation of target proteins or lead to immobilization at more than one site
	Copper-catalyzed azide–alkyne cycloaddition (''click'' reaction)	Easily accessible; high yielding without need of temperature control; byproduct-free	Instability and toxicity of copper catalyst
	Bio-orthogonal reaction	Strained alkyne derivatives promote the catalyst-free cycloaddition	Hard to have a control on the site of ligation in the peptide sequence
Nonclassical approaches	Selectively reactive sequences (SRS)	No alteration of protein activity; low immunogenicity; quick reaction, specific and irreversible; no crosslinking	No evidence for the safety *in vivo*; kinetics can be slow; possible low conjugation yield
	Bio-click reaction	Robust and mild approach; the protein reactive group can be introduced by polymerase chain cloning	Difficult to control the amount of coupled proteins
	Ligation mediated by small protein bio-linkers	Directional, efficient and site-specific immobilization of entire monoclonal antibodies with conserved biological activity	Large size; potentially immunogenic

Aim of the work

The aim of my PhD research project was development of different protein/peptide conjugation strategies onto multifunctional colloidal nanoparticles. A major issue we addressed is the effect protein conjugation onto nanoparticles may exert on protein stability and biological activity. Actually, it is reported that some conjugation strategies may compromise both protein stability, activity, as well as prevent a proper orientation for the protein to be capable of effectively docking the target receptor.

To address the issue we adopted strategies that make it possible to bind the protein to the respective nanoparticle very specifically and also with a predetermined orientation.

Materials and methods

All chemicals were purchased from Sigma-Aldrich (St. Louis, MO) Fluka (St. Gallen, Switzerland) and Riedel-de Haën (Seelze, Germany) and used as received. Water was deionized and ultrafiltered by a MilliQ apparatus from Millipore Corporation (Billerica, MA) before use. TEM images were obtained by a Zeiss EM-109 microscope operating at 80 kV, available at the "Centro di Microscopia Elettronica per le Nanotecnologie applicate alla medicina" (CMENA, University of Milan). Dynamic light scattering (DLS) measurements were performed at 90° with a 90Plus Particle Size Analyzer from Brookhaven Instruments Corporation (Holtsville, NY), working at 15 mW of a solid state laser (λ = 661 nm). Viscosity and refractive index of pure water were used to characterize the solvent. Nanoparticles were dispersed in the solvent and sonicated in a S15H Elmasonic apparatus (Elma, Singen, Germany) before analysis. UV-vis spectra were recorded using a Nanodrop 2000C spectrophotometer (Thermo Fisher Scientific, Wilmington, Germany) in an absorbance range between 200 and 700 nm. T_2 relaxation times were performed at a temperature of 313 K using a Bruker Minispec mq20 system (Bruker, Ettlingen, Gerrmany) working with ^{1}H at 20 MHz magnetic field with the following parameters: Carr-Purcell-Meiboom-Gill pulse sequence, 1000 echoes with a 20 ms echo times and 2 s repetition time. Samples were introduced using a 10 mm NMR spectroscopy tubes prewarmed and sonicated at 40 °C. Fluorescence measurements

were performed with FluoroMax-4 Spectrofluorometer (Horiba Scientific, Edison, NJ), using Hellma fluorescence Suprasil cuvette quartz with pathlenght of 1 mm. The FTIR absorption spectra were acquired using the Varian 610-IR infrared microscope coupled to a Varian 670-IR spectrometer (Varian Australia Pty Ltd, Mulgrave VIC, Australia) and equipped with a nitrogen-cooled, mercury–cadmium–tellurium (MCT) detector. Flow cytometry analyses were performed using a FACS Calibur flow cytometer (Becton Dickinson, Franklin Lakes, NJ). Confocal microscopy images were acquired with a SP2 AOBs microscope confocal system (Leica, Solms, Germany).

1. Synthesis and characterization of iron oxide and gold nanoparticles

1.1 Magnetic iron oxide nanocristals (MNC2)

1.1.1 Synthesis of Fe_3O_4 nanoparticles (MNC1) by coprecipitation method

Monodisperse magnetic nanoparticles were obtained as previously described here: to a solution of distilled water (173 mL) and NH_4OH 28-30% (14 mL), prewarmed at 60 °C under vigorous stirring, was added a mixture of 1 M $FeCl_3 \cdot 6H_2O$ in distilled water (20 mL) and 2 M $FeSO_4 \cdot 7H_2O$ in 2 N HCl (5 mL); the solution turned dark instantaneously and a black precipitate was formed. The reaction suspension was heated immediately at 90 °C under vigorous magnetic stirring for 30 min. At the end of the reaction, the product was collected from the suspension with a rare-hearth permanent magnet while the supernatant was discarded. The particulate was washed several times with distilled water until neutral pH of the washings. Finally obtained MNC1 were redispersed in distilled water (220 mL) at a concentration of 7.5 mg Fe_3O_4 mL^{-1}.

1.1.2 Synthesis of PEG-coated Fe_3O_4 nanoparticles (MNC2)

A water suspension of MNC1 (3 mL, 7.5 mg mL^{-1}) was sonicated 30 min at RT; subsequently, polyethylene glycol 600 diacid (57 µL, 0.112 mmol) was added to the suspension and the resultant mixture was sonicated for 30 min at RT At the end of the reaction, nanoparticle suspension was transferred in a centrifuge tube and unreacted nanoparticles were centrifuged at 10000 rpm for 5 min. In this way, supernatant solution, which appeared as a brown clear solution, was separated from the precipitates, which were discarded. To remove the excess of the unreacted reagent, the solution was purified

by dialysis membrane (MW CutOff 12-14000 Da) overnight; finally MNC2 were diluted with double distilled water to a final concentration of 1 mg mL^{-1}. Under these conditions, nanoparticle suspension was stable for several months at RT

1.1.3 Measurement of proton transverse relaxation times (T_2) of MNC2

Before T_2 measurements, the tubes were prewarmed at this temperature for 10 min in order to obtain thermal equilibration and T_2 values were acquired on the samples at this stage. Relaxivity was determined as the slope of a $1/T_2$ plot as a function of iron concentration expressed in mM.

1.1.4 Dependence of MNC2 stability on pH

Different vials with MNC2 suspension (200 µL) in double distilled water (1.8 mL) were prepared at different pH (C_{NPs}= 0.1 mg mL^{-1}). Initial pH value of MNC2 was around 5. The acidic pH values were obtained adding 0.02 N HCl dropwise in a range of pH from 1 to 5. The alkalinity was raised above this value by adding 0.02 N NaOH dropwise in the range between 7 and 11. In this way, the stability of MNC2 was controlled by monitoring the decreasing of UV-vis spectra of the PEG absorption from 0 to 90 min (in the range of λ from 200 and 600 nm).

1.2 Magnetic iron oxide nanoparticles (MNP2)

1.2.1 Synthesis of surfactant-coated Fe_3O_4 nanoparticles (MNP0)

MNP0 were synthesized according to Park et al.[141] First, the iron-oleate complex was prepared by reacting metal chlorides and sodium oleate in a mixture solvent composed of ethanol, distilled water and hexane. The resulting solution was heated to 70 °C and kept at that temperature for 4 h. When the reaction was complete, the upper organic layer containing the iron–oleate complex was washed three times with distilled water in a separatory funnel. After washing, hexane was evaporated off, resulting in iron–oleate complex in a waxy solid form. For the nanoparticles synthesis, 40 mmol of the iron-oleate and 5.7 g of oleic acid (20 mmol) were dissolved in 200 g of 1-octadecene at room temperature. The reaction mixture was heated to 320 °C and kept at that temperature for 30 min. The resulting solution containing the nanoparticles was then cooled to room temperature, ethanol (100 mL) was added and the black precipitate was centrifuged. The

supernatant was discarded and the product washed several times with ethanol to remove the unbound surfactant. The resulting oleylamine-coated magnetite nanocrystals were dispersed in chloroform (MNP0).

1.2.2 Synthesis of PMA-coated Fe_3O_4 nanoparticles (MNP1 and MNP2)

An aliquot of 0.5 M PMA (63 µL) was added to MNP0 (4.6 mg in $CHCl_3$), the mixture was homogenized and the solvent was then evaporated at reduced pressure. Sodium borate buffer (SBB, pH 12, 10 mL) was added obtaining a clean nanoparticle dispersion, which was concentrated in Amicon tubes (MW cutoff 100 kDa) by centrifuging at 3500 rpm for 1 h. Finally, the nanoparticles were washed twice diluting with SBB in the same way and concentrated (each centrifuge cycle was 20 min at 3500 rpm) to a final volume of 200 µL. The nanoparticle solution (MNP1), was reacted with aqueous 0.1 M N-(3-Dimethylaminopropyl)-N′-ethylcarbodiimide hydrochloride (EDC·HCl) (18 µL) for 2 min, then aqueous 0.05 M (2,2-(ethylendioxy)bisethylamine, EDBE) (9 µL) was added and stirred for 2 h (MNP2). It is possible to have fluorescent nanoparticles making the same protocol but using FITC-PMA. To synthesize fluorescent MNP2, to a 0.5 M of PMA solution in $CHCl_3$ (5 mL) was added 1.0 M fluoresceinamine (0.5 mL in dimethylsulfoxide (DMSO)) prior to add the PMA solution to MNP0. The mixture was reacted overnight at room temperature. This solution (63 µL) was added to MNP0 (4.6 mg in $CHCl_3$).[141,142] In this case, nanoparticles were called MFP1 and MFP2.

1.2.3 Functionalization of PMA-coated Fe_3O_4 nanoparticles with linker (MNP3)

MNP2 (or MFP2) dispersion was shaken overnight at 4 °C in the presence of ligand (460 µL, 10 mg mL^{-1} in DMSO), concentrated and washed twice with water as described above (MNP3). A NH_2-ended O_6-PEG-guanine (L0) was used for the conjugation of SNAP-scFv, 2-(2-(2-((4-nitrophenoxy)carbonyloxy)ethoxy)ethoxy)ethyl 2-(2-(6-chlorohexyloxy) ethoxy) ethylcarbamate linker (L1) was used to conjugate HALO-H11 and Imidazole-1-carboxylic Acid 11-(Diethoxy-phosphoryl)-undecyl ester (L2) for the binding of CUT-U11.

1.3 Gold Nanoparticles Preparation

Citrate-stabilized gold nanoparticles (AuNPs) of 16 ± 1.2 nm were synthesized according to the method developed by Turkevich and Frens.[143,144] Briefly, 30 mg (80 mmol) of $HAuCl_4$ trihydrate was added to 300 mL of double-distilled water and the solution was heated to boiling. Next, 9 mL of warm (60-80 °C) 1% trisodium citrate were added, followed by reflux for 60 min until color change from dark blue to red was observed. Once cooled to room temperature, the nanoparticles were filtered using a 0.45 mm Millipore filter before use, and characterized by UV-vis spectroscopy, TEM, DLS and ζ-potential techniques.

1.3.1 Nanoparticle physicochemical characterization

Extinction spectra of AuNPs were recorded on a NanoDrop 2000c Spectrophotometer (ThermoScientific) in 1 cm path length quartz cuvettes, using mQ water as media. The added volume of NPs solution was 10 orders of magnitude lower compared to the present volume of medium to maintain the physical conditions of the medium. In each case, the pure medium served as a blank. The surface plasmon peaks at 518 nm and 524 nm were observed for NPs before and after functionalization, respectively. Nanoparticle concentration was calculated using an extinction coefficient of 2.14×10^8 $M^{-1}cm^{-1}$, following the procedure described by Haiss et al.[145] DLS measurements were performed using a disposable cuvette with 1 cm optical path lengt. The cuvettes were cleaned with Milli-Q water and stored dry. The samples were prepared by dilution with Milli-Q water containing 10 mM NaCl, followed by filtration with a 0.45 µm cellulose acetate syringe filter before loading into the cuvette in order to remove large interfering particulate matter. Each sample was allowed to equilibrate for 4 min prior to starting measurement. Three to ten independent measurements of 60 s duration were performed, at 25 °C. The calculations of hydrodynamic diameter were performed using Mie theory, considering absolute viscosity and refractive index values of the medium to be 0.911 cP and 1.334, respectively. The ζ-potential was determined at 25 °C. The samples for measurements were prepared by dilution the concentrated nanoparticles in 10 mM NaCl (pH 7). A minimum of 3 runs and 10 subruns per sample were performed to establish measurement repeatability. The ζ-potential was automatically calculated from electrophoretic mobility based on the Smoluchowski theory. A viscosity of 0.891 cP, a dielectric constant of 78.6, and Henry function of 1.5 were used for the calculations. Then

samples for TEM images were prepared by evaporating a drop of nanoparticles onto carbon-coated copper grid and allowing it to dry on the air. The histograms of the particle size distribution and the average particle diameter were obtained by measuring about 150-200 particles by using Measure IT Olympus Software.

1.3.2 Fluorescence spectroscopy

The samples for Fluorescence analysis on Au-U11, Au-$U11_{scrambled}$ and Au-peptide NPs were diluted with mQ water (at a ratio 1:500) prior to analysis and the spectra were acquired in the range of 500-600 nm after excitation at 488 nm wavelength. An emission peak at 517 nm was attributed to fluorescent AuNPs.

2. Protein production

2.1 Trastuzumab

Trastuzumab was received from Roche Products Ltd. (UK) as a powder lyophilized for intravenous administration; before reactions it was purified from additives by dialysis (membrane, MW cutoff 12-14000 Da) in phosphate buffer solution, pH 7.4, 300 mM NaCl, 2.7 mM KCl, 10 mM phosphate.

2.2 SNAP-scFv800E6

2.2.1 Construction of the expression vector

The DNA coding for SNAP-tag was amplified from pGEX- 6P-1-SNAP-GFP vector (kindly provided by Petra Hohenberger, Karlsruher Institut für Technologie (KIT)). The primers were: 5'-CCGAGAATTCATGGACAAAGACTGCGAAATG-3' (forward primer) and 5'-CGTAGAATTCGCCCAGCCCAGGCTTGCCCAG-3' (reverse primer), containing an *EcoRI* site (underlined). The resulting PCR product was digested with *EcoRI* and ligated to the corresponding site of the expression vector pPICZαA-scFv800E6.[146] The ligation mixture was transformed by electroporation into *E. coli* DH5α competent cells for propagation of the recombinant plasmid. The resulting recombinant expression vector pPICZαA-SNAP-scFv800E6 was confirmed by restriction endonuclease digestion and DNA sequencing.

2.2.2 Transformation in P. pastoris and screening of transformants

The recombinant expression vector pPICZαA-SNAP-scFv800E6 was linearized with *HindIII* and the digested product was transformed into the *P. pastoris* host strains KM71H and GS115 by electroporation (1.5 kV, 400 Ω, 25 μF; Bio-Rad Gene Pulser). Transformants were selected on YPDS (1% yeast extract, 2% peptone, 2% dextrose, 1 M sorbitol) plates containing 100 μg mL^{-1} Zeocin. For small-scale screening of SNAP-scFv800E6 fusion protein-productive clones, single clones from YPD agar plates were grown in 5 mL YPD medium at 30 °C overnight with shaking at 250 rpm. The cultures were centrifuged at 1500×g for 4 min and then the pellets resuspended in 5 mL of BMMY (1% yeast extract, 2% peptone, 100 mM potassium phosphate (pH 6.0), 1.34% YNB, 0.00004% biotin, 0.004% histidine, 0.5% methanol) or BMDY (BMMY containing 2% dextrose instead of methanol). To maintain induction, methanol was added to the culture medium every 24 h at a final concentration of 0.5%. After 48 h induction, the cultures were centrifuged at 5000×g for 10 min and the supernatants analyzed by SDS-PAGE and Western blotting. For medium-scale screening of SNAP-scFv800E6 fusion protein-productive clones, single clones from YPD agar plates were grown in 10 mL YPD medium at 30 °C overnight with shaking at 250 rpm. The cultures were centrifuged at 1500×g for 4 min and then the pellets resuspended in 10 mL of BMMY (1% yeast extract, 2% peptone, 100 mM potassium phosphate (pH 6.0), 1.34% YNB, 0.00004% biotin, 0.004% histidine, 0.5% methanol) or BMDY (BMMY containing 2% dextrose instead of methanol). To maintain induction, methanol was added to the culture medium every 24 h at a final concentration of 0.5%. After 0, 24, 48 and 72 h induction, the cultures were centrifuged at 5000×g for 10 min and the supernatants analyzed by SDS-PAGE and Western blotting.

2.2.3 Optimization of induction conditions

In order to setup the optimal conditions for SNAP-scFv expression, medium-scale culture experiments were performed in different induction conditions. The best producing clone GS115-pPICZαA-SNAP-scFv800E6-1 was grown in 10 mL YPD medium at 30 °C overnight with shaking at 250 rpm. The cultures were centrifuged at 1500×g for 4 min and then the pellets were resuspended in 10 mL of BMMY with different methanol concentration (0.5% and 2%) and in BMMY supplemented with 2% dextrose or 0.8% glycerol. The cultures, yielding an initial OD_{600} value of 10, were supplemented every 24 h

with methanol to a final concentration of 0.5% or 2% to maintain induction. Culture supernatants were sampled at different times to monitor SNAP-scFv production by Western blot analysis.

2.2.4 Purification of SNAP-scFv800E6

For purification, 200 mL yeast culture in BMMY with 2% dextrose yielding an initial OD_{600} value of 10 was induced by daily addition of methanol to a final concentration of 0.5%. After 48 h of methanol treatment, the culture supernatant was filtered through 0.22 µm filters and dialyzed overnight in 50 mM sodium phosphate pH 8.0, 300 mM NaCl. The dialyzed medium was loaded at a flow rate of 0.5 mL min^{-1} onto a Ni-NTA Agarose (Qiagen) column (bed volume 0.5 mL) pre-equilibrated with 50 mM sodium phosphate pH 8.0, 300 mM NaCl, 10 mM imidazole. The column was washed with 50 mM sodium phosphate pH 8.0, 300 mM NaCl, 20 mM imidazole and the protein eluted with a stepwise imidazole gradient, 100 mM to 200 mM, in the same buffer. Fractions were collected and analyzed by SDS-PAGE and Western blotting. Protein content was determined using the Coomassie Plus Protein Assay Reagent from Pierce and bovine plasma immunoglobulin G as the standard protein.

2.3 HALO and HALO-U11

2.3.1 Construction of the expression vector

A modified DNA sequence encoding for HALO and for HALO-U11 were synthesized (Eurofins MWG Operon, Ebersberg) to obtain sequences containing *SalI* and *XhoI* restriction sites, respectively, at 5' and 3' positions. HALO and HALO-U11 DNA sequence were cloned in a pGEX-6P-1 vector (GE Healthcare, Life Sciences, Little Chalfont, UK) between *SalI* and *XhoI* restriction sites according to Molecular cloning handbook, to obtain HALO and HALO-U11 as GST-fusion proteins containing a PreScission protease recognition site. Plasmidic DNA (pGEX/HALO and pGEX/HALO-U11) were sequenced and used to transform *E. coli* expression strain BL21(DE3)-RIL (E. coli B F^{-}ompT hsdS ($rB^{-}mB^{-}$) dcm^{+} gal?(DE3) (Stratagene, La Jolla, CA).

2.3.2 HALO and HALO-U11 expression and purification

E. coli strain BL21(DE3)-RIL expressing HALO or HALO-U11 as GST-fusion

protein were grown at 37 °C in LB-ampicillin medium until they reached A_{600} = 1 and induced overnight with 0.5 mM IPTG at 25 °C. A 2.8 g cells were obtained from 500 mL of culture. To prepare crude extract, cells were resuspended in lysis buffer (5 mL g^{-1} wet weight; 25 mM potassium phosphate, pH 7.2, 150 mM NaCl, 0.5 mM phenylmethanesulfonyl fluoride, 5 mM DTT, 100 mM $MgCl_2$) plus 1 mg mL^{-1} lysozyme and incubated for 30 min at 4 °C. DnaseI (0.2 mg g^{-1} cells, wet weight) and 1% Triton X-100 were added to cell suspension, and the sample was further incubated for 30 min at 25 °C and sonicated. Finally, it was centrifuged for 30 min at 39000×g. Supernatant was loaded onto Glutathione Sepharose 4B affinity column (0.5 mL bed volume, GE Healthcare). Then, it was washed with 20 volumes of washing buffer (25 mM potassium phosphate, pH 7.2, 150 mM NaCl) and equilibrated with 10 volumes of cold Cleavage Buffer (50 mM Tris-HCl, pH 7.0, 150 mM NaCl, 1 mM EDTA, 1 mM DTT). To elute HALO or HALO-U11, the resin was incubated at 4 °C overnight under shaking with Prescission Protease (400 U mL^{-1} resin) (GE Healthcare). Proteins eluted with PreScission protease cleavage were analyzed by SDS-PAGE. The proteins were detected by Coomassie Brilliant Blue R-250 staining. Protein content was assayed at 280 nm using extinction coefficient of 60000 M^{-1} cm^{-1} and 66920 M^{-1} cm^{-1} for HALO and HALO-U11, respectively.

2.3.3 HALO and HALO-U11 labeling

HALO and HALO-U11 were labeled incubating 1 mg of the protein (1 mg mL^{-1}) in 0.1 M sodium carbonate-bicarbonate buffer with 2 mg of fluoresceine isothiocyanate (Sigma) for 2 h at 25 °C. Then, HALO_FITC and HALO-U11_FITC were purified from unreacted FITC through a sephadex G-25M column and protein concentration was determined using the following formula: [concentration (mg mL^{-1})] = $[A_{280}-(0.35 \times A_{495})]/1.4$.

2.4 CUT and CUT-U11

2.4.1 CUT DNA synthesis and cloning in pET-11a vector

A modified DNA sequence encoding for CUT was synthesized (Eurofins MWG Operon, Ebersberg) to obtain sequences containing *NdeI* and *BamHI* restriction sites, respectively, at 5' and 3' positions. CUT DNA sequence was cloned in a pET-11a vector

between *NdeI* and *BamHI* restriction sites according to Molecular cloning handbook, to obtain CUT fused with His-Tag. Plasmidic DNA (pET-11a/CUT) was sequenced and used to transform *E. coli* expression strain OrigamiB(DE3).

2.4.2 CUT-U11 DNA synthesis and cloning in pET-30b(+) vector

A modified DNA sequence encoding for CUT-U11 were synthesized (Eurofins MWG Operon, Ebersberg) to obtain sequences containing *NdeI* and *BglIII* restriction sites, respectively, at 5' and 3' positions. CUT-U11 DNA sequence was cloned in a pET-30b(+) vector between *NdeI* and *BglIII* restriction sites according to Molecular cloning handbook, to obtain CUT-U11 fused with His-Tag. Plasmidic DNA (pET-30b/CUT-U11) was sequenced and used to transform *E. coli* expression strain Tuner(DE3): F^{-}*ompT* *hsdS*$_B$ (r_B^- m_B^-) *gal dcm lacY1*. A spacer made of GGGGSGGGG was inserted between cutinase and U11.

2.4.3 CUT expression and purification

E. coli strain BL21(DE3)-RIL expressing CUT was grown at 37 °C in LB-ampicillin medium until they reached A_{600} = 1 nm under stirring and induced overnight with 1 mM IPTG at 18 °C. A 3.3 g cells were obtained from 1 L of culture. To prepare crude extract, cells were resuspended in lysis buffer (5 mL g^{-1} wet weight: 50 mM Na_2HPO_4/ 300 mM NaCl pH 7.4, 100 mM $MgCl_2$, 10 mM imidazole), 1 mg mL^{-1} lysozyme, DNAseI (0.2 mg g^{-1} cells, wet weight) and 1% Triton X-100 were added to cell suspension, and the sample incubated for 30 min at RT and sonicated. Finally it was centriguged for 30 min at 20000 rpm, 4 °C. Supernatant was loaded onto His-pure-cobalt resin (1 mL bed volume, Thermo Scientific, Rockford, Illinois, USA). Then it was washed with 10 volumes of water and equilibrated with 10 volumes of equilibrated buffer (50mM Na_2HPO_4/300 mM NaCl pH 7.4, 10 mM imidazole). To elute CUT, four elution buffers with an increasing gradient of imidazole were prepared (50 mM, 100 mM, 150 mM and 200 mM). Proteins eluted were then analyzed by SDS-PAGE.

2.4.4 CUT-U11 expression and purification

E. coli strain Tuner(DE3)pET-30b/CUT-U11/His-tag was grown at 37 °C in LB-kanamicin medium until they reached A_{600} = 1 nm under stirring and induced 3 h with

0.05 mM IPTG. A 2.3 g cells were obtained from 500 mL of culture. To prepare crude extract, cells were resuspended in lysis buffer (3 mL g^{-1} wet weight: 50 mM Na_2HPO_4/300 mM NaCl pH 8, 0.5 mM phenylmethanesulfonyl fluoride, protease inhibitor). 1 mg mL^{-1} lysozyme, DNAseI (0.2 mg g^{-1} cells, wet weight) and 1% Triton X-100 were added to cell suspension, and the sample incubated for 30 min at RT and sonicated. Finally it was centrifuged for 30 min at 20000 rpm, 4 °C. Supernatant was loaded onto Ni-NTA Superflow resin (0.5 mL bed volume, Quiagen S.p.a., Milan, Italy). Then it was washed with 10 volumes of water and equilibrated with 10 volumes of equilibrated buffer (50mM Na_2HPO_4/300 mM NaCl pH 8). To elute CUT-U11, five elution buffers with an increasing gradient of imidazole were prepared (100 mM, 150 mM, 200 mM, 250 mM and 300 mM of imidazole). Proteins eluted were then analyzed by SDS-PAGE.

2.4.5 CUT and CUT-U11 labeling

CUT and CUT-U11 were labeled incubating 1 mg of CUT-U11 (1 mg mL^{-1}) in 0.1 M sodium carbonate-bicarbonate buffer with 2 mg of fluoresceine isothiocyanate (Sigma) overnight at 4 °C. Then, CUT-F and CUT-U11-F were purified from unreacted FITC throught a sephadex G-25M column and proteins concentration were determined using Nanodrop 2000c/2000 UV-Vis Spectrophotometers (Thermo Scientific), *Protein and labels* software.

2.4.6 Activity assay

The activity of CUT and CUT-U11 were measured with Kontron Uvikon 930 (NorthStar Scientific) spectrophotometer. The activity assay was performed using 4-nitrophenil decanoate as enzyme substrate. The release/absorbance (420 nm) of the chromogenic product 4-nitrophenol in time was measured.

2.5 U11 peptide

2.5.1 Peptide synthesis

Peptides U11 and U11 scrambled were assembled by stepwise microwave-assisted Fmoc-SPPS on a Biotage ALSTRA Initiator+ peptide synthesizer, operating in a 0.12 mmol scale on a 2-CTC resin (0,6 mmol/g). Resin was swelled prior to use with a NMP/DCM mixture. Activation and coupling of Fmoc-protected amino acids was

performed using Oxyma 0.5 M / DIC 0.5 M (1:1:1), with a 5 equivalent excess over the initial resin loading. Coupling steps were performed for 10 minutes at 50 °C. Deprotection steps were performed by treatment with a 20% piperidine solution in DMF at room temperature (1 × 3 min + 1 × 5min). Following each coupling or deprotection step, peptidyl-resin was washed with DMF (4 × 5ml). Following chain assembly, peptide was cleaved from the resin using a TFA 90%, water 5%, thioanisole 2.5%, TIS 2.5% mixture (3 h, RT). Following precipitation in cold diethyl ether, crude peptide was collected by centrifugation and washed with further cold diethyl ether to remove scavengers. Peptides was then dissolved in 50% aqueous acetonitrile 0.07% TFA buffer and purified by preparative RP-HPLC.

2.5.2 RP-HPLC analysis and purification

Analytical and semi-preparative reversed phase high performance liquid chromatography (RP-HPLC) were carried out on a Tri Rotar-VI HPLC system equipped with a MD-910 multichannel detector for analytical purposes or with a Uvidec-100-VI variable UV detector for preparative purpose (all from JASCO, Tokyo, Japan). A Phenomenex Jupiter 5m C18 90Å column (150 × 4.6 mm) was used for analytical runs and a Phenomenex Jupiter 10m C18 90Å (250 × 21.2 mm) for peptide purification. Data were recorded and processed with Borwin software. 2 % /min linear gradient of 0-60 % eluent B (eluent A = H_2O/ 3 % CH_3CN / 0.07 % TFA, eluent B = 70 % CH_3CN/ 30 % H_2O/ 0.07 % TFA) was employed at a flow rate of 1 mL/min for analytic purposes. UV detection was recorded in the 220-320 nm range. Peptide purification was achieved by preparative RP-HPLC at a flow rate of 14 mL/min using a 100% A → 30% B gradient over 40 min. Pure RP-HPLC fractions (>95%) were combined and lyophilized. Mass spectra were collected separately.

2.6 Peptides

2.6.1 Peptide synthesis

The selected peptides were manually synthesized using the Fmoc (fluorenylmethyloxycarbonyl) solid-phase strategy (0.15 µmol). The syntheses were carried out on 2-Chlorotrityl resin (loading 1.6 mmol/g) using all standard L-aminoacids. The aminoacids in 3-fold excess were pre-activated with TBTU (4 equiv)/HOBt (4

equiv)/DIPEA (8 equiv) in DMF and then added to the resin and left under stirring for 50 minutes. 5(6)-carboxyfluorescein (2 equiv) was dissolved in a solution of HOBt (2.5 equiv) and EDAC (2.5 equiv) in DMF, added to the resin and left under stirring for 16 hours, then washed with 20% piperidine in DMF for 45 minutes. The Fmoc deprotection step was performed with 20% piperidine in DMF for 5 + 15 min. The peptides were cleaved off the resin by treatment with a mixture of trifluoroacetic acid/phenol/water/triisopropylsilane/tioanisol for 2 hours at room temperature and under nitrogen atmosphere in order to reduce cysteine oxidation. The resins were filtered, and the crude peptides were precipitated with a mixture of t-butyl-methyl-ether and petroleum ether, dissolved in a water/methanol solution and lyophilized.

2.6.2 RP-HPLC analysis and purification

The products were purified by preparative RP-HPLC on a Waters system equipped with photodiode detector array Waters 2996 using a Sunfire C18 OBD Prep column (19 x 150 mm; 5 µm) and a linear gradient of H_2O (0.1% TFA)/MeOH (0.1% TFA) from 30 to 80% of MeOH (0.1% TFA) in 32 min at flow rate of 14 mL/min. The analysis and purity determination of the fractions was evaluated by analytical RP-HPLC on a VWR Hitachi – Elite LaChrom system equipped with Hitachi diode array detector L-2450 using an Eclipse XDB C18 column (4.6 x 150 mm, 5 µm). The collected fractions containing the peptides were freeze-dried. Identity and purity of the compounds were assessed by a Sciex API 4000 mass spectrometer (Applied Biosystems, Foster City, CA) and a Pump 22 Infusion (Harvard Apparatus), (by direct infusion.) MS scan from 50 to 2000 Da was used to monitor compound.

3. Bioconjugation reactions

3.1 Amide coupling of MNC2 with TZ

The conjugation reaction was performed at room temperature as follows. EDC·HCl (1.9 mg, 10 µmol) and Sulfo-NHS (5.42 mg, 25 µmol) were dissolved in MNC2 water suspension (800 µg, 0.8 mg mL^{-1}, pH 5) under vigorously magnetic stirring. After the activation of the carboxylic acid (approximately 15 min), purified TZ (48 µL, 33.3 mg mL^{-1}) was added to this solution. Next, the pH of the reaction system was adjusted to 7.4 using 1 M NaOH. The reaction lasted overnight at RT under magnetic stirring. At the end

of the reaction, the particulate was precipitated by centrifugation at 6000 rpm for 10 min and the supernatant was discarded; in order to remove the unbound antibodies, the resultant particulate was washed three times (3 × 1 mL) with phosphate buffered saline solution (PBS: 10 mM phosphate, 300 mM NaCl, 2.7 mM KCl, pH 7.4). Finally, the product was redispersed in the same PBS (1 mL) and stored at 4 °C before further experiments.

3.1.1 Determining TZ loading on nanoparticles surface

Fe_3O_4 nanoparticles were spherical in shape with an average radius of about 5 nm; the average volume of nanoparticles was 5.23 10^{-25} m^3 and the density of magnetite was 5 10^6 g m^{-3}; the mass of a single nanoparticle that is 2.615 10^{-18} g. Hence, 1 mg of Fe_3O_4 contains 3.824 10^{14} nanoparticles. The amount of antibodies appended on nanoparticles surface was determined by using a Bradford Protein Assay. According this method and the curve calibration standard elaborated at different concentation of the antibody, we estabilished that 217 µg of TZ were loaded on 1 mg of MNC2. In 217 µg of TZ (*MW*= 150 Kda) there are 8.71 10^{14} molecules of antibody for 1 mg of nanoparticles. In conclusion, 2 molecules of TZ per nanoparticle were statistically determined.

3.2 Conjugation of SNAP-scFv800E6 to MFN2

Purified SNAp-scFv800E6 (0.3 mg) with MFN2 (2mg) in PBS, pH 7.4 (1 mL), in the presence of 1 mM DTT, were incubated overnight at 4 °C. Next, unconjugated SNAP-scFv was removed by centrifuging the mixture in amicon YM-100 tubes and the concentrated particles were washed three times with PBS (5 mL).

3.3 Synthesis of MNP-H and MNP-H11

MNP3 (2 mg) were incubated 1 h at RT under shaking with 2 mg of HALO_FITC. Then, unconjugated HALO_FITC was removed by centrifugation of the sample with Amicon YM-100. Resultant MNP-H were washed three times in Amicon YM-100 with PBS buffer. The amount of HALO_FITC immobilized onto MNP3 was determined by measuring fluorescence emission of the sample exciting at 488 nm, using the standard curve reported in **Fig.10**.

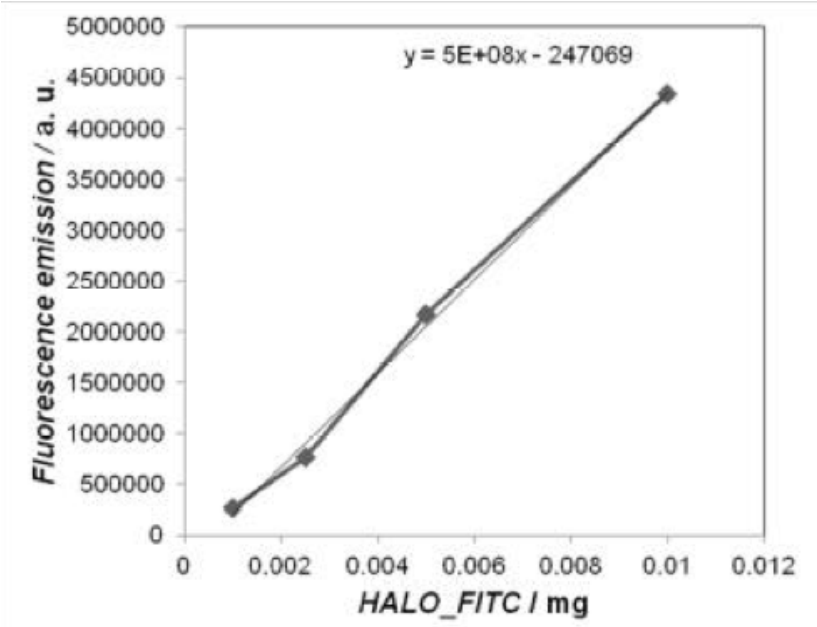

Fig.10 Standard curve obtained measuring fluorescence emission at 514 nm (excitation 488 Fluorescence emission spectrum obtained nm) of HALO_FITC different amounts.

3.4 Synthesis of MNP-CUT and MNP-CUT-U11.

MNP3 (250 µg) were incubated 1h at room temperature under shaking with 125 µg of CUT-FITC or CUT-U11-FITC in PBS/BSA 0.3%. Then, unconjugated protein was removed by centrifugation of the sample with Amicon YM-100. MNP-CUT and MNP-CUT-U11 were washed three times in Amicon YM-100 using PBS buffer. The amount of immobilized protein onto MNP3 was determined by measuring fluorescence emission of the sample exciting at 488 nm, using the standard curve reported in **Fig.11**.

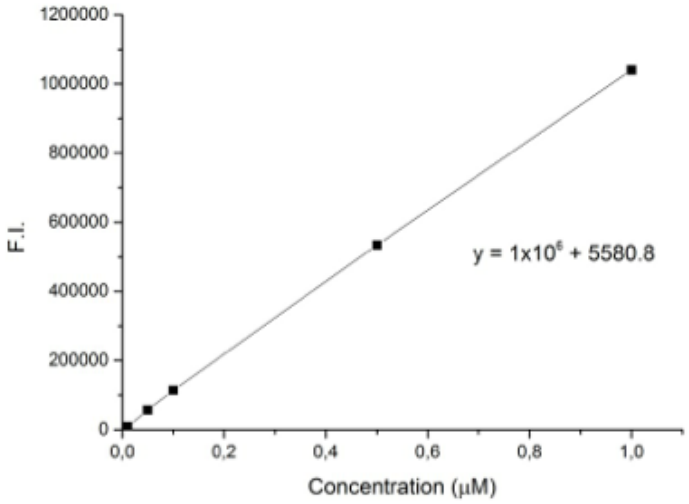

Fig.11 Standard curve of concentration for CUT-U11-FITC.

3.5 Gold nanoparticles functionalization with U11 peptide

The functionalization of Au-citrate NPs with peptides, FITC and PEG ligands was carried out following a procedure described by Levy et al.[147] For this purpose, a PEG-SH ($HS\text{-}C_{11}\text{-}(EG)_4\text{-}OH$) was dissolved in methanol to give 14.7 mM stock solution. U11 and U11 scrambled peptides were dissolved in mQ water to give 0.7 mM stock solutions, which were stored at –20 °C. $HOOC\text{-}(CH_2)_{10}\text{-}S\text{-}S\text{-}(CH_2)_{10}\text{-}CONH\text{-}FITC$ was dissolved in methanol to give 1.62 mM stock solution, which was stored away from direct sunlight. The ligands were pre-mixed in desired proportions in methanol and added quickly under vigorous stirring to 30 mL of Au-citrate NPs dispersion of known concentration. The ligands were allowed to attach to the particles overnight, followed by washing by repeated centrifugation at 13500 rpm for 20 min at 4 °C.

3.6 Gold nanoparticles functionalization with peptides 1-4

The modification of AuNPs with peptides and PEG ligands was carried out following a procedure described by Levy *et al.*[147] For this purpose, 11-mercaptoundecyl-tetra(ethylene glycol), (PEG-SH) was dissolved in methanol to give 14.7 mM stock solution. $NHS\text{-}PEG_8$-maleimide linker was dissolved in DMSO to give 0.3 M solution, which was then diluted with methanol to give 3mM stock solution which was stored at −20 °C. Finally, cystamine was dissolved in mQ water to give 1 mM stock solution, while

peptides were dissolved in methanol at a 1 mM concentration. Methanolic PEG and cystamine solution (86.6 µL and 19.7 µL, respectively) were mixed and quickly added to 50 mL of 1.28 nM AuNPs dispersion, under vigorous stirring. The ligands were allowed to attach to the particles overnight, followed by washing by repeated centrifugation at 13500 rpm for 20 min at 10 °C. Afterwards, 65.2 µL of NHS-PEG_8-maleimide solution was added to the NPs and allowed to react for 2 h at room temperature. After a second purification, 196.8 µL of peptide solution (5-fold excess) were added to react with NPs overnight at room temperature. The final purified NPs were filtered using a 0.45 µm Millipore filter before use, and characterized by UV-vis and fluorescence spectroscopy, TEM, dynamic light scattering and ζ-potential.

4. Cell cultures

MCF-7 is an adenocarcinoma cell line that was first isolated in 1970 from the breast tissue of a 69-year old Caucasian woman. It was used as human breast cancer HER2 positive target. Also **MDA MB 468** cells are an adenocarcinoma cell lines. They were isolated from a 51-year old Black woman. They were used as HER2 negative and uPAR positive target. Promonocitic **U937** cell clones 13 and 10 were used as uPAR positive and uPAR negative targets, respectively. They were isolated from a 37-year old male. The **4T1** mouse mammary carcinoma is a transplantable tumor cell line that is highly tumorigenic and invasive. They were used as uPAR positive target. **CAL51** human breast cancer cells were used as uPAR negative target. **3T3-L1** murine fibroblast cell line was used as noncancerous control.

MCF-7, MDA MB 468, 4T1, CAL51 and 3T3-L1 cell lines were cultured in 50% Dulbecco's Modified Eagle's Medium High Glucose (DMEM-HG) and 50% F12, whereas U937 were cultured at 2×10^5 cells per mL in RPMI 1640 medium. Each medium were supplemented with 10% fetal bovine serum, L-glutamine (2 mM), penicillin (50 UI mL^{-1}), and streptomycin (50 mg mL^{-1}) and were cultured at 37 °C in a humidified atmosphere containing 5% CO_2 and subcultured prior to confluence using trypsin/EDTA.

5. Bioconjugates characterization

5.1 Immunoprecipitation assay

MCF-7 cells were lysed with lisys buffer containing 20 mM Tris HCl, 150 mM NaCl,

10 mM EGTA, 10% glycerol and 1% Triton X-100, pH 7.4 for 30 min at 4 °C and then centrifuged at 8500 rpm for 10 min to remove membranes and cell debris from protein fraction. Bradford assay was used to determine protein content of whole cell extract. Preclearing step was performed with 200 µL of PMNC (1 mg mL^{-1}) for 1 h on wheel at 4 °C. The immunoprecipitation was carried out with 1 mg of pre-cleared lysate and Tz-PEG-MNP (200 µL, 1 mg mL^{-1}, corresponding to 3.75 µg of linked-antibody) for 16 h at 4 °C on wheel. Samples were washed three times in lysis buffer and boiled in sodium dodecyl sulfate sample buffer containing 5% 2-mercaptoethanol to cleave the binding to the beads. Samples were run on 8% poliacrilammide gel. Proteins were blotted onto PVDF membranes and incubated in blocking solution (5% skim milk in TBS, 0.05% Tween) for 1 h at RT. For HER-2 detection, membranes were then probed for 1 h at RT using anti-HER-2 polyclonal antibodies (1:500 Millipore, Billerica, MA) in blocking solution. Specificity of the interaction between the HER-2 and TMNP was verified with immunoblot of immune-precipitated samples with unrelated proteins such as anti-Clnx pAb (1:500 Genetex) at RT for 1 h in TBS + 0.05% tween + 5% BSA. Specific HRP-conjugated secondary-antibodies were used always 1 h at RT (anti-mouse 1:10000 BioRad Cell Signaling, Danvers, MA). Immunoreactive bands were revealed using ECL Western blotting reagent E Healthcare).

5.2 Dot Blot Assay

Standard Minifold I dot blot apparatus were used in this assay. TZ or purified nanoparticle suspension were spotted onto PVDF membrane. After all samples were fixed the membrane was incubated in blocking solution (5% skim milk in PBS) for 60 min at RT. To evaluate TZ activity, membranes were then probed for 60 min at 25 °C using horseradish peroxidase-rabbit anti-human antibodies at a 1:1000 dilution in PBS buffer. Immunoreactive spots were revealed using ECL Western blotting reagent.

5.3 Confocal laser scanning microscopy

Cells were cultured on collagen pre-coated cover glass slides until sub-confluence and incubated with nanoparticles, for different time periods at different concentrations. Cells were washed with phosphate-buffered saline (PBS, EuroClone), fixed for 5 min with 4% paraformaldehyde (Sigma) and then treated for 10 min with Triton 0.01%. A blocking step was performed for 1 h at RT with a solution containing 2% bovine serum albumin

(BSA, Sigma), 2% goat serum and 0.2 µg mL^{-1} DAPI (4',6-diamino-2-phenylindole) in PBS. For TMNP binding experiments, MCF-7 cells were incubated 20 min with 100 µg mL^{-1} of TMNP or with 11 µg mL^{-1} of free TZ. TMNP and TZ were revealed by a FITC-conjugated antibody to whole murine IgG (MP Biomedicals) at a 1:300 dilution by incubating for 2 h at RT. As negative control, MCF-7 cells were incubated solely with the secondary antibody anti-human FITC. To test the SNAP-scFv binding capability, MCF-7 cells were incubated 1 h at 37 °C with 100 µg mL^{-1} of SSMFN or with 20 µg mL^{-1} of free SNAP-scFv. ScFv was revealed by a FITC-conjugated antibody to whole murine IgG (MP Biomedicals) at a 1:300 dilution by incubating for 2 h at RT. U937 uPAR-positive cells (clone 13) and U937 uPAR-negative cells (clone 10), as negative control, were incubated 1 h at 37 °C with 0.1 mg mL^{-1} of MNP-H11. UPAR expression was assayed on U937_13 cells by 15 min incubation at 25 °C with an anti-uPAR (American 63iagnostic) at a 1:200 dilution. Anti-uPAR was revealed after a 15 min incubation at 25 °C using an anti-mouse secondary antibody conjugated with Alexa Fluor 488 (Invitrogen) at a 1:300 dilution. Finally, MDA-MB-468 cells were incubated for 1 h and with 100 µg of MFP-CU11 or 100 µg of MFP-CUT. MDA MB 468 cells were incubated 1 h at 37 °C with 2 nM of both AuNPs (**1)** and Au-(**5**) nanoparticles. Microscopy analysis was performed with a Leica SP2 AOBs microscope confocal system. Images were acquired with 63× magnification oil immersion lenses at 1024×1024 pixel resolution.

5.4 Flow cytometry

Cells (5×10^5) were incubated 2 h at 4 °C in flow cytometry tubes in the presence of each bioconjugates, at different concentrations. After incubation, cells were washed three times with PBS. Labeleb cells were resuspended with 0.5 mL of PBS and analyzed by a FACS Calibur flow cytometry (Becton Dickinson). 20000 events were acquired for each analysis, after gating on viable cells, and a sample of untreated cells was used to set the appropriate gates. SSMFN and MNP-H11were incubated at a concentration of 20 µg mL^{-1} or 100 µg mL^{-1}, whereas pegylated MNP1 (P-MNP) at 20 µg mL^{-1} and HALO at 40 ng mL^{-1}. AuNPs (**1)** and Au-(**5)** nanoparticles were incubated at final concentrations of 0.5, 2 and 4 nM, respectively. Finally free peptides and Au-peptide NPs were used at final concentrations of 1 µg or 10 µg, and 4 nM or 8 nM, respectively.

5.5 Cell death assay

Cells were cultured on a 12 multiwell dish until sub-confluence. The cells were incubated for 1, 3 and 24 h at 37 °C in the presence of different amount of each bioconjugates. After incubation, cells were washed twice in PBS and treated for flow cytometry analysis according to instructions of Annexin V-PE-Cy5 Apoptosis Detection Kit manufacturer's protocol (BioVision Incorporated). Briefly, cells were resuspended in Binding Buffer 1× and incubated for 5 min in presence of 5 µL of Annexin-PE. Subsequently, cells were analyzed on a FACS Calibur flow cytometer (Becton Dickinson). 20000 events were acquired for each analysis, after gating on viable cells. Therefore, we consider cell death as populations positive for Annexin V. The assay was performed in triplicate and the results were expressed as mean values ± standard deviation. SSMFN and MNP-H11 were incubated at a concentration of 20 µg mL^{-1} or 100 µg mL^{-1}. AuNPs (**1)** and Au-(**5)** nanoparticles were incubated at final concentrations of 0.5, 2 and 4 nM, respectively. Finally free peptides and Au-peptide NPs were used at final concentrations of 1 µg or 10 µg, and 4 nM or 8 nM, respectively.

5.6 Cell proliferation assay

Cells were cultured on a 96 multiwell dish at a density of 5000 cells cm^{-1}. Then cells were incubated with each bioconjugates at different concentrations. At the indicated time points, cells were washed with PBS and then incubated for 3 h at 37 °C with 0.1 mL of 3-(4,5-dimethyl-2-thiazolyl)-2,5-diphenyl-2H-tetrazolium bromide (MTT) stock solution previously diluted 1:10 in DMEM medium without phenol red. At the end of the incubation, 0.1 mL of MTT Solubilizing Solution was added to each well to solubilize the MTT formazan crystals (Sigma-Aldrich). Absorbances were read immediately in a BIORAD Microplate reader using a test wavelength of 570 nm and a reference wavelength of 690 nm. The results are expressed as means ± standard deviation of the mean of 5 individual experiments. SSMFN and MNP-H11 were incubated at a concentration of 20 µg mL^{-1} or 100 µg mL^{-1}, AuNPs (**1)** and Au-(**5)** nanoparticles were incubated at final concentrations of 0.5, 2 and 4 nM, respectively. Finally free peptides and Au-peptide NPs were used at final concentrations of 1 µg or 10 µg, and 4 nM or 8 nM, respectively.

5.7 Transmission electron microscopy

MDA-MB-468 cells were incubated for 4 h with 40 µg of MNP-CU11 and 40 µg of MNP-CUT. After incubation time, cell pellets were washed in PBS (5 min, twice), fixed in 2.5% glutaraldehyde (Electron Microscopy Sciences), 0.1 M phosphate buffer, pH 7.2, for 2 h. After one rinse with phosphate buffer, specimens were postfixed in 1.5% osmium tetroxide (Electron Microscopy Sciences) for 2 h, dehydrated by 70, 90, and 100% EtOH, and embedded in epoxy resin (PolyBed 812 Polysciences Inc. USA). Ultrathin sections were stained with uranyl acetate and lead citrate and examined by means of TEM (Zeiss EM109).

Results and discussions

1. Investigating the structural biofunctionality of antibodies conjugated to magnetic nanoparticles

The conjugation of nanoparticles with monoclonal antibodies (mAbs) is a well-established strategy to deliver the nanoprobe to specific cell types. This approach combines the unique physical properties of nanoparticles, with the specific and selective recognition capability of mAbs or other proteins to cells and tissues. However, despite the huge interest for mAb nanoconjugates, only poor evidence is currently available on the actual preservation of the protein biofunctionality at the molecular level, once mAb has been covalently conjugated to the nanoparticles. Such difficulty mainly resides in the lack of reliable methods capable of providing exhaustive information on structural/conformational features sustaining the protein functionalities of bioconjugate systems.

The purpose of the study presented in this thesis is investigating how and what IgG immobilization onto the surface of iron oxide nanoparticles may preserve the structural bioactivity as, deduced by accurate analysis of the essential folding features obtained by Fourier-transform infrared (FTIR) spectroscopy. In this study we used Trastuzumab (TZ), which is a recombinant, humanized IgG mAb selectively binding with high affinity to the

extracellular domain of the human epidermal growth factor receptor 2 (HER2). HER2 is expressed in several primary tumors, including breast, ovarian, gastric and salivary cancers, and in metastatic sites.[148] For this reason, TZ has been developed for clinical immunotherapy and the conjugation of TZ with chemotherapeutics may offer an excellent strategy for targeted delivery of drugs malignant cells.[149]

1.1 MNC synthesis and characterization

Bare monodisperse magnetite nanoparticles (MNC1) were obtained by aqueous alkaline coprecipitation of Fe^{2+} and Fe^{3+} ions in 1 : 2 molar ratio, as described by Polito et all.[150] A bifunctional linker α-ω-dicarboxyl-terminated polyethylene glycol (PEG, M_W 600 Da) was grafted on the Fe_3O_4 surface by ultrasound-assisted reaction and the unreacted excess of PEG was removed by dialysis. The synthesized carboxyPEG-functionalized nanoparticles (MNC2) were highly soluble in water, thus the MNC2 suspension was diluted to a final concentration of 1 mg mL^{-1}, which was stable for several months at room temperature. PEG-coated nanoparticles are more biodegradable, non-antigenic, non-irritative to tissues and less toxic than unmodified nanoparticles.[151-153] At the same time, the PEG chains are responsible for the so-called ‘‘stealth effect’’, preventing nonspecific adsorption of opsonin proteins.[154] TEM image showed that the core size of MNC2 was unchanged after PEG grafting (10 ± 3 nm, **Fig. 12**). The hydrodynamic diameter of MNC2 was determined to be 82.4 ± 1.0 nm by Dynamic Light Scattering (DLS). A good contrast power for MNC2 in PBS was deduced by the relaxivity value r_2, which was calculated to be 131.9 $mM^{-1}s^{-1}$. The pH-dependent stability of MNC2 in water was also investigated by UV-vis absorption spectra. MNC2 were dispersed in deionized water and evaluated in the pH range from 1 to 11, in which they did not display any aggregation up to pH 7–8. A critical formation of large clusters of nanoparticles was instead observed above pH 9 after 90 min incubation, which resulted in collapsing of the colloidal suspension (**Fig. 13**). Zeta potential (ζ) of MNC2 in water in the range of pH between 3 and 9 was also investigated. At pH 3, MNC2 were strongly positively charged with ζ = +42.0 ± 3.2 mV (probably due to a tendency of PEG to capture protons). In contrast, at pH 9, MNC2 exhibited a strongly negative surface charge of ζ = −43.3 ± 1.3 mV, confirming the presence of completely deprotonated carboxylate groups on the external surface of nanoparticles. Similar results were obtained in PBS: as expected, in this case, MNC2 were less negatively charged, with ζ = −19.5 0.5 mV.

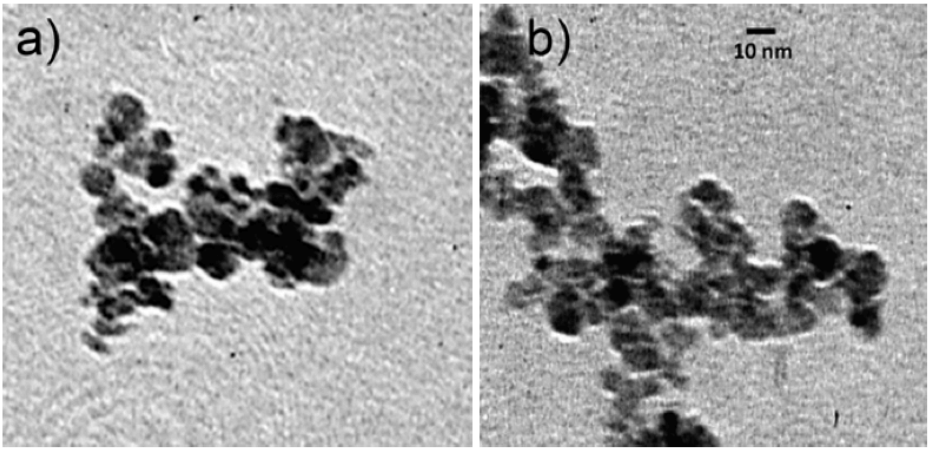

Fig. 12 TEM images of a) MNC1 synthesized by the coprecipitation method and b) MNC2 obtained by reaction of MNC1 with polyethylene glycol 600 diacid. For TEM analyses, the nanoparticles were dispersed under sonication in ethanol (50 μg mL^{-1}) and a drop of the resulting solution was placed on a Formvar/carbon-coated copper grid and air-dried.

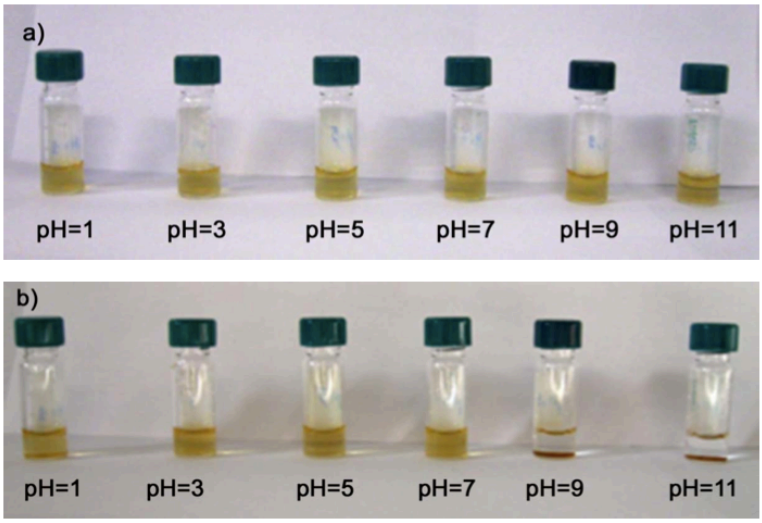

Fig. 13 MNC2 solutions (0.1 mg mL^{-1}) in deionized water at different pH values. A) Freshly prepared solutions and b) after 90 min.

1.2 MNC2 functionalization: TMNP

MNC2 were ready for conjugation with amine-containing biomolecules by amide coupling owing to the high surface density of carboxyl functionalities. To examine their potential in mAb conjugation, purified TZ was covalently bound to MNC2 at pH 7.4 in the

presence of coupling agents, such as sulfo-NHS and EDC, exploiting the lysine amine groups present on the peptide sequence of the antibody (**Scheme 1**).

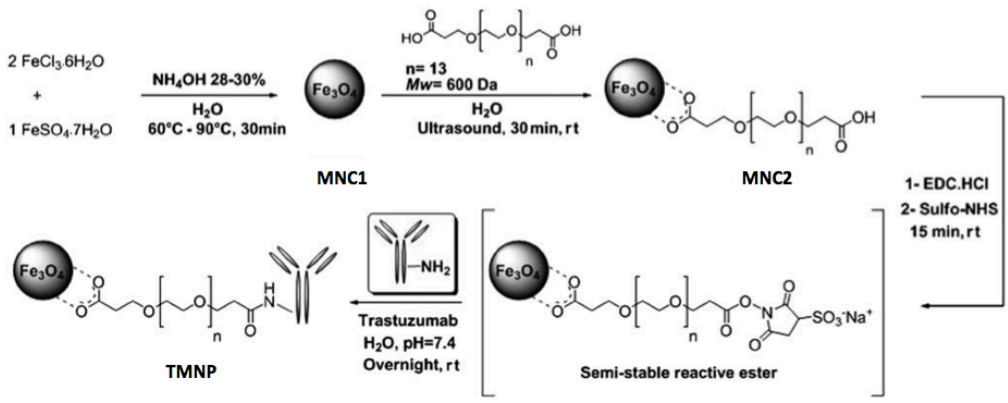

Scheme 1 Schematic representation of the synthesis of pegylated Trastuzumab-modified iron oxide nanoparticles (TMNP).

The resulting TMNP were washed with PBS to remove unbound antibodies, which would lead to false-positives in biological experiments, resuspended in PBS at a final concentration of 0.8 mg mL^{-1} and stored at 4 °C. The average number of TZ loaded on TMNP was estimated to be about 2 mAb per nanoparticle by a Bradford protein assay. The hydrodynamic size of TMNP was 224.9 ± 2.7 nm, which was remarkably higher than that of MNC2. Only a slight decrease in relaxivity was observed (**Table 3**). In addition, ζ values showed a marked decrease in negative charge to ζ = 7.8 ± 1.1 mV, which demonstrated that several carboxylate groups from the surface PEG chains were involved in the linkage with TZ, and the residual negative charges were partially compensated by positive charges on the IgG molecule, consistent with the basic isoelectric point of TZ (IP_{TZ} = 8.45). The physical/chemical characteristics of MNC2 and TMNP are summarized in **Table 3**.

Table 3 Comparison between physico-chemical characteristic of MNC2 and TMNP.

Parameter	Unit	MNC2	TMNP
Hydrodynamic diameter (DLS)	nm	82.2 ± 1	225 ± 3
Z-potential	mV	−19.5 ± 0.5	− 7.8 ± 1.1
T_2 relaxivity (r_2)	$mM^{-1}\,s^{-1}$	132	103

An important prerequisite to be kept in mind when designing an appropriate conjugation strategy is maintaining intact, as much as possible, the biological activity and full receptor binding capability of immobilized mAbs. We had a first immediate evidence of the immunoreactivity of mAbs in TMNP performing a dot blot analysis (**Fig. 14**). Our results confirmed that TMNP were able to crossreact with anti-human antibody with the same sensitivity of free TZ.

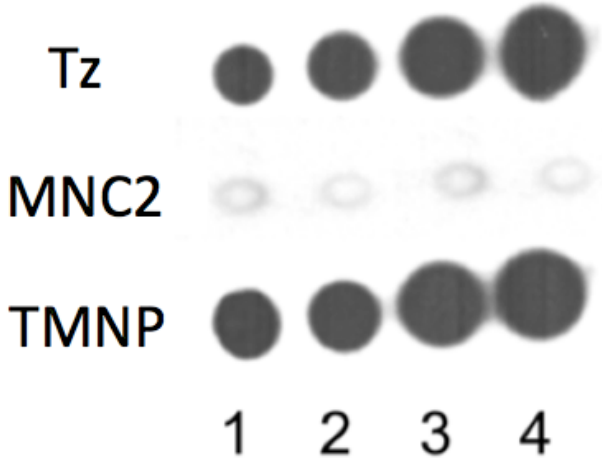

Fig. 14 Immunodot blot assays carried out in parallel with increasing amount (1, 50 ng; 2, 100 ng; 3, 200 ng; 4, 300 ng) of soluble and immobilized (TMNP) trastuzumab. Pegylated nanoparticles (MNC2) were the negative control. TMNP were incubated with anti-human antibodies conjugated with horseradish peroxidase (HRP-rabbit) at a 1:1000 dilution in PBS buffer. The immunoreaction was revealed by a strong signal using ECL western blotting as reagent.

1.3 Structural analysis of immobilized TZ

In order to explore the structural properties of the conjugated antibody, we used FTIR spectroscopy to obtain information on protein secondary structure.[155,156] In **Fig. 15 a**, the absorption spectra of free TZ (A), of a mixture of MNC2 and free TZ (B), of TMNP (C), and of MNC2 (D) are reported in the 1500–1700 cm^{-1} spectral region, where the amide I and amide II bands occur. These bands are due to the absorption of the C=O stretching and N–H bending vibrations of the protein backbone, respectively.[155,156] The presence of these two bands in the TMNP spectrum confirmed that the conjugation reaction occurred successfully. Indeed, unconjugated MNC2 displayed a completely different profile in this spectral region, with only a broad absorption centered at about

1606 cm^{-1}.

Information on the secondary structure of the protein can be obtained through the analysis of the amide I band, as it is the spectral region most sensitive to the structural conformation changes of the protein.[156] In order to resolve the amide I band components, we performed the second derivatives of the measured spectra (**Fig. 15 b**).[155] The spectrum of freshly purified TZ is dominated by two main components, which appear as negative peaks in the second derivative, at 1692 cm^{-1} and 1641 cm^{-1} that can be both assigned to the native β-sheet structure of the protein.[156] The spectrum of TMNP was almost identical to that of free TZ under native condition indicating that the amidic conjugation used in this work did not affect significantly the protein secondary structure. To monitor the stability of the conjugated mAb, we collected the FTIR spectra of the samples at different times of incubation up to 96 h at 37 °C. The comparison of the FTIR second derivative spectra of native TZ at the beginning of incubation with that after 96 h indicates that the protein secondary structures were substantially unchanged. The same result was obtained for conjugated TZ after incubation at 37 °C. We tested the storage stability of TMNP, and found that conjugated TZ was stable even after two months of incubation at 4 °C without any additional stabilizing agents.

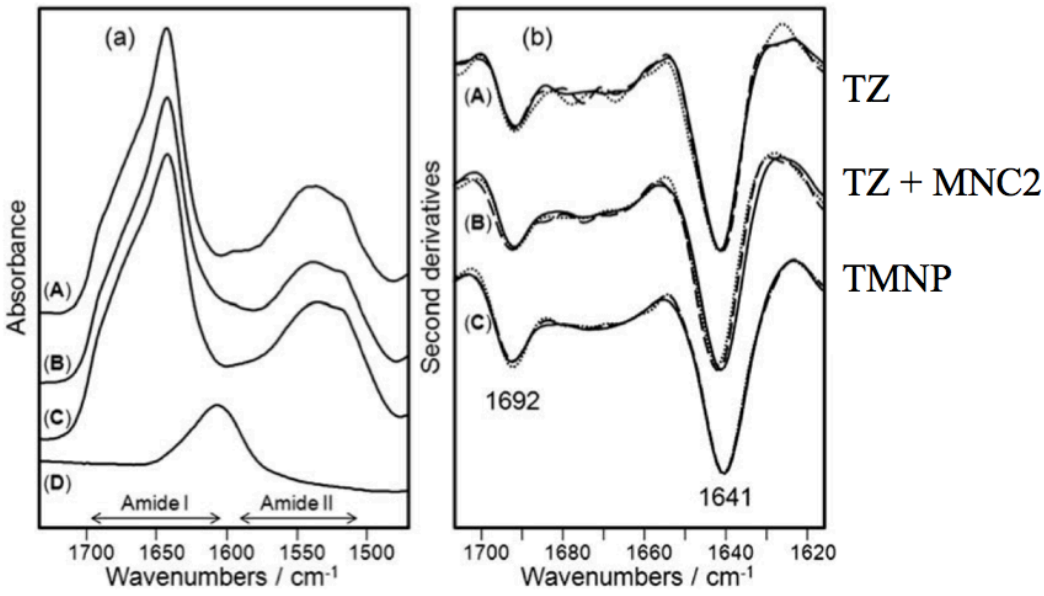

Fig. 15 Structural characterization of TZ, TMNP, and MNC2 by FTIR spectroscopy. (a) FTIR absorption spectra

in the amide I and amide II regions of (A) free TZ at 1.0 mg mL^{-1}, (B) a mixture of free TZ at 1.0 mg mL^{-1} and free MNC2 at 4.7 mg mL^{-1}, (C) TMNP at 4.7 mg mL^{-1} (1.0 mg mL^{-1} TZ), and (D) MNC2 at 7.0 mg mL^{-1}. In this spectral region, MNC2 (D) displayed only a broad absorption around 1606 cm^{-1}, while TMNP (C) showed the protein amide I and amide II bands confirming the success of the bioconjugation. The spectra were collected immediately after sample preparation. (b) Second derivatives of the spectra reported in (a). Spectra were collected at time 0 (continuous lines), after 24 h (dashed lines), and after 96 h (dotted lines) of incubation at 37 °C. The spectra are dominated by two components at 1692 cm^{-1} and 1641 cm^{-1} assigned to the native b-sheet structure of TZ that were found to be stable upon incubation at 37 °C both in the free and in the bioconjugated protein.

Next, we examined the FTIR absorption of all the mentioned samples after lyophilization and resuspension in buffered heavy water (PBS/D_2O), pH 7.4, to simulate the physiological environment. In this way, it was possible to monitor in real time the stability of the conjugated antibodies by transmission FTIR at 37 °C, exploiting the low absorbance of D_2O in the amide I region. These results confirmed once again that conjugation did not affect the native protein secondary structure, which was found to be stable over 24 h incubation at 37 °C (data not shown). Altogether, these data provide compelling evidence of the preserved stability of mAb in TMNP system and demonstrate that under these synthetic conditions the conjugated protein did not change its physiological biofunctionality.

To quantitatively assess the secondary structure components of the conjugated antibodies, we performed a Gaussian curve fitting of the absorption spectra of free TZ and of TMNP, whose results are reported in **Fig. 16**. The relative weights of the β-sheet components (1641 and 1692 cm^{-1}) and of the random coil component (R.c. 1663 cm^{-1}) were very similar, with only minor differences. In particular, TMNP seems to display a slightly larger R.c. that could account for a partially reduced bioactivity. Next, we examined the infrared absorption spectra of TZ physically adsorbed on bare MNC1 (**Fig. 16** and **Fig. 17**). As expected, the bioactivity of the antibody was strongly reduced. The spectra were very different in the amide I band, whose maximum shifted from 1641 cm^{-1} for free TZ to 1650 cm^{-1} for adsorbed TZ. Indeed, the Gaussian curve fitting of these spectra indicates a strong change in the antibody secondary structures. The β-sheet components were reduced from ~50% in free TZ to ~34% in the adsorbed TZ immediately after preparation, and to ~22% after 96 h incubation at 37 °C. R.c. increased from ~44% in free TZ to ~55% and ~66% in the adsorbed TZ at 0 and 96 h incubation,

respectively. In this case, the loss of native secondary structure predicted by the above FTIR analysis is in agreement with the decreased bioactivity observed for the adsorbed TZ.

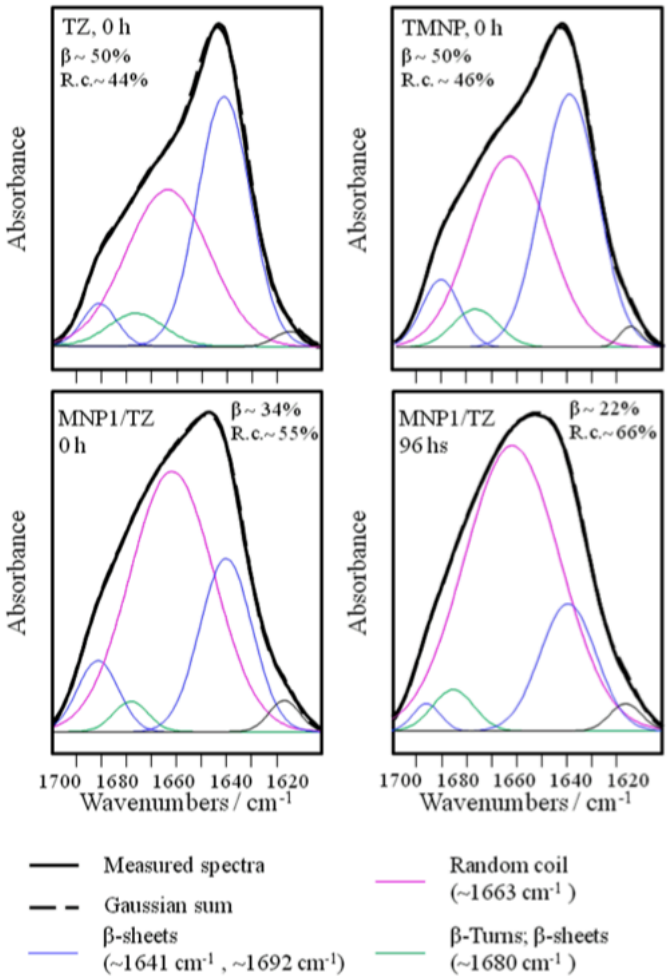

Fig. 16 Gaussian curve fitting of the absorption spectra in the Amide I region of free TZ, of TMNP, and of TZ adsorbed to MNC1 immediately after preparation and after 96 h of incubation at 37 °C. The β-sheet components are reported in blue and their percentage weights over the total Amide I band are indicated. The component peaked at ~1663 cm^{-1} (reported in pink) is mainly due to random coil structures (R.c.) with possible contribution of β-turns. The curve fitting of the measured spectra into Gaussian function was performed following the method previously described.

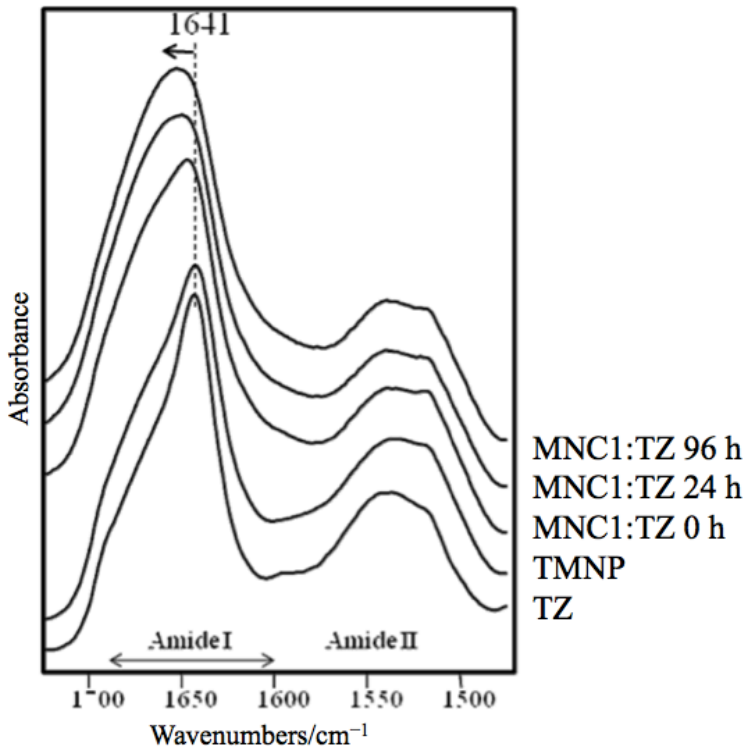

Fig. 17 FTIR absorption spectra of free TZ, of TMNP, and of TZ adsorbed to MNC1 at different times of incubation at 37 °C (0, 24, and 96 hours). The maximum of the Amide I band shifts from 1641 cm^{-1} in the free TZ to 1650 cm^{-1} in the adsorbed TZ at 96 hours of incubation, consistent with a gradual unfolding of protein secondary structure.

1.4 TMNP target capability

To check whether TMNP were able to maintain effectively the specific targeting capability of TZ for HER2-positive breast cancer cells, we investigated the TMNP binding to HER2 in HER2-overexpressed MCF7 cells.[158] Two MCF7 whole cell extracts were incubated in parallel at 4 °C with TMNP and with unconjugated MNC2 (control), respectively. Immunoprecipitates (bound) and the supernatants (unbound) were first analyzed by western blotting with anti-HER2 antibody in order to reveal TMNP binding to HER2 receptor (**Fig. 18**, upper). The comparison between TMNP and MNC2 confirmed that the conjugation with TZ was necessary to immunoprecipitate the HER2 membrane receptor in MCF7 whole cell extracts. Calnexin (Clnx), an integral protein of the endoplasmic reticulum, was tested as negative control to assess the possible nonspecific interaction of TMNP with undesired biomolecules using a labeled anti-Clnx mAb, which

displayed a detectable signal only in unbound sample (**Fig. 18**, lower). This suggests that the interaction between TMNP and HER2 is specific.

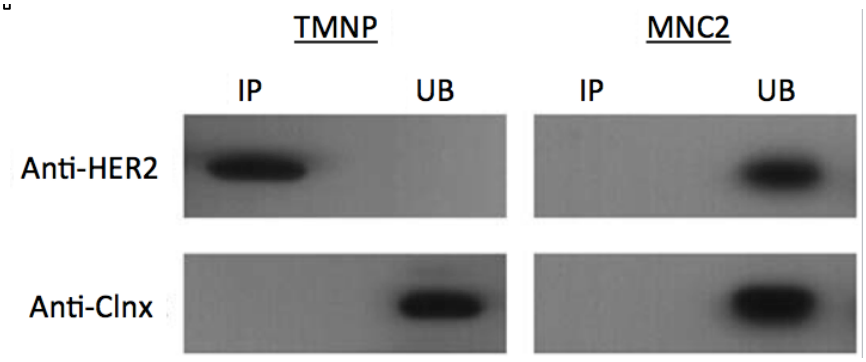

Fig. 18 Immunoprecipitation of HER2 in MCF7 cells. Immunoprecipitation was performed using anti-HER2 or anti-calnexin antibodies cross- linked to TMNP and MNC2 (as negative control). Nanoparticles were incubated overnight at 4 °C in a whole extract of MCF7 cells. Bound (IP) and unbound (UB) proteins were eluted in SDS-PAGE application buffer, electrophoresed and immunoblotted. Clnx: calnezin.

Immunoprecipitation data were confirmed by relaxivity measurements, which provided evidence on iron oxide capture by MCF7, and by immunofluorescence after TMNP incubation with living cells. Since HER2 is a trans-membrane receptor, TMNP were expected to localize to the membrane of HER2-positive MCF7 cells. In order to assess HER2 surface distribution, MCF7 cells were first treated with either TZ (**Fig. 19 d–f**) or TMNP. Next, TZ and TMNP were labeled with anti-human FITC-labeled secondary antibodies (green), whereas cell membranes were stained with DiD oil (mb, blue). After 20 min incubation at 37 °C, TMNP were observed on MCF7 cell surfaces (**Fig. 19 a–c**), demonstrating that they localized selectively to trans-membrane receptors. The combined results of these experiments clearly evidences the target-selectivity of TMNP towards HER2 breast cancer marker.

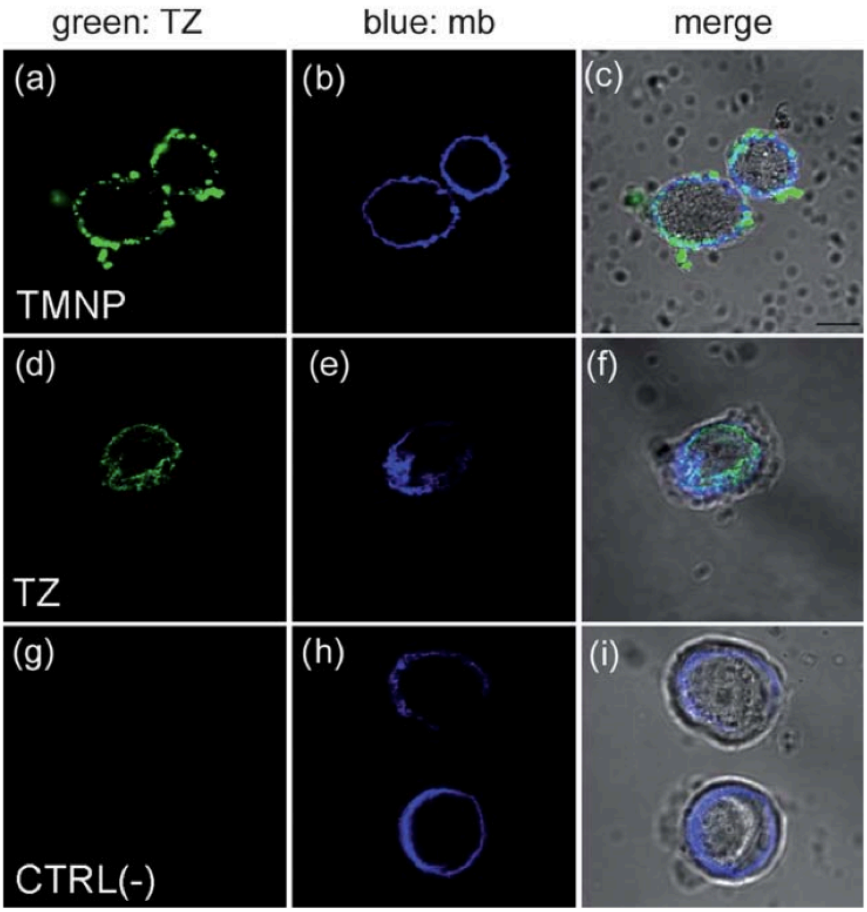

Fig. 19 Confocal laser images of MCF7 cells cultured with TMNP or free TZ. MCF7 were incubated for 20 min with TMNP (100 mg mL^{-1}; a–c) or TZ (11 mg mL^{-1}; d–f). As negative control, MCF7 were stained with secondary antibodies anti-human FITC (g–i). Cell membranes (mb) were stained with DiD oil (blue). TMNP and TZ were labeled with anti-human FITC secondary antibodies.

2. Conjugation of biological molecules in an oriented manner on nanoparticles for breast cancer cells targeting

Multifunctional iron oxide nanoparticles (MNP) find increasing applications in nanomedicine, in particular MNP could be utilized as noninvasive clinical imaging method for diagnosis and treatment of malignant diseases.[159,160] Great efforts have been made to develop efficient target-oriented contrast agents. In this context, the use of MNP combining the emission of detectable optical and magnetic signals and focused targeting action is attracting broad interest in noninvasive cancer diagnosis (both *in vitro* and *in*

vivo).[76,161] The selective recognition of specific cancer cells is of primary importance and is usually achieved exploiting the modification of MNP with biomolecules endowed with high affinity for specific cell membrane receptors.[162,163] A protein's to recognize the respective receptor whilst being conjugated to MNP surface, is an important feature to be considered; in this way the specific peptide chosen would be engineered to achieve an oriented attachment. This characteristic determines bioactivity, avidity and targeting efficiency of the functionalized MNP; moreover, the possibility to control the ligand/peptide orientation on the nanoparticle surface, is a fundamental step to optimize receptor recognition.[164-166]

An elegant strategy involves the use of fusion proteins containing a small enzyme capable of irreversibly cross-coupling with a suicide inhibitor anchored to the solid surface. The enzyme is defined "capture protein" because it covalently and selectively reacts with the linker immobilized on the MNP. This approach optimized the orientation-controlled display of the peptide onto the MNP surface without any artificial chemical reaction, but through an enzymatic conjugation.[167,168] In this way the ligand of biological interest is always oriented in the correct way.[169,170] This novel approach presents several advantages: 1) protein attachment has a uniform orientation and allows a maximum protein functionality, 2) the immobilized ligand is a small molecule, 3) the system is applicable on a wide range of proteins and the active site can be (genetically) engineered in order to introduce a specific sequence for protein immobilization, 4) the nature of the enzymatic ligation is highly specific and irreversible; in addition, the reaction occurs quickly under physiological conditions thus preventing protein structure degradation or denaturation.[171]

Here three strategies involving engineered proteins consisting of a "capture protein", genetically fused with a small peptide involved in biological target, have been adopted. We used a SNAP tag fused with an scFv antibody,[169] a HALO tag fused with the small U11 peptide,[170,172] and a cutinase enzyme also fused with the U11 peptide.

2.1 Protein oriented ligation on nanoparticles exploiting O_6-alkylguanine-DNA transferase (SNAP) genetically encoded fusion

SNAP is a small enzyme that irreversibly transfers the alkyl group from its substrate, O_6-alkylguanine-DNA, to one of its cysteine residues (**Scheme 2**).[172] However, it has been demonstrated that SNAP is highly reactive also toward alternative non-natural

nucleobases, including O_6-methyl- and O_6-benzylguanine derivatives.[173] Such aggressive reactivity toward simple molecules is particularly attractive for nanoparticle biofunctionalization. Therefore, we reasoned that a PEGylated O_6-alkylguanine derivative could be a good candidate to mediate the covalent, site-specific immobilization of SNAP fusion proteins on MFN.

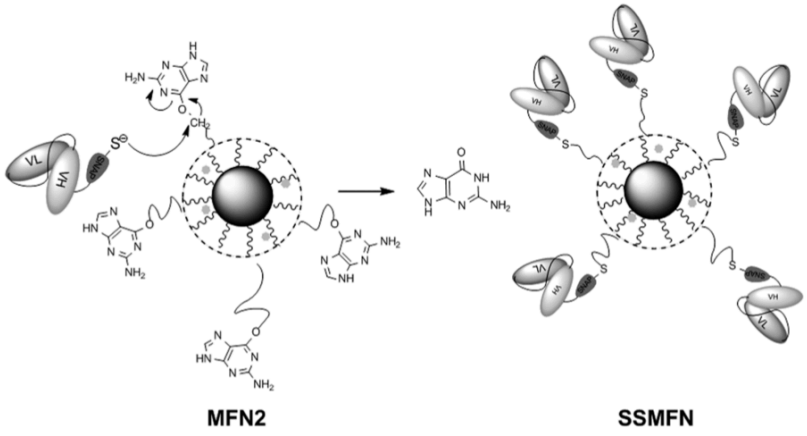

Scheme 2 Mechanism of SNAP-mediated immobilization of sCfv on MFN.

We designed a bimodular genetic fusion (SNAP-scFv) comprising a bioactive scFv mutant selective for HER2 receptor in breast cancer cells as a targeting module. ScFv is a small (20-30 kDa) antibody fragment consisting of a variable V_H and V_L regions of a monoclonal antibody connected throught a syntetic loop. Their monovalent binding reduce their affinity and specificity for the antigen, so reduce their potential in cancer diagnosis and therapy. As multimerization has been shown to enhance the affinity of scFvs toward the respective antigens, their conjugation to 3D-shaped nanostructures is expected to improve significantly their efficiency in targeting specific cell membrane receptors. In this work we used a scFv800E6 variant of anti-HER2 monoclonal antibody.

2.1.1 SNAP-scFv protein production in Pichia pastoris

The scFv800E6 sequence was modified inserting a DNA sequence in a pPICZαA vector encoding for SNAP at the N-terminal position using *EcoRI* restriction site. The modified gene was used to electroporate two different *P. pastoris* host strains, KM71H and GS115. Four scFv-SNAP best expressing clones were selected for medium-scale culture experiment, two from KM71H and two from GS115

strains. GS115/pPICZαA/SNAP/scFv800E6-1 clone was chosen as best producer and used for optimization of scFv-SNAP expression. The highest expression level was obtained in the presence of 0.5% methanol and 2% dextrose after 48 h of induction. Secreted scFv-SNAP containing a *C*-terminal 6×His tag was purified from medium by a single purification step onto Ni-NTA agarose column in 1.5 mg mL^{-1} yield.

2.1.2 MFN synthesis

Highly uniform 8 nm magnetite nanoparticle (MNP0, **Fig. 20**) coated with oleate surfactants were obtained by solvothermal decomposition in organic solvents as described by Park *et al.* MNP were then suspended in chloroform and transferred to water phase by mixing with a 0.5 M solution of an amphipilic polymer (PMA) in sodium borate buffer (SBB, pH 12). PMA was obtained by condensation of poly(isobutylene-alt-maleic anhydride), previously reacted with fluoresceinamine, and dodecylamine.[142] The resulting PMA-coated nanoparticles (MFN1) were fluorescent and superparamagnetic and were highly dispersed in aqueous environment. In order to optimize the accommodation of bulky proteins and to reduce possible nonspecific adsorption of other biomolecules to MFN, a PEG spacer (5 kDa) was linked to the guanine functionality. The pegylated surface ligand L0, containing an NH_2-ended O_6-PEG-guanine, was synthesized in 3 steps according to the procedure described in the methods section. L0 was bound directly to the residual carboxylic groups of the polymer coating *via* EDC activation (MFN2, **Scheme 3**). Previous evidence suggests that nanoparticle saturation occurs after conjugation of a discrete number of PEG ligands. MFN2 were characterized by DLS, exhibiting a mean hydrodynamic size of 145 ± 2 nm in PBS (pH 7.4, 5 μg mL^{-1}) and a maximal fluorescence emission at 515 nm. MFN2 were stable in PBS buffer resulting in a dark clean solution.

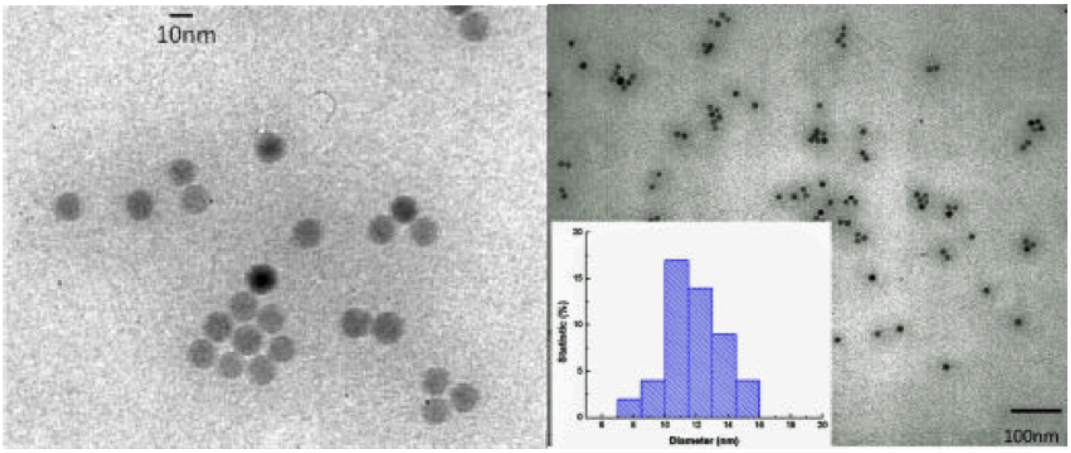

Fig. 20 TEM image of MNP0 (inset: size distribution of the nanoparticles).

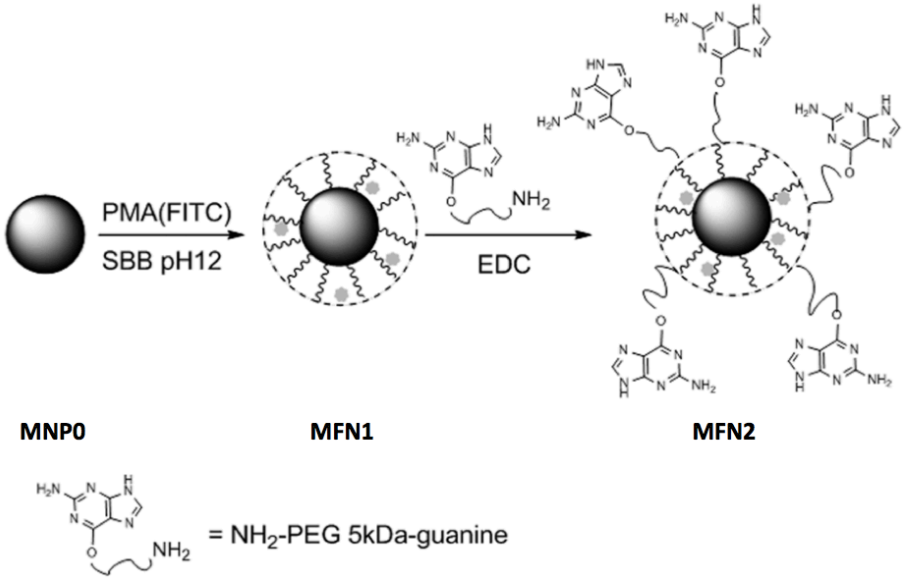

Scheme 3 Synthesis of MFN2.

2.1.3 MFN2 SNAP-scFv conjugation: SSMFN

The conjugation of the fusion protein to L0 on nanoparticles was achieved by reacting purified scFv-SNAP (0.5 mg) with MFN2 (1 mg) in PBS, pH 7.4, in the presence of 1 mM dithiothreitol (DTT). After overnight incubation at 4 °C, unconjugated scFv-SNAP was removed by centrifuging the mixture in amicon YM-100 tubes and the concentrated particles were washed three times with PBS, resulting in scFv-SNAP-functionalized MFN (SSMFN). DLS showed an increment in the hydrodynamic size (178 ± 7 nm) upon

conjugation.

2.1.4 SSMFN targeting capability

HER2-positive MCF7 cancer cells were used as cellular model to assess the targeting efficiency of SSMFN. Two sets of SSMFN were incubated for 1 h with MCF7 cells at two different concentrations (20 μg mL^{-1} and 100 μg mL^{-1}, respectively) and with HER2-negative MDA MB 468 cancer cells (100 μg mL^{-1}, negative control). Flow cytometry performed on HER2-positive MCF7 treated with SSMFN evidenced a concentration-dependent signal right-shift associated with labeled cells. In contrast, MDA MB 468 cells remained unlabeled after SSMFN treatment at the highest concentration (**Fig. 21**). The extent of labeling was larger with the 100 μg mL^{-1} SSMFN sample. However, all MCF7 cells detected were at least partially labeled. Submitted to even at 20 μg mL^{-1}. Indeed, no populations corresponding to unlabeled cells were recovered at both concentrations tested. These results suggest that SSMFN were recruited selectively by HER2-expressing MCF7 cells and that SSMFN-HER2 recognition was dose-dependent.

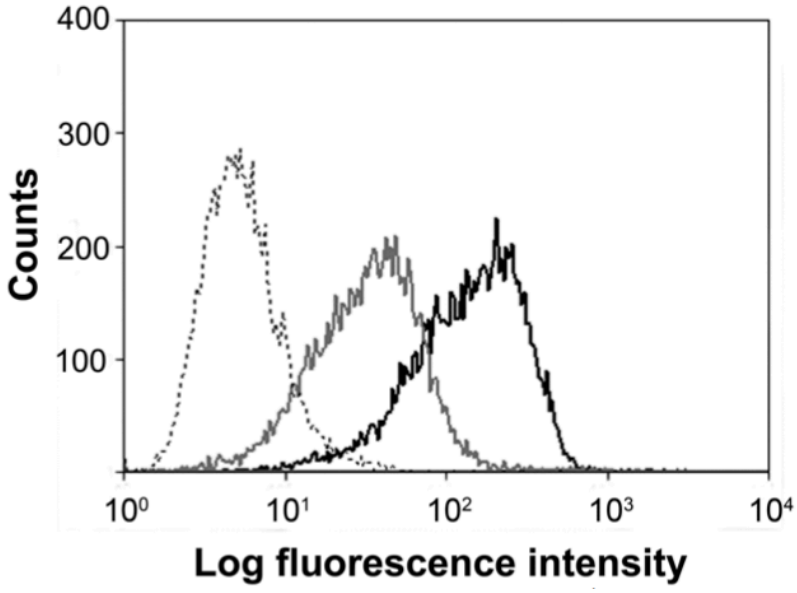

Fig. 21 MCF7 cells were incubated 1 h at 37 °C with 20 μg mL^{-1} (dark gray line) and 100 μg mL^{-1} (black line) of SSMFN. As a negative controls, MDA MB 468 cells treated with 100 μg mL^{-1} of SSMFN (light gray line) and untreated MCF7 cells (dashed line) were reported.

Next, confocal laser scanning microscopy confirmed the specificity of binding between SSMFN and HER2 receptors. MCF7 and MDA MB 468 cells were treated in parallel with 100 µg mL^{-1} SSMFN. Cells were also incubated 1 h with 20 µg mL^{-1} as a positive control and revealed with a dye-labeled secondary antibody to whole murine IgG. As HER2 is a transmembrane receptor, SSMFN and scFv-SNAP localized at the cell membrane of HER2-positive cells only, which confirmed that SSMFN adhesion to cell membrane was actually mediated by specific interaction with HER2 (**Fig. 22**).

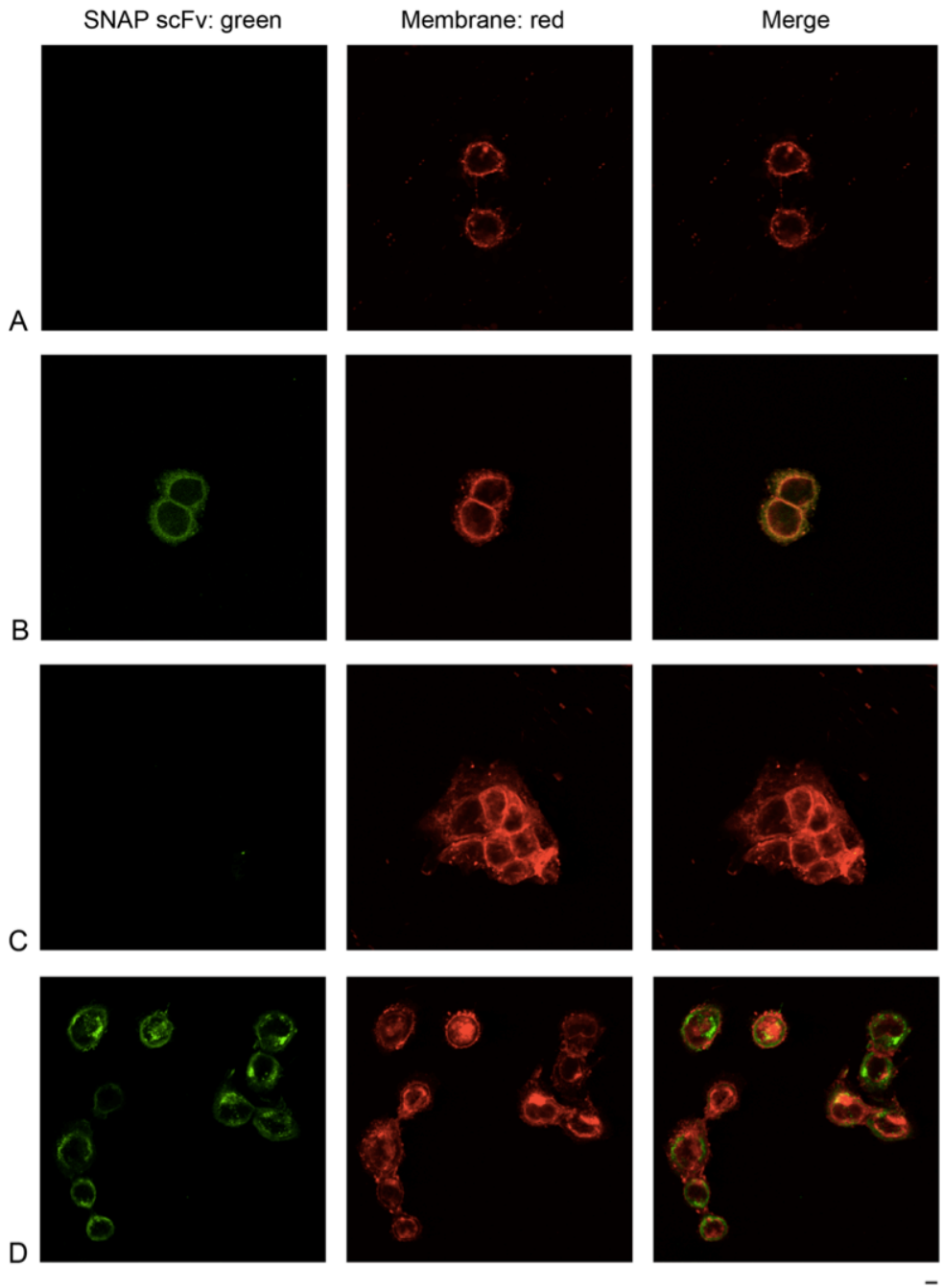

Fig. 22 $HER2^{+}$ cells (MCF7, D) and $HER2^{-}$ cells (MDA MB 468, C) were incubated 1 h at 37 °C with SSMFN (100 µg mL^{-1}). SNAP-scFv incubation with MCF7 and MDA MB 468 cells was used as positive (B) and negative controls (A), respectively. SNAP-scFv was revealed by fluorescein isothiocyanate (FITC)-conjugated secondary antibody against whole murine IgG (green). Membranes were stained with DiD oil (red). Scale bar = 10 µm.

2.1.5 SSMFN cytotoxicity

The MTT assay was performed to check SSMFN toxicity towards cell. Cells were incubated with SSMFN at 20, 50 and 100 μg mL^{-1}, showing that SSMFN were non-toxic in this range of concentrations, which is relevant to *in vitro* and *in vivo* applications (**Fig. 23 A**). MTT (3-(4,5-dimethylthiazol-2-yl)-2,5-diphenyltetrazolium bromide) assay showed a pattern similar to that of untreated cells both at 20 and 100 μg mL^{-1} (**Fig. 23 B**). On the whole, these experiments suggested that SSMFN were safe in cell cultures.

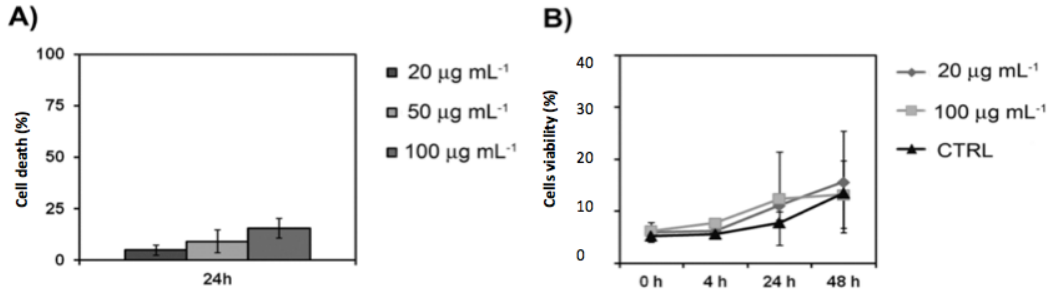

Fig. 23 A) Cell death assay with SSMFN. MCF7 cells were treated with SSMFN (20 μg mL^{-1}, 50 μg mL^{-1} and 100 μg mL^{-1}) for 24 h. Cell death was assessed by measuring the exposure of Annexin V and the incorporation of 7-aminoactinomycin D evaluated by flow cytometry. The percentage of cell death in untreated population was subtracted. The results are expressed as means ± S.D. of the mean of 3 individual experiments. B) Cell proliferation assay with SSMFN. MCF7 cells were treated with SSMFN (20 μg mL^{-1} and 100 μg mL^{-1}) for up to 48 h. Cell proliferation was tested by measuring the conversion of MTT into formazan. CTRL represents untreated control. The results are expressed as means ± S.D. of the mean of 5 individual experiments.

2.2 Orientation-controlled conjugation of Haloalkane dehalogenase fused homing peptides to multifunctional nanoparticles for the specific recognition of cancer cells

Haloalkane dehalogenase (HALO) from *Rhodococcus rhodochrous* forms an ester bond between aspartate 106 in the enzyme and the substrate, concomitantly removing halides from aliphatic hydrocarbons. Substitution of catalytic His272 with a phenylalanine prevents the substrate release, which usually occurs in native HALO, and thus stable bond can be formed between HALO and an alkyl conjugate.[172] Hence, we reasoned that a chloroalkane linker could be a good candidate to mediate the covalent, oriented

immobilization on MNP of homing peptides genetically fused with HALO.

We designed a bimodular genetic fusion (HALO–U11) comprising a small peptide of 11 amino acids (U11) that has a high affinity for urokinase plasminogen activator receptor (uPAR), which is overexpressed in several metastasizing tumors, as a targeting module, and HALO, as an MNP capture module. U11 is believed to be the primary uPAR binding motif with a dissociation constant of 1.3-1.4 μM.[125]

2.2.1 HALO and HALO-U11 protein production in Escherichia coli

The HALO sequence was modified by selective mutagenesis of the native protein. Moreover, *SalI* and *XhoI* restriction sites were inserted at the 5'- and 3'-positions, respectively, and the modified gene was cloned in a pGEX-6-P-1 vector to express HALO fused with glutathione S-transferase (GST). HALO was expressed in BL21(DE3) codon plus *E. coli* strain. After induction with isopropyl β-D-1-tiogalactopiranoside (IPTG), cells were collected and disrupted, HALO was isolated from the crude extract by using a glutathione–sepharose column and eluted by PreScission protease cleavage (1 mg L^{-1} yield).

HALO capture module was engineered by the introduction of a targeting element that consists of the 11 amino acid sequence VSNKYFSNIHW (U11) involved in uPAR recognition, throught a C-terminal insertion of a GGGGSGGGG loop, which provides sufficient freedom to U11. HALO-U11 fusion protein was produced in BL21(DE3) *E. coli* and purified by using the same procedure described above for HALO.

2.2.2 MNP synthesis

MNP2 were obtained as described above (section 1.2, materials and methods). The anchor ligand L1 containing a chlorohexane moiety, which is reactive toward the HALO binding site, was synthesized in three steps from simple precursors. L1 was linked to the amines on the polymer envelope through nucleophilic addition to the p-nitrophenyl carbonate group by incubation overnight at 4 °C (MNP3, **Scheme 4**). MNP3 were characterized by DLS, and exhibited a mean hydrodynamic size of 40.1 ± 2.7 nm in PBS (5 mg mL^{-1}, pH 7.4) with a ζ-potential of −28.5 ± 3.0 mV. MNP3 was very stable in PBS buffer and formed a dark transparent solution.

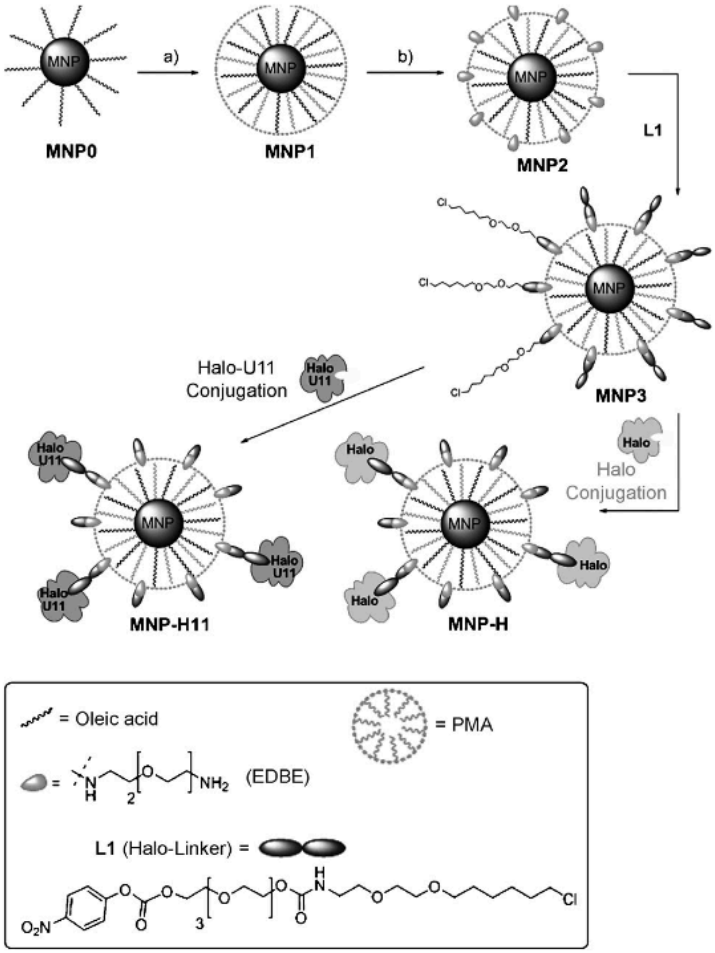

Scheme 4 Synthesis of HALO-functionalized multifunctional nanopar- ticles (MNP-H and MNP-H11). a) PMA, SBB, pH 12; b) EDBE, EDC, water. EDBE = 2,2-(ethylenedioxy)bisethylamine, EDC = N-(3-dimethyla-minopropyl)-N'-ethylcarbodiimide hydrochloride, PMA = amphiphilic polymer, SBB = sodium borate buffer.

2.2.3 HALO and HALO-U11 MNP3 conjugation

The optimal conditions for the conjugation of the fusion protein with L1 on MNP was deter- mined by varying several experimental parameters, including the protein/nanoparticle ratio, time, temperature, and incubation buffer (**Table 4**). The best HALO-functionalized MNP (MNP-H) conjugation conditions were obtained by treating purified fluoresceine isothiocyanate (FITC) labeled HALO with MNP3 in a 1:1 ratio (w/w) in PBS, pH 7.4. After 1 h incubation at 25 °C, unconjugated HALO was removed by centrifuging the mixture in amicon YM-100 tubes and the concentrated nanoparticles

were further reacted with α-methoxy-ω-amino- PEG (2 kDa, $mPEG_{2k}$-NH_2), after activation of the carboxylate groups of the polymer by EDC, to minimize possible nonspecific adsorption.

Table 4 Summary of conditions assayed for HALO-MNP3 conjugation.

Sample	HALO:MNP3 ratio	Buffer	Time (h)	Temperature (°C)	% conjugated protein
1	1:1	PBS	1	25	23.29
2	1:2	PBS	1	25	14.10
3	2:1	PBS	1	25	13.27
4	1:1	PBS	16	4	5
5	1:5	PBS	16	4	5
6	1:1	BB	1	25	11.6

*BB : binding buffer (100 mM Tris, pH 7.6, 150 mm NaCl, 0.05% IGEPAL CA-630).

The nanoparticles were then washed three times with PBS. The amount of filtered off, unreacted dye-labeled HALO was fluorometrically measured after first establishing a standard calibration curve, which provided the number of HALO molecules attached to each nanoparticle. We determined the presence of an average of about 5 HALO molecules per MNP-H. DLS analysis showed an increment in the hydrodynamic size upon conjugation (62.9 ± 7.2 nm), consistent with the attachment of protein molecules, and the nanoparticles were stable owing to a negative zeta potential of −32.3 ± 0.4mV. To assess whether the conjugation occurred specifically to L1, HALO was incubated with MNP2, as a control. No binding, within the fluorescence assay sensitivity, occurred to nanoparticles in the absence of L1, thus demonstrating that HALO immobilization on the nanoparticles was indeed mediated by ligand interaction with the active site of the enzyme.

After preliminary assessment of the efficiency of the HALO conjugation, a HALO-U11 capture module was engineered. HALO-U11 was reacted with FITC-labeled MNP3 by using the conjugation protocol illustrated in **Scheme 4**, to give MNP-H11 with a hydrodinamic size distribution of 67.6 ± 3.1 nm and a ζ-potential value of −27.8 ± 2.6 mV. In this case, the fluorescent label was covalently incorporated inside the polymer layer to avoid contact of the dye with the external environment, which could affect the

nanoparticle affinity for cellular receptors.

2.2.4 MNP-H11 targeting capability

U937 cell lines were selected as the cellular model to assess the targeting efficiency of MNP-H11, because these cancer cells are available as both uPAR-positive (U937_13) and uPAR-negative (U937_10). The only difference between them was the membrane expression of a U11-specific receptor, uPAR. U937_13 cell lines were first treated in parallel with dye-labeled MNP2 and HALO to evaluate nonspecific interactions of the pegylated nanoparticles and of the capture protein, respectively, with $uPAR^+$ cells. In both cases, no evidence of cell labeling was detected by flow cytometry (**Fig. 24**).

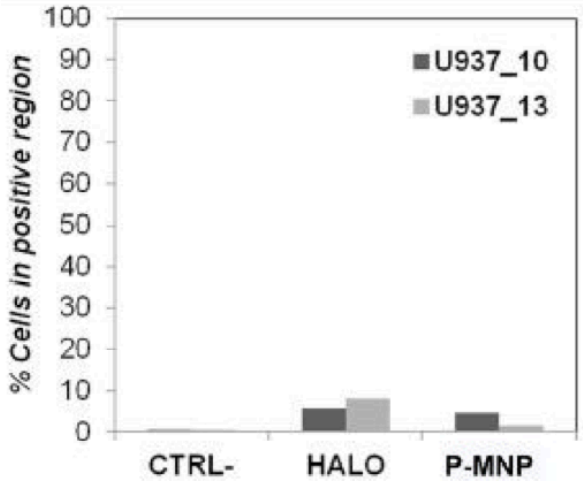

Fig. 24 Pegylated MNP1 and HALO were tested to evaluate binding to uPAR. U937 $uPAR^+$ and $uPAR^-$ cells were incubated 1 h at 37 °C with pegylated MNP1 (P-MNP, 20 μg mL^{-1}) and with HALO (40 ng mL^{-1}) and then processed for flow cytometry. Untreated cells were used to set the positive region.

To assess the influence of the controlled orientation of ligand presented HALO–U11, MNP were also directly conjugated with U11 peptide (4–6 molecules per MNP) by introducing a Cys residue at the C-terminal (MNP-U11). MNP-H11 and MNP-U11 were each incubated for 1 h with U937_13 and with U937_10 (control) cancer cells at two different concentrations (20 mg mL^{-1} and 100 mg mL^{-1}). Flow cytometry performed on the U937_13 cells treated with MNP-H11 evidenced a twentyfold increase in the percentage of cells in the positive region compared to MNP-U11 treated cells (**Fig. 25**). Quite surprisingly, MNP-U11 were not able to bind $uPAR^+$ cells any more than to $uPAR^-$,

probably owing to a low availability of the short peptides for recognition. U937_10 cells remained mostly unlabeled after MNP-H11 treatment, even at 100 mg mL^{-1}. These results demonstrate that the controlled peptide orientation is crucial for optimal target specific recognition, as MNP-H11 were captured selectively by uPAR-expressing U937_13 cells.

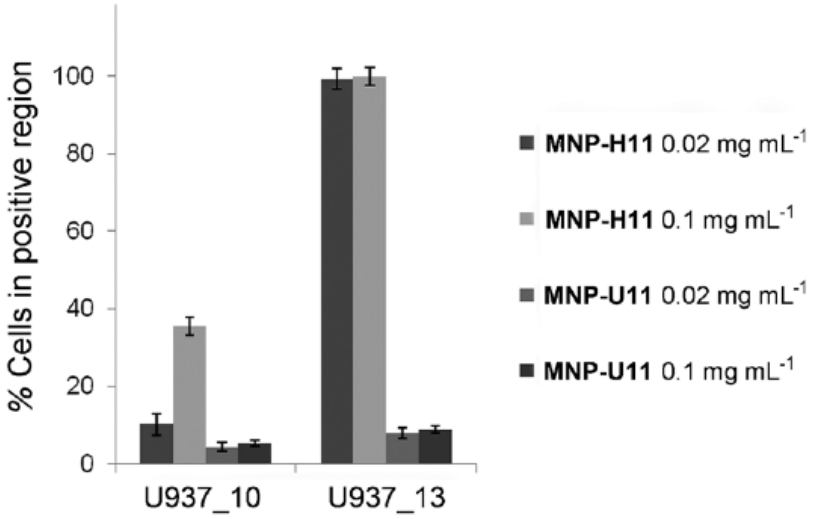

Fig. 25 MNP-H11 and MNP-U11 binding specificity to uPAR. U937 $uPAR^+$ (U937_13) and $uPAR^-$ (U937_10) cells were incubated at 37 °C with MNP-H11 and MNP-U11 at two different concentrations (0.02 mg mL^{-1} and 0.1 mg mL^{-1}) for 1 h and then processed for flow cytometry. Untreated cells were used to set the positive region. Data are expressed as means ± standard error (SE) of three individual experiments.

The specificity of the binding between MNP-H11 and uPAR was confirmed by confocal laser scanning microscopy. U937_13 and U937_10 cells (CTRL-) were treated in parallel with MNP-H11 (100 mg mL^{-1}) for 1 h at 37 °C. As a uPAR expression control, U937_13 cells were immunodecorated with anti-uPAR antibody (CTRL+). MNP-H11 were localized in the proximity of the cell membrane and inside the cytoplasm of $uPAR^+$ cells only, showing a uPAR recognition pattern similar to the positive control; this finding confirms that MNP-H11 adhesion to the cell membrane and internalization were actually mediated by specific interactions with the U11 peptide (**Fig. 26**).

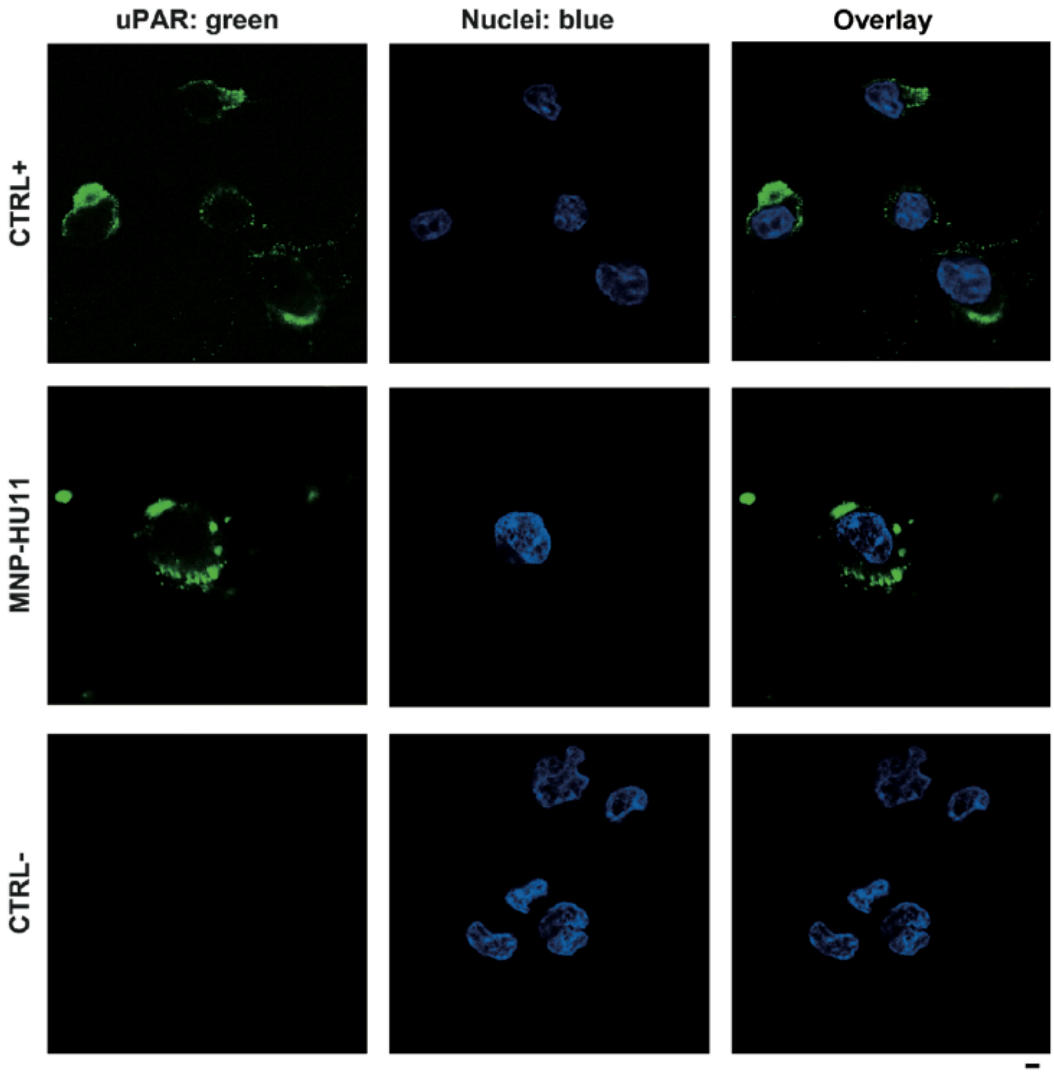

Fig. 26 Confocal microscopy images of U937 uPAR^{+} and uPAR^{-} (CTRL−) cells, incubated for 1 h at 37 °C with MNP-H11 (0.1 μg mL^{-1}, green). As a positive uPAR-expression control (CTRL+), U937 uPAR^{+} cells were immunodecorated with anti-uPAR primary antibody, revealed with an anti-mouse secondary antibody conjugated with Alexa fluor 488 (Invitrogen). Nuclei were stained with 4',6-diamidino-2-phenylindole (DAPI). Scale bar = 10 μm.

2.2.5 MNP-H11 cytotoxicity

Cell-death experiments performed on U937_13 cells after 24 h incubation with MNP- H11 at 20 mg mL^{-1} and 100 mg mL^{-1}, suggested that MNP-H11 were nontoxic within this range of concentrations; this finding is relevant to in vitro and in vivo applications (**Fig.**

27).

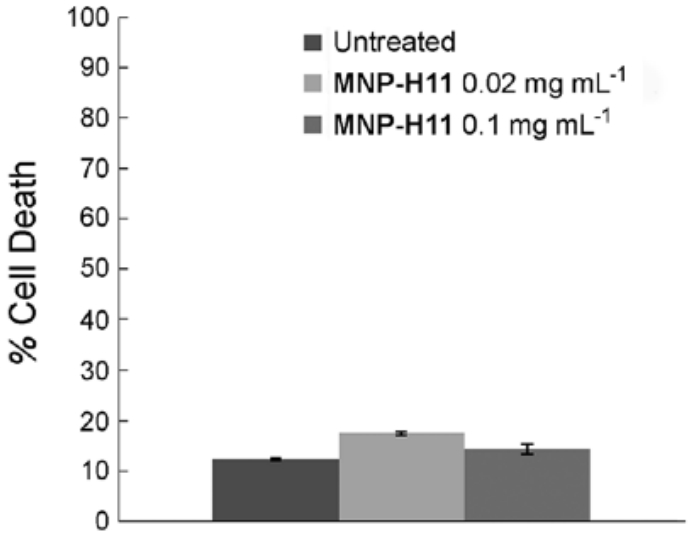

Fig 27 Cell-death assay. U937 uPAR^{+} cells were treated with MNP-H11 (0.02 mg mL^{-1} and 0.1 mg mL^{-1}) for 24 h (light and dark grey, respectively). Cell death was assessed by measuring the exposure of Annexin V and the incorporation of 7-aminoactinomycin D and evaluated by flow cytometry. An untreated sample is show as negative control. All results are expressed as means ± SE of five individual experiments.

2.3 Covalent-oriented immobilization via enzymatically fusion protein Cutinase-U11, for targeting cancer cells

Cutinase (CUT) from *Fusarium solani pisi* is a 22 kDa serine esterase that forms a site specific covalent adduct with phosphonate esters ligands. The phosphonate-ester, which mimic the tetrahedral transition state of an ester hydrolysis, is attacked by the catalytic serine (Ser 120) residue, resulting in displacement of the leaving group and formation of a stable covalent adduct that is resistant to hydrolysis.[171] Moreover, the enzyme is small, globular and monomeric, all features that minimize the steric effect of peptides eventually fused with it. In this work, we reasoned that an alkylphosphonate para-nitrophenol ester linker could be a good candidate to mediate the covalent, oriented immobilization between the MNP and the homing peptide genetically fused with CUT.

We designed a modular genetic fusion (CUT-U11) comprising the small peptide U11.[173] In this way, MNP covalently bound with CUT-U11, may be potentially used as modular delivery platform with nano size for active target or imaging probe.

2.3.1 CUT and CUT-U11 protein production in Escherichia coli

CUT DNA sequence was cloned in a pET-11a vector, to obtain a protein fused with His-tag, between *NdeI* and *BamHI* restriction sites. The modified gene was used to transform BL21(DE3)-RIL *E. coli* strain, in which CUT was expressed. After induction with IPTG, cells were collected and disrupted, and CUT purified using a Ni-NTA agarose column in 1.6 mg L^{-1} yield.

DNA sequence encoding CUT-U11 was modified to obtain sequence containing *NdeI* and *BglIII* restriction sites, respectively, at 5' and 3' positions. CUT-U11 DNA sequence was cloned in a pET-30b vector. CUT-U11 was expressed in *E. coli* expression strain Tuner(DE3) and purified as CUT onto a Ni-NTA agarose column in 1 mg mL^{-1} yield. As for HALO-U11, a spacer made of GGGGSGGGG was inserted between cutinase and U11.

2.3.2 MNP synthesis

MNP2 were obtained as described previously (see chapter materials and methods, section 1.2). The Alkyl phosphonate L2 was linked to the amines on the polymer envelop through nucleophilic addition to the carbonyl diimidazole group by incubation overnight at 4 °C (MNP3). Even if these particles were not PEGylated, they had a high solubility and presented a lower trend to aggregation. In alternative, PMA was first treated with FITC, before reaction with MNP1, with the aim to obtain a fluorescent coating (MFP1). The resulting MNP1 or MFP1 exhibited optimal stability and monodispersion properties. The nanoparticles were characterized by DLS and ζ−Potential and presented the values of 21.1 nm and −65.32 ± 0.06 mV respectively.

2.3.3 CUT-U11 MNP3 conjugation

The bioconjugation reaction was carried out in a 1 : 2 (w/w) ratio between MNP3 and CUT-U11 (**Scheme 5**).

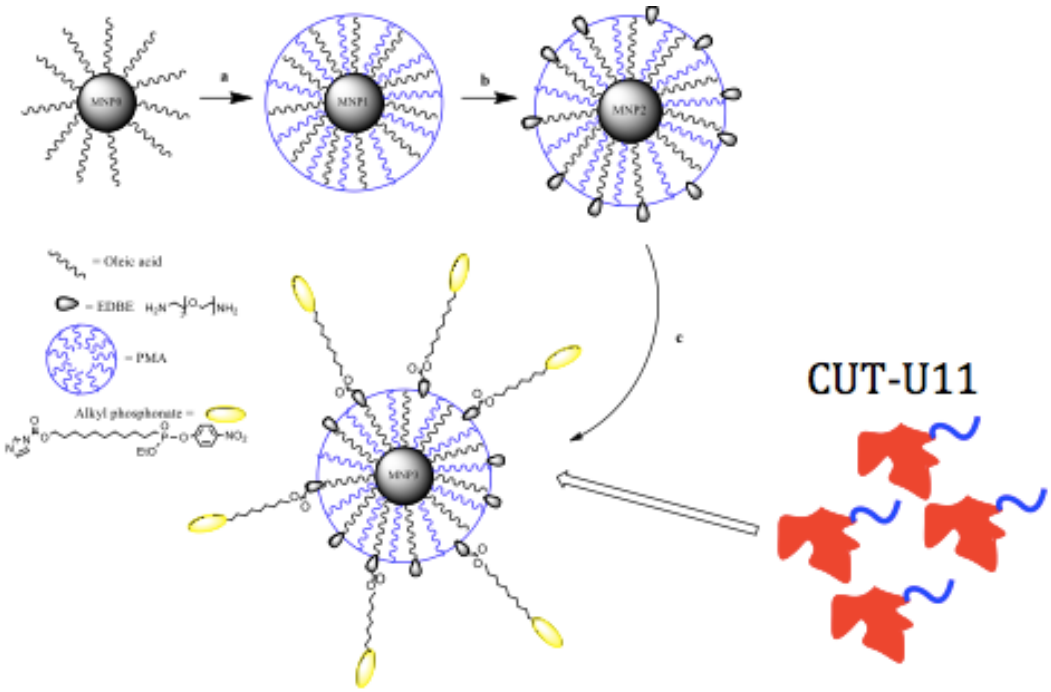

Scheme 5 Synthesis of CUT-U11 functionalized multifunctional nanoparticles. a) PMA, SBB, pH 12; b) EDBE, EDC, water. EDBE = 2,2-(ethylenedioxy)bisethylamine, EDC = *N*-(3-dimethylaminopropyl)-*N'*-ethylcarbodiimibe hydrochloride, PMA = amphiphilic polymer, SBB = sodium borate buffer.

Three different amounts of protein and nanoparticles were tested, maintaining always the same ratio 1:2. Hence, 25 : 50 (1), 50 : 100 (2), 125 : 250 (3) µgs of MNP3 and CUT-U11 respectively were reacted for 1 h at room temperature, under stirring at 140 rpm on the shaker. All the three reactions were made with CUT-U11-FITC, with the purpose to quantify spectrofluorimetrically the amounts of protein reacted on the nanoparticles. Therefore, a standard curve based of CUT-U11-FITC was set (**Fig. 28**).

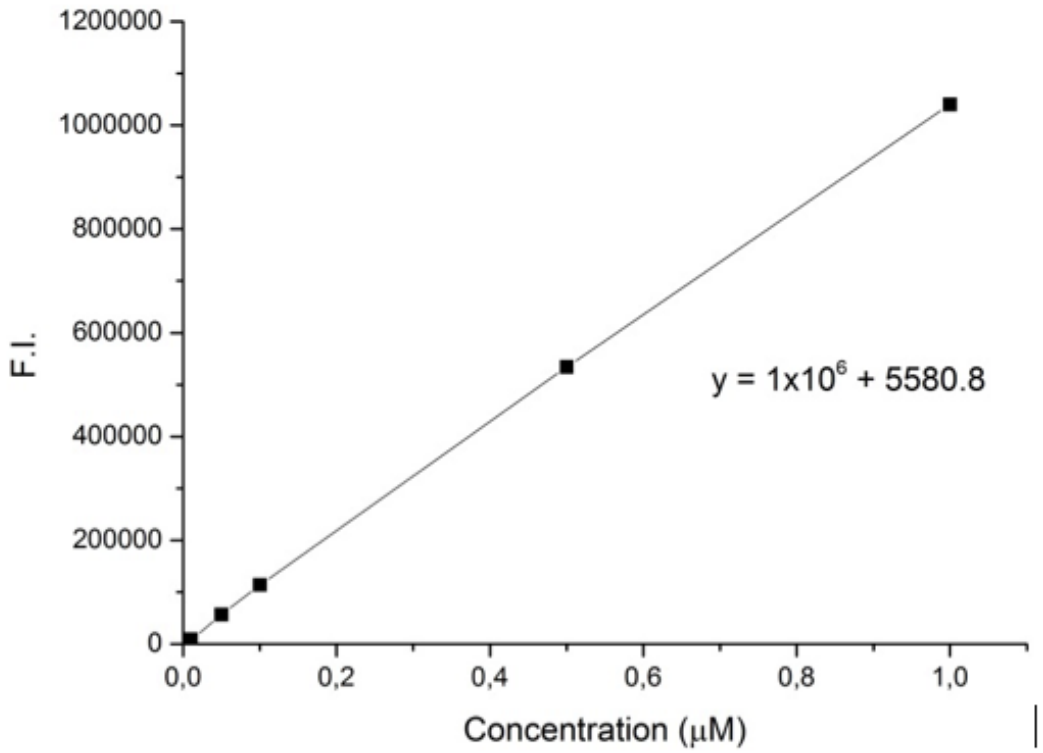

Fig. 28 Standard curve of concentration for CUT-U11-FITC.

After the incubation, the mixes were centrifuged, washed three times in PBS and resuspended in PBS. Then, the fluorescence of each mix was measured (**Fig. 29**). The amount of protein for each sample was determined by the standard curve based on CUT-U11. The highest fluorescence was measured for the third condition, so we decided to set all the subsequent experiments with the amount of MNP3 : CUT-U11 used for this reaction (125 : 250 μg).

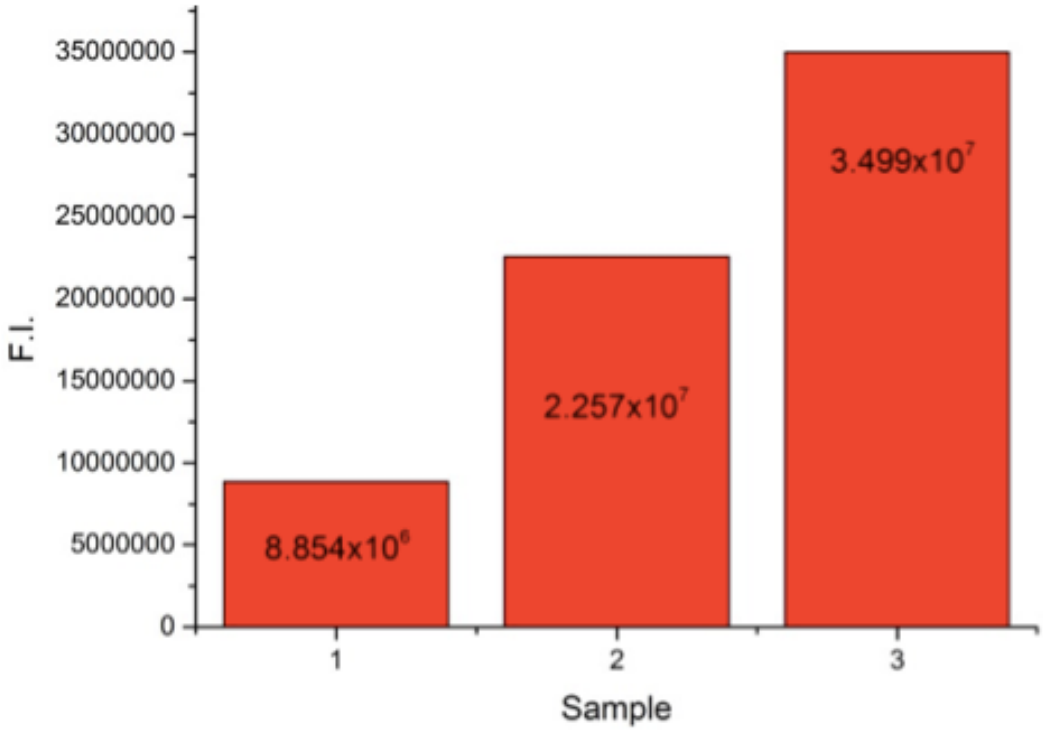

Fig. 29 Intensity of fluorescence of the different batches of MNP-CUT-U11-FITC.

To monitor the conjugation reaction, two distinct reactions were performed. MNP1 or MNP3 were incubated with CUT in a 1:2 ratio (w/w) nanoparticle/protein. After 5 min incubation, the CUT activities of the washed mixtures were tested. **Fig. 30** shows that phosphonate linked to MNP3 competed with 4-nirtophenyl decanoate for the active site of the enzyme. Indeed, CUT maintained its activity when incubated with MNP1, while in the case of MNP3 displayed from the beginning a much lower activity compared to MNP1, which further declined at later times, suggesting of irreversible inhibition.

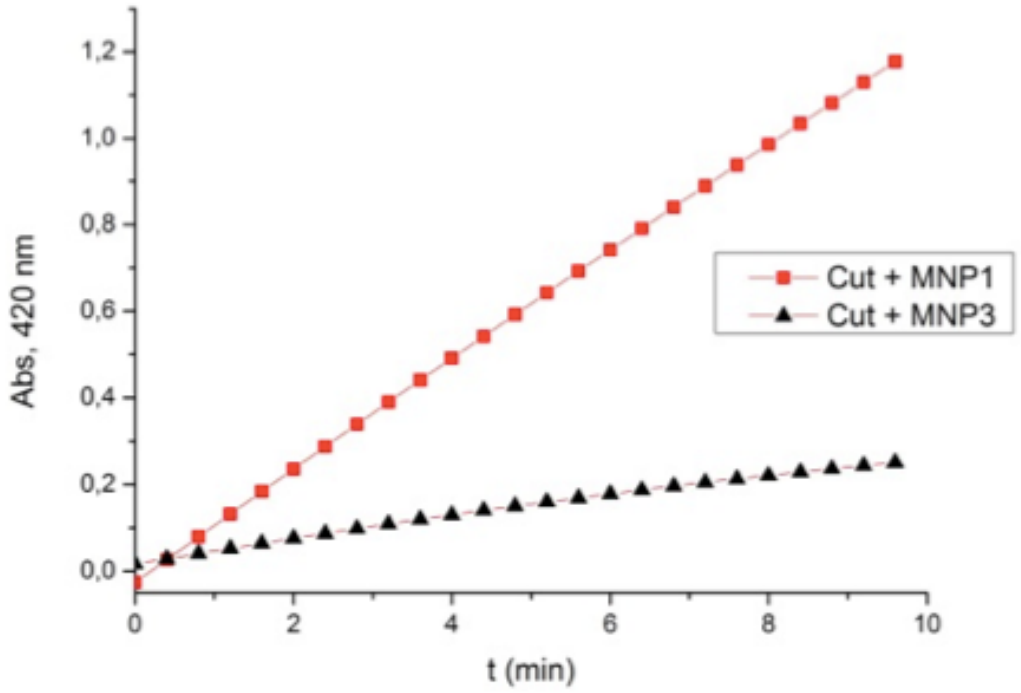

Fig. 30 Activity assay of CUT after reaction with MNP1 or MNP3.

To demonstrate that the conjugation between CUT-U11 and NPs is mediated by the alkyl-phosphonate, we set up two different experiments. In the first experiment we incubated CUT with its inhibitor 4-nitrophenyl-phosphonate in order to demonstrate that it could not bind nanoparticles if the protein had been already inhibited. In this way, 250 µg of CUT were incubated with 4-nitrophenyl-phosphonate (0.5 µM) for 15 min. Then, the enzyme was passed in a PD10 column to eliminate the excess of inhibitor. CUT-Inhibited (CUT-I) was incubated with MNP3 under the mentioned conditions. After the reaction was completed, the mixture was washed three times in PBS. The excluded volume and the washes were tested with Bradford. We observed that about 91% of CUT-I was conjugated to the NPs. This shows that CUT-I was aspecifically adsorbed to the NPs surface. The second experiment involved a bioconjugation reaction between CUT and MNP1, i.e., the NPs that do not expose the alkyl phosphonate linker. After the end of incubation, the resulting NPs were washed three times and excluded volume and washes were collected and assayed with Bradford. The amount of protein bound onto the NPs was 63%. Also in this case we found a large amount of protein aspecifically adsorbed.

Since aspecific adsorption was found, we did not prove the specificity of the reaction between CUT and phosphonate linker in this condition.

Different approaches were initially used for avoiding this aspecific adsorption of protein on MNPs. In the first attempt MNP-CUT-11 were incubated in PBS plus 0.5 mg mL^{-1} SDS for 30 min at RT.[171] This method was inefficient due to the disruption of nanoparticles, probably causing to the dissolution of PMA coating, as shown by the presence of a white precipitate at the bottom of the tube after centrifugation. So, under these conditions the protein quantification was not feasible.

The second strategy was accomplished by altering the ionic strength of reaction mix. Since magnetite superparamagnetic nanoparticles have a strong net negative charge, and the pI of CUT and CUT-U11 is 7.89 and 8.37 respectively, we reasoned that washing nanoparticles at basic pH (higher than pI), might eliminate aspecific protein adsorption. Also, this method was inefficient, and the amount of protein recovered in the excluded volumes and washes was comparable with data already obtained in the two experiments above described.

Finally, we decided to fully cap all possible aspecific binding site on nanoparticles surface using Bovine Serum Albumin (BSA). The idea was that BSA adsorption on nanoparticles surface could prevent aspecific interaction with CUT. In this way, CUT could bind nanoparticles only via alkyl phosphonate linker. For this set of experiments, we use CUT-U11-FITC, to easily quantify the amount of conjugated protein with a spectrofluorimeter. A large amount of BSA (PBS/BSA 0.3%) was incubated with MNP3 before adding the protein. A control mix was set using MNP1. The reaction mixes were washed twice in PBS centrifuging 30 min at 17000 rpm. The supernatant was discarded and mixes resuspended in PBS once again. Then, their fluorescence was measured. The fluorescence intensity was clearly higher for MNP3 ($3.66\ 10^7 \pm 1.08\ 10^7$) than for MNP1 ($2.5\ 10^6 \pm 1.15\ 10^6$) incubated with CUT-U11-FITC (**Fig. 31**). This is also appreciable to the naked eye. In fact, after centrifugation, a yellow pellet was suitable in the reaction mix conducted with MNP3 due to the presence of CUT-U11-FITC. In contrast, the pellet obtained after the reaction conducted with MNP1 was dark (**Fig. 31**). This experiment demonstrates the specificity of the reaction between enzyme and alkyl phosphonate linker. We could also quantify the presence of 4 CUT-U11-FITC molecules per MNP and 1 protein molecule aspecifically adsorbed. The amount of protein was quantified by comparison with a calibration curve constructed with the CUT-U11-FITC (**Fig. 32**).

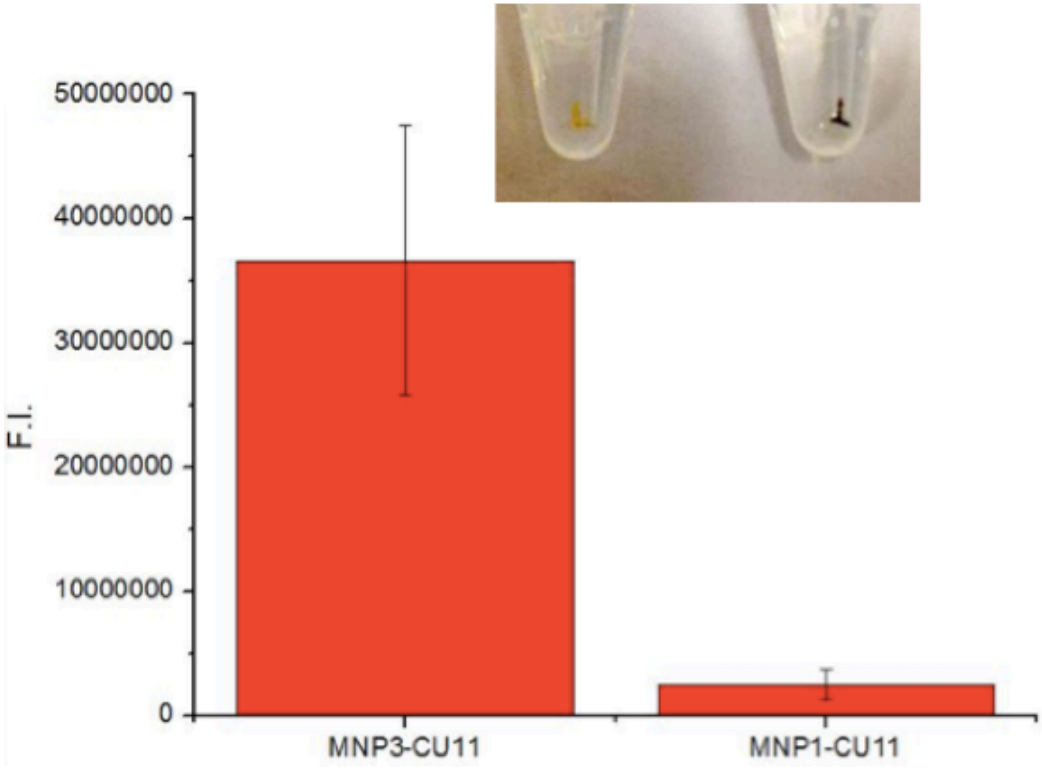

Fig. 31 Figure 4: Fluorescence intensities of MNP3-CUT-U11 and MNP1-CUT-U11. Inset: photo of

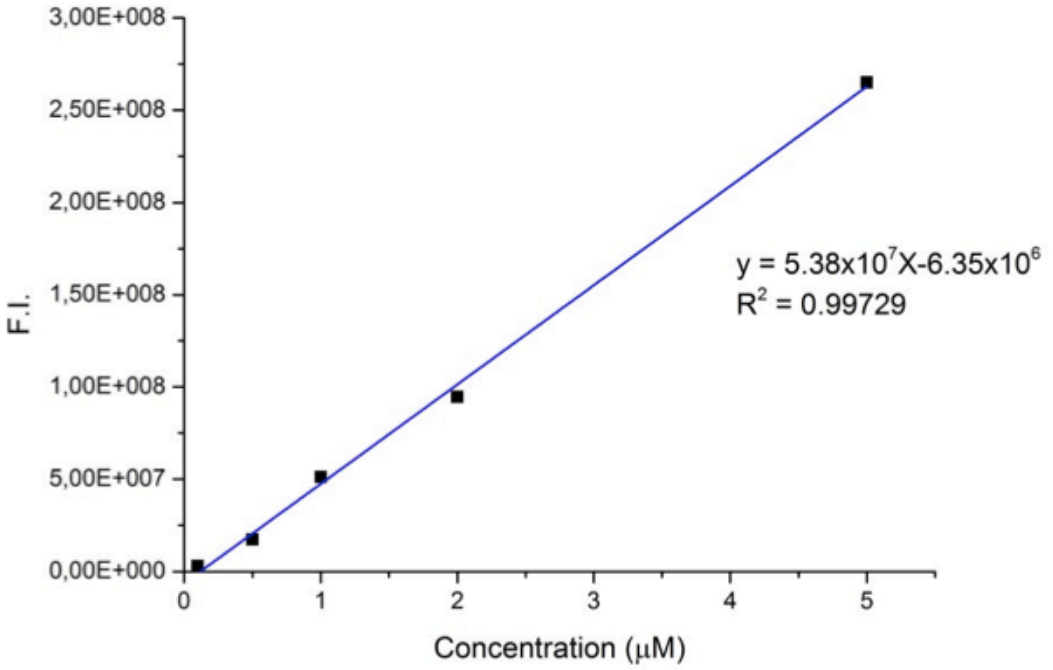

Fig. 32 Standard curve of concentration for CUT-U11-FITC.

Also, the characterization of the MNP-CUT-U11 by DLS and ζ−potential, confirmed the bioconjugation. The hydrodynamic diameter of MNP-CUT-U11 increased from 21.1 nm (for MNP3) to 53.4 nm due to protein binding. The different size recorded for MNP-CUT (46.41 nm) and MNP-CUT-U11 could be attributed to the presence of the U11 peptide that enhanced the solvation sphere of the nanoparticles. ζ−potential measures showed a substantial decrease in the surface MNPs charge, which turned from – 65.32 ± 0.06 mV of colloidal suspension MNP3, to – 38.51 ± 2.62 mV of MNP-CUT-U11, more pronounced than MNP-CUT (− 51.01 ± 1.75). Also this feature could be attributed to the presence of U11, which presents a positive net charge.

2.3.4 MNP-CUT-U11 targeting capability

Fluorescent superparamagnetic nanoparticles MFP-CUT and MFP-CUT-U11 were prepared to test U11 biological activity on $uPAR^+$ cells. MFP-CUT and MFP-CUT-U11 were incubated with MDA MB 468 cells at a concentration of 100 μg mL^{-1} of culture medium for 1 h at 37 °C. As expected, only MFP-CUT-U11 was observed in the proximity

of MDA MB 468 uPAR^{+} cell membrane and inside the cytoplasm (**Fig. 33**). These finding demonstrate that MFP-CUT-U11 targeting is mediate by specific U11/uPAR^{+} interaction.

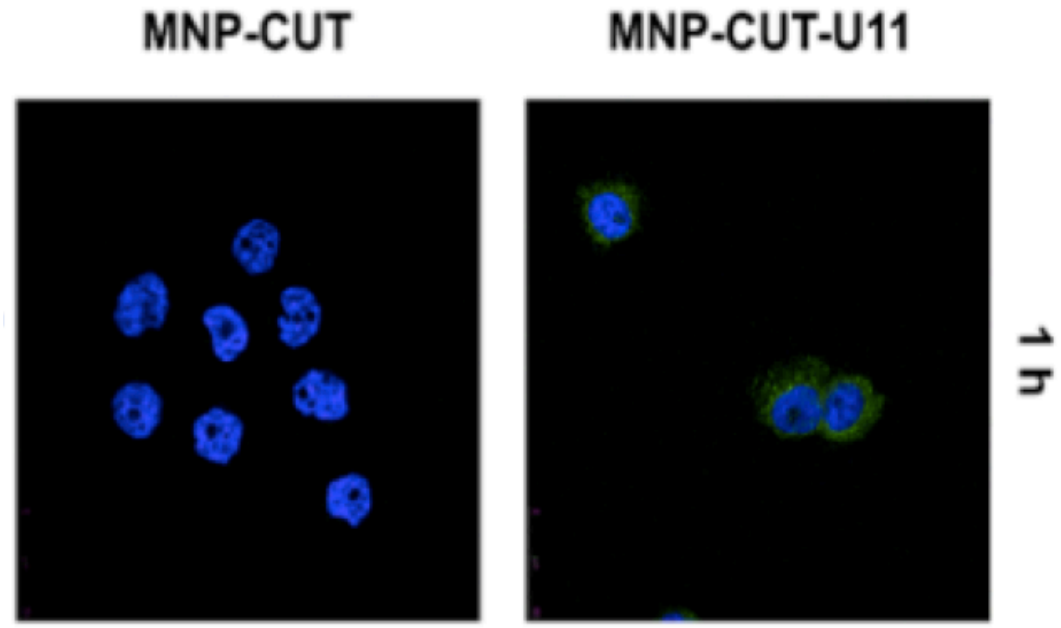

Fig. 33 Confocal microscopy images of MDA MB 468 cells, incubated for 1 h at 37 °C with MNP-CUT-U11 and MNP-CUT (100 μg mL^{-1}). Nuclei were stained with 4',6-diamidino-2-phenyl-indole (DAPI). Scale bar: 10 μm.

Moreover, 40 μg of both MNP-CUT and MNP-CUT-U11 samples were incubated 4 h with MDA MB 468 cells, for Transmission Electron Microscopy (TEM) analysis. Also in this case, only MNP-CUT-U11 was detected inside the cells (**Fig. 34**).

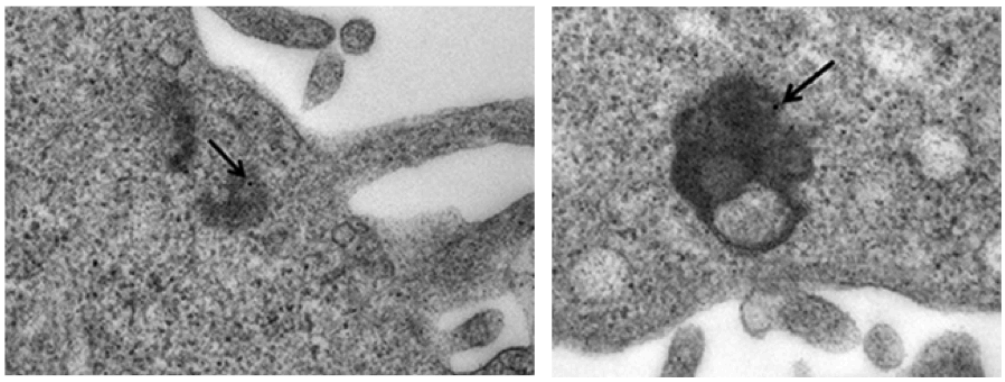

Fig. 34 TEM images of MDA MB 468 cells incubated for 4 h at 37 °C with MNP-CUT-U11 and MNP-CUT (40 μg mL^{-1}).

It is reported that the mechanism of complex uPA/uPAR internalization is clathrin mediated. For this reason we expected to see nanoparticles embedded in this structure. In spite of this, there is also evidence of different internalization mechanisms in. As apparent from TEM picures, nanoparticles were found inside endosomes. We do not exclude a specific interaction U11/uPAR, but probably the entire complex protein-nanoparticle could alter the normal way of receptor internalization. Additional studies are necessary to clarify this issue.

3. Gold nanoparticle functionalized with short peptides for targeting breast cancer cells

Targeted therapy with monoclonal antibodies is the main treatment currently employed in many cancers. However the use of short peptides as targeting moieties to tumor receptors has several potential advantages over commonly employed entire antibodies. In particular, they allow better organization and lower undesirable natural biological activity of peptides, along with their low nonspecific uptake by reticuloendothelial system such as the liver, spleen and bone marrow.[174] In addition, peptides are chemically stable and relatively easy to derivatize compared to monoclonal antibodies

Recently, so called “tumor homing peptides”, have attracted plenty of attention in the field of oncology, thanks to their high selectivity toward tumor cells.[175-177] Due to their good targeting capacity, peptide-mediated, selective drug delivery to tumor tissue may alleviate the problem of high drug toxicity and low biodistribution.

Among different nanoparticles, gold nanoparticles (AuNPs) have been proved to be a good tool for biomedical applications, due to their unique optical and chemical properties, along with straightforward preparation and surface functionalization *via* Au-thiol chemistry. In addition, functionalization of nanoparticles with bioactive targeting ligands allows to improve not only the selectivity of the conjugates exploiting a higher capacity to enter the cells, but also their antitumor activity over the free drug through an increase of its local concentration.

Due to gold nanoparticles properties and to peptides peculiarity, we studied the binding of AuNPs modified with *ad hoc* synthesized peptides with breast cancer cells.

Here, we have adopted AuNPs functionalization with U11 peptide for uPAR targeting, as well as peptides selected from a phage-displayed peptide library (TumorHoPe) specific for MCF7 breast cancer cells recognition.

3.1 Development of U11-functionalized gold nanoparticles for selective targeting of urokinase plasminogen activator receptor-positive breast cancer cells

Urokinase amino-terminal fragment (ATF) protein-derived peptide sequences have recently been used as an efficient way of targeting the urokinase plasminogen activator receptor (uPAR) on cancerous cells. Among uPAR targeting peptide sequences, U11 peptide (VSNKYFSNIHW) represents a part of urokinase plasminogen activator (uPA) ligand. Its looped structure comprises eleven amino acid residues localized at the tip of a β-hairpin loop within growth factor domain of uPA. The interaction between U11 and uPAR was found to be characterized by an equilibrium dissociation constant K_d of 1.3-1.4 μM.[173] Considering the binding affinity along with the receptor-mediated endocytosis properties of the uPAR-uPA complex, the uPAR-U11 receptor-ligand system could be attractive for the targeting of nanoparticles. So we developed an *ad hoc* nanoconjugate where U11 peptide is inserted into a mixed monolayer of ligands imparting the stability and fluorescent properties to AuNPs.

3.1.1 AuNPs synthesis

Citrate-stabilized AuNPs were prepared by a modified Turkevich-Frens method yielding monodisperse spherical nanoparticles of 16 ± 1.2 nm.[178,179] The method involves the reaction of boiling chloroauric acid solution with small amounts of warm sodium citrate solution. Citrate ions act as both a reducing agent and a capping agent leading to the formation of nanoparticles.

3.1.2 AuNPs bioconjugaiton

For covalent conjugation to AuNPs exploiting Au-thiol chemistry, a cysteine was added to the C-terminus of the peptide. A scrambled peptide retaining the U11 amino acid residue composition, was used as a control (ISKSVYNFWNH). AuNPs were stabilized and functionalized by a mixed layer of ligands to give fluorescent U11-

derivatised nanoconjugates.[183,184] For this purpose, the components were mixed at specific stoichiometric ratios to achieve precise control over the number of functional ligands on each particle, maintaining reproducibility in nanoparticle production. For nanoparticle derivatization we used U11 peptide along with a short PEG (11-mercaptoundecyl-tetra (ethylene glycol), (1)) containing both –SH and –OH groups, and a dithiol molecule terminated with –COOH and FITC groups (2). In **Fig. 35** it is schematically presented a TEM micrograph showing a typical multifunctional particle of this type, along with the chemical structure of the ligands utilized for the synthesis. Although conjugation of peptides to the protecting ligand shell of AuNPs is an appealing strategy to preserve their biological activity.[181,182]

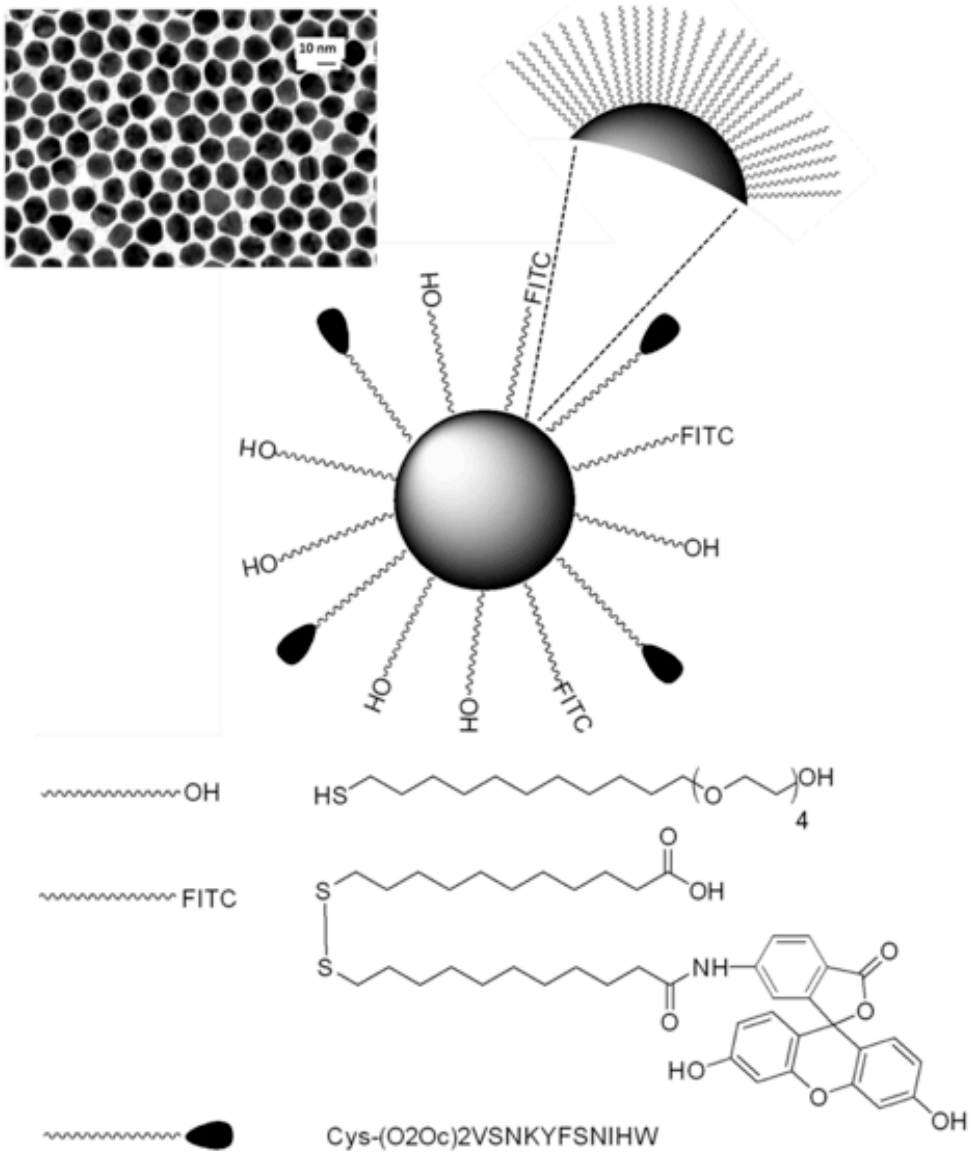

Fig. 35 Schematic representation of mercaptoethylene glycol-stabilized and U11 peptide-functionalized gold nanoparticles, along with the structure and amino acid sequences of the lignads and an example of TEM micrograph of AuNPs.

It has been shown elsewhere that ligand shell composition and ligand density on nanoparticle surface play an important role in particle internalization mechanism and efficiency.[183,184] Our preliminary experiments have shown that 3% of FITC groups is the most suitable amount to render the NPs bright enough for cell binding studies aimed at

avoiding false positive results (data not shown). On the other hand, variation of U11 amount from 1% to 20 % demonstrated destabilization of nanoparticles and irreproducible results (data not shown), especially at high peptide contentrations. In view of these considerations, we adjusted the initial amounts of U11 peptide and FITC to 3% each.

Although AuNPs are known to quench the fluorescence due to energy transfer, our nanoconjugates remain highly fluorescent with intensity around 10^9 CPS being sufficiently bright for potential biological applications. However, the fluorescence intensity of the NPs was observed to decrease after a few weeks, probably, due to detachment of thiolated FITC molecules. Thus, only freshly-prepared AuNPs were used for all biological experiments to avoid false negative results.

The physicochemical properties of peptide-functionalized nanoparticles have been studied by UV-vis, TEM, DLS and ζ-potential techniques and the results are reported in **Table 5**. The nanoparticles showed negative charge and small hydrodynamic diameter confirming good colloidal stability and monodispersity at 1 mM NaCl at pH 7.

Table 5 Au-U11 NPs characterization by UV-vis spectroscopy, transmission electron microscopy (TEM), dynamic light scattering (DLS) and ζ-potential.

Parameter	Unit	Au-U11
Local Surface Plasmon Resonance (LSPR)	nm	524
Particle size (TEM)	nm	16 ± 1.2
Hydrodynamic diameter (DLS)	nm	21.3 ± 1.5
Z-potential	mV	− 30 ± 1.02

3.1.3 AuU11 biological activity

To assay NP biological activity we used both uPAR-positive human MDA MB 468 cells, uPAR-positive murine 4T-1 cells and uPAR-negative human CAL51 breast cancer cells.

The binding efficiency between uPAR and Au-U11 NPs was studied by fluorescence-based flow cytometry (FACS) as a function of nanoparticle concentration. Generally, cell-associated FITC fluorescence was examined two hours post-incubation of

Au-U11 NPs with the cells. In order to minimize receptor-mediated endocytosis, we performed the incubation at 4°C. Flow cytometry results, reported on **Fig. 36**, show that uPAR-positive cells treated with Au-U11 NPs evidence a twofold increase in the percentage of cells in the positive region compared to uPAR− treated cells (CAL51) at 0.5 nM concentration of NPs. At higher, 2 nM and 4 nM, nanoparticle concentration, the percentage of cells in the positive region grows up to reach 53 %, indicating the binding in a concentration-dependent manner (**Fig. 36**). The nanoparticles functionalized with scrambled U11 peptide showed negligible binding to all kinds of tested cells, confirming the specificity of the nanoparticles for uPAR.

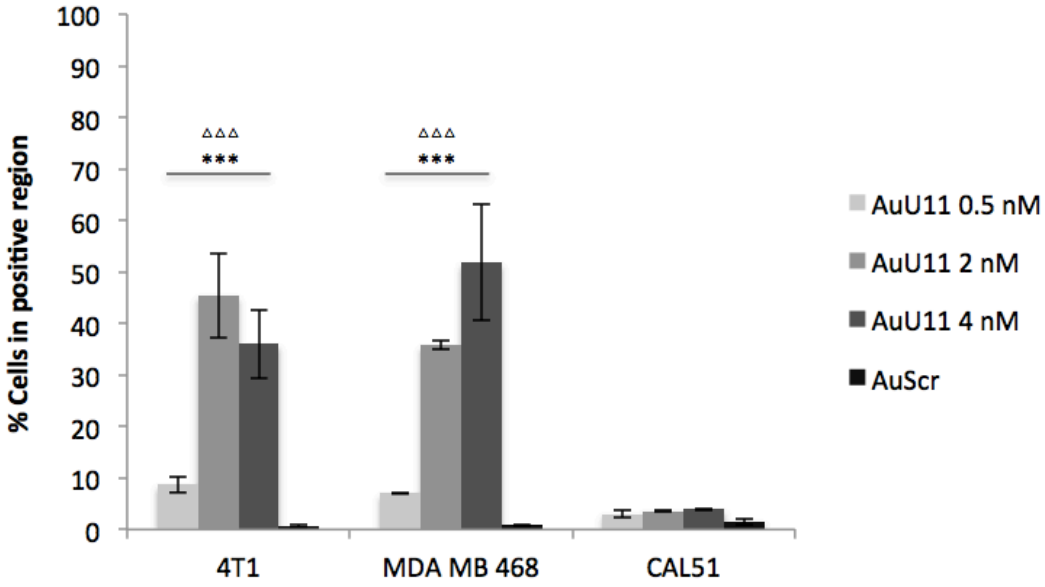

Fig. 36 FACS analysis of uPAR targeting with Au-U11 NPs on MDA MB468 ($uPAR^+$), 4T1 ($uPAR^+$) and CAL-51 ($uPAR^-$) cells. The cells were incubated for 2 h at 4°C with 0.5, 2, and 4 nM particle concentration. The results are expressed as means ± S.D. of 3 individual experiments normalized on cell proliferation of untreated cells. T-student analysis are calculated compare to untreated control.

While flow cytometry is a powerful tool to quantify association of nanoparticles with cells, it does not distinguish between cellular binding and cellular internalization. To confirm cellular uptake and internalization of the nanoparticles by the breast cancer cells we performed confocal laser scanning microscopy experiments. Scrambled peptide conjugated nanoparticles and cell-only controls were also included. The data do indicate

the active involvement of receptor-mediated targeting and U11 ligand specificity to uPAR-positive MDA MB 468 cells as localization of Au-U11 NPs can be observed inside the cell. Negligible internalization was evident with nontargeted scramble-peptide functionalized nanoparticles (**Fig. 37**).

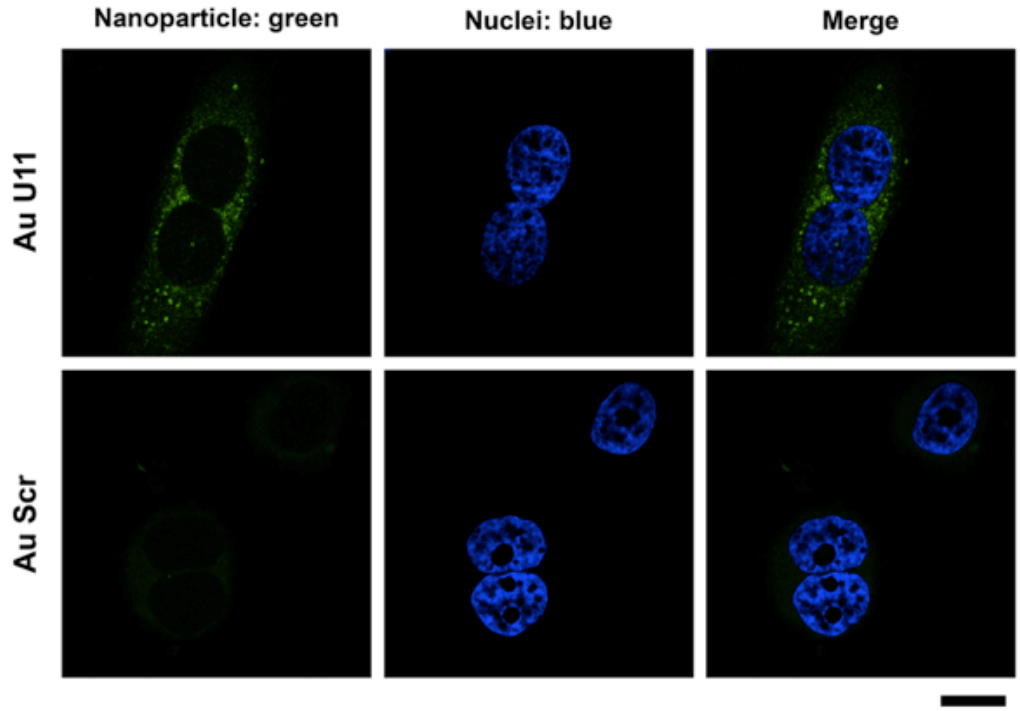

Fig. 37 Confocal microscopy study of uPAR targeting with Au-U11 and Au-U11scr NPs on MDA MB 468 ($uPAR^+$) cells. Cells were incubated for 1 h at 37 °C with 2 nM particle concentration. Nuclei were stained with 4',6-diamidino-2-phenyl-indole (DAPI) Scale bar = 10 µm.

3.1.4 AuU11 cytotoxicity

In order to exclude possible cytotoxic effects of Au-U11 NPs, cell death was evaluated by the Annexin V assay at 1, 3 and 24 h after labeling (**Fig. 38 A**). No evidence of cytotoxicity was observed in MDA MB 468 cells at the dosage used (0.5, 2 and 4 nM). 3-(4,5-Dimethylthiazol-2-yl)-2,5-diphenyltetrazolium bromide (MTT) assay was performed to evaluate the effect of Au-U11 NPs on cell viability. The data demonstrate that the nanoparticles induced minimal *in vitro* cytotoxicity at a concentration of up to 4 nM (**Fig. 38 B**).

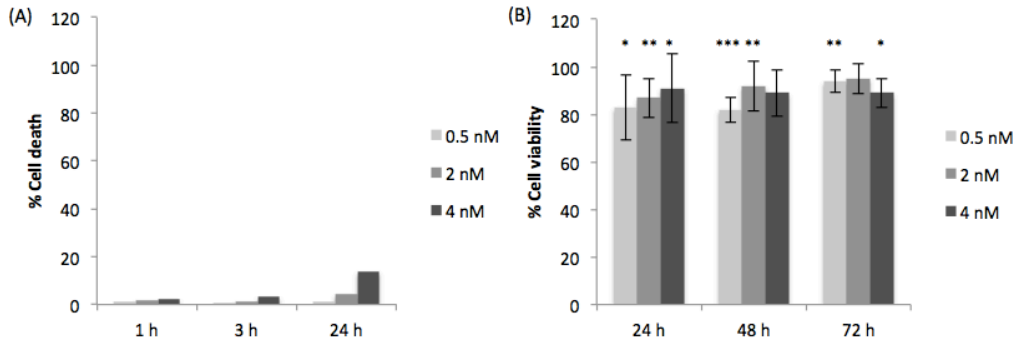

Fig. 38 A) Cell death assay with Au-U11 NPs. MDA MB 468 cells were treated with Au-U11 NPs (0.5, 2 and 4 nM) for 1, 3 and 24 h. Cells death was assessed to measure the exposure of Annexin V evaluated by flow cytometry. The percentage of cell death in untreated population was subtracted. B) Cell viability assessed by the MTT assay with Au-U11 NPs. MDA MB 468 cells were treated with Au-U11 NPs (0.5, 2 and 4 nM) for up to 72 h. The results are expressed as means ± S.D. of 6 individual experiments normalized on cell proliferation of untreated cells. T-student analysis are calculated compare to untreated control.

3.2 From phage display to breast cancer cells targeting with peptide conjugated gold nanoparticles

TumorHoPe is a manually curated comprehensive database containing 744 entries of experimentally characterized tumor homing peptides.[185] These peptides recognize tumor tissues and the tumor-associated micro environment, including tumor metastasis. We chose three peptides specific for HER2 receptor, which is overexpressed in some breast cancer cell lines like MCF7, and conjugated them to AuNPs, in order to evaluate their binding efficiency.

3.2.1 Peptide selection

LTVSPWY peptide (Peptide 1) was identified using a biopanning procedure by Shadidi *et al*. showing strong binding to SKBR3 and T47D breast cancer cell lines.[186] Then, it was conjugated to magnetic nanoparticles for selective targeting of HER2-positive tumor cells (SKOV3). *In vitro* studies using magnetic nanoparticles functionalized with LTVSPWY peptide revealed the nanoconjugates to be taken up selectively showing low cytotoxicity.[187] WNLPWYYSVSPT peptide (Peptide 2) was identified by phage display, and showed a strong binding to breast cancer cell lines SKBR3, T47D, MCF7, and PM-1. Importantly, no binding of the peptides 1 and 2 was observed to human

normal cells from different origin, such as mammary epithelial cells (HMEC), peripheral blood mononuclear cells (PBMC), umbilical vein endothelial cells, normal colon fibroblast, and human $CD34^+$ bone marrow cells.[186] RGDPAYQGRFL peptide (Peptide 3) was identified by Kaur *et al.* by a peptide array-whole cell interaction approach.[188] Flow cytometry and confocal microscopy studies showed that the RGD-motif containing peptide was highly selective to MDA MB 435 and MCF7 cancer cells, but had very little affinity for control HUVEC cells. RGDPAYQGRFL peptide was also conjugated to PEO-*b*-PCL diblock polymeric micelles to obtain targeted carrier systems.[189]

3.2.2 Peptide design and synthesis

Peptide sequences 1-3 were modified introducing 5(6)-carboxyfluorescein (FAM) at the N-terminus along with a β-alanine spacer. The same spacer was introduced at the carboxyl terminus to distantiate the binding sequence from the dipeptide ArgCys introduced for nanoparticles conjugation (Cys) and to increase water solubility (Arg). Peptide 4 was prepared as negative control and had inverted amino acid sequence of the peptide 1 (scrambled). All the peptides were synthesized by Fmoc solid phase synthesis and FAM was introduced before cleavage using EDAC activation.

3.2.4 AuNPs bioconjugation

For Au-peptide NPs preparation, peptides were chemically conjugated to the nanoparticles. In this case, direct conjugation of the peptides to GNPs, even in small amounts (1-5% of total ligand amount), led to insufficient colloidal stability and further nanoparticle aggregation. This is probably due to high peptide hydrophobicity and possible electrostatic interactions between positive charges present in peptide chains and negatively charged surface of GNPs. Rather, we succeeded in obtaining stable NPs by stabilization and functionalization with a shell of thiolated ligands containing a short PEG-OH (11-mercaptoundecyl-tetra(ethylene glycol)) plus a small amount of cystamine linker, a small disulfide, containing molecule with primary amines at both ends. The cystamine-modified NPs are then activated with a NHS-$(EG)_8$-maleimide linker and conjugated with the peptides *via* cysteine residue. This method is supposed to improve the accessibility of the peptide ligands, and, subsequently, of the amino acid residues to be recognized by the cells. A TEM image of as-obtained NPs and mean size distribution diagram are reported in **Fig. 39**.

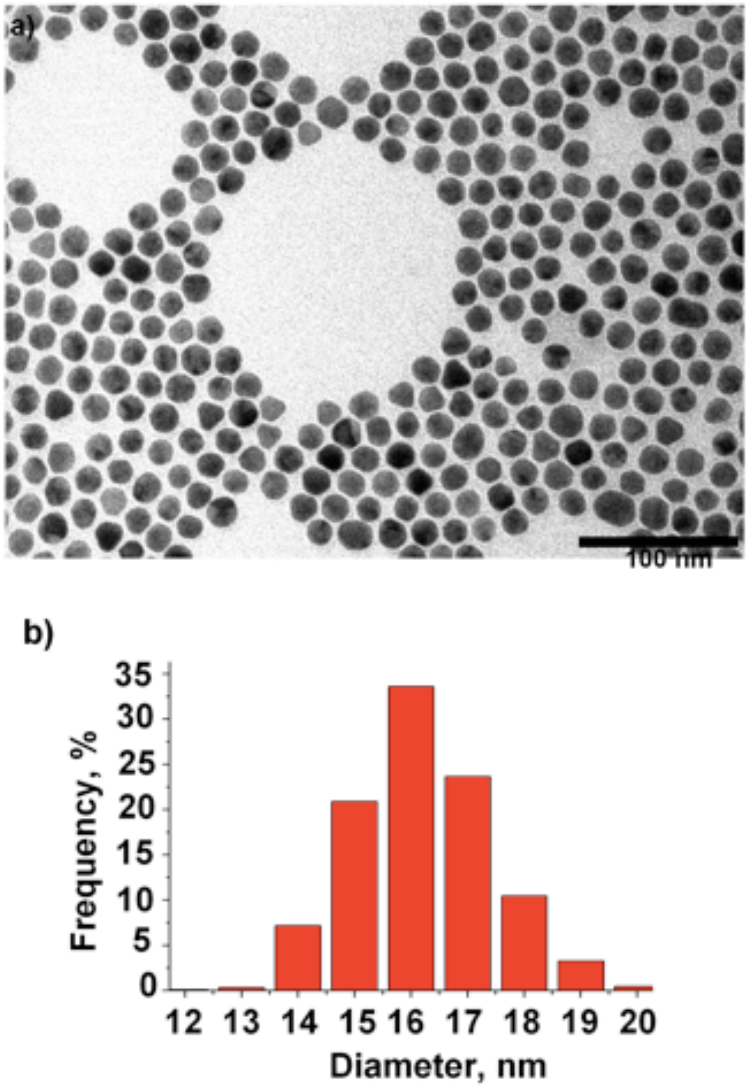

Fig. 39 a) TEM image, scale bar = 100 nm; and b) mean particle diameter distribution of Au-peptide NPs.

A red-shift from 518 to 524 nm occurred when citrate ions were substituted by PEG-OH and cystamine molecules. An increase of LSPR (Local Surface Plaasmon Resonance) band absorbance was indicative of a change in the environment surrounding the particles. Importantly, the particles remained stable and no change in LSPR band was found after repeated centrifugation and final re-dispersion in PBS for further coupling. After NHS-$(EG)_8$-maleimide conjugation, a further shift of 3 nm occurred. Finally, when

peptide ligands were attached, the LSPR band with a slightly different shape was detected around 527 nm, indicating a successful coupling reaction. A further confirmation of successful peptide conjugation was obtained by fluorescence spectroscopy. To avoid false negative results due to possible fluorescence quenching by AuNPs, we decided to detach the peptides from nanoparticle surface by incubation with a dithiothreitol (DTT) solution. The analysis showed the presence of an intense emission band at 519 nm attributed to the FITC-functionalized peptides (**Table 6**).

Table 6 Local surface plasmon resonance (LSPR) values of peptide functionalized AuNPs and fluorescence values of the nanoconjugates at emission wavelength of 519 nm.

Sample	Local Surface Plasmon Resonance (LSPR, nm)	Fluorescence Intensity (FI)
Au-P1	527	$6.5\ 10^7$
Au-P2	527	$1.2\ 10^8$
Au-P3	527	$8{,}5\ 10^7$
Au-P4	527	$1.1\ 10^8$

Table 7 shows further characterization of Au-peptide conjugates. The mean hydrodynamic diameter of nanoconjugates found by DLS was around 27-36 nm with a narrow polydispersity index ranging from 0.21 to 0.27. The ζ-potential values show that the nanoconjugates were negatively charged, with values between −11 and −8 mV.

Table 7 Amino acid sequences of peptides and characterization of Au-peptide NPs by dynamic light scattering (DLS) and ζ-potential.

Sample	Amino acid sequence	DLS (nm)	Z-potential (mV)
Au-P1	FAM-βA-LTVSPWY-βARC	27.0	− 9.2
Au-P2	FAM-βA-WNLPWYYSVSPT-βARC	31.2	− 8.7
Au-P3	FAM-βA-RGDPAYQGRFL-βARC	30.0	− 10.0
Au-P4	FAM-βA-WSPLTYV-βARC	36.3	− 11.0

3.2.5 Au-peptide NPs targeting capability

To study specific binding of Au-peptide nanoconjugates by cancerous cells, we used MCF7 human breast cancer cells, while murine 3T3-L1 fibroblast noncancerous cells were used as negative control. Although a specific targeting receptor of these peptides on MCF7 cells has not been identified, their strong affinity for this cell line is proven. Fluorescence-based flow cytometry was used to monitor the binding both of free peptides and of Au-peptide NPs during *in vitro* experiments. Free peptides were incubated with MCF7 cells (5×10^5 cells) at 1 and 10 μg mL^{-1} for 1 h. Incubation at 4 °C allowed to minimize receptor-mediated endocytosis. Results show that peptides 1-3 are able to specifically bind MCF7 cells in a concentration-dependent manner. As expected, scrambled peptide 4 showed no specific binding to MCF7 cells (**Fig. 40**).

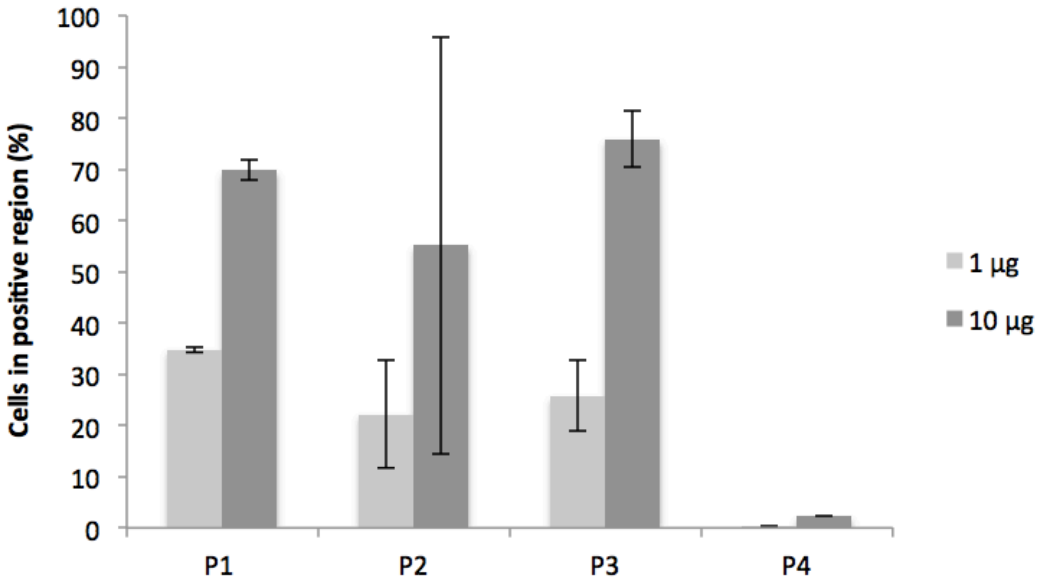

Fig. 40 Cellular binding of peptide 1 (P1), peptide 2 (P2), peptide 3 (P3) and peptide 4 (scrambled peptide, P4) to MCF7 breast cancer cells at 1 μg mL^{-1} (fuxia column) and 10 μg mL^{-1} (blue column) concentrations by flow cytometry. The results are expressed as means ± S.D. of 3 individual experiments normalized on untreated cells.

Once verified the specificity of the peptides to MCF7 cells, we examined the binding efficiency of Au-peptide NPs. For this purpose, nanoparticles were incubated with MCF7 and 3T3-L1 cells (5×10^5) for 1 h at 4 °C at two different concentrations: 4 nM and

8 nM. Flow cytometry showed a remarkable increase in the fluorescence signal strongly dependent on nanoparticle concentration, while this change was absent when NPs were incubated with 3T3-L1 cells (**Fig. 41**). The values show a nearly double increase in mean fluorescence intensity when the concentration of Au-peptide 1-3 NPs rises from 4 nM to 8nM, confirming that Au-peptide NPs bind selectively and in a concentration dependent manner to MCF7 cells. In contrast, no fluorescence labelling was observed even at the highest concentration when Au-peptide 4 NPs were incubated with both MCF7 and 3T3-L1 cells, suggesting that peptide 1-3 maintained their ability to recognize MCF7 cells when conjugated to NPs. In particular, Au-peptide 1 NPs showed the highest affinity toward MCF7 cells, probably due to better peptide solubility and good colloidal stability.

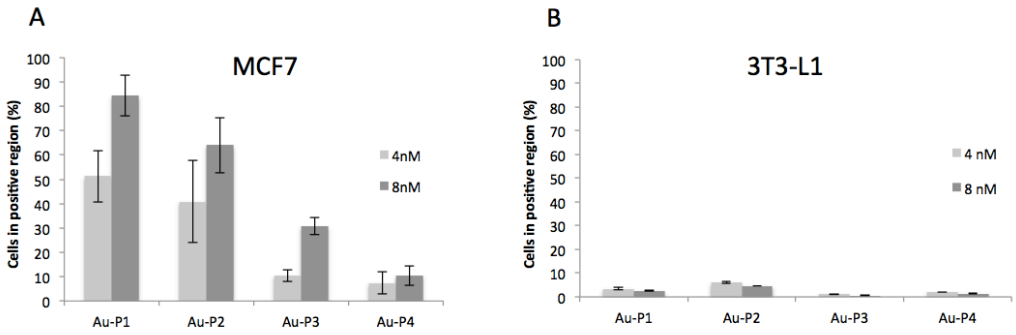

Fig. 41 A) Cellular binding of AuNPs functionalized by peptide 1, peptide 2, peptide 3 and scrabled peptide 4 to (A) MCF7 breast cancer cells at 4 nM (fuxia column) and 8 nM (blue column) concentrations and to (B) noncancerous 3T3-L1 fibroblast cells at 4 nM (green column bar) and 8 nM (blue column) concentrations by flow cytometry. The results are expressed as means ± S.D. of 3 individual experiments normalized on untreated cells.

3.2.6 Au-peptide NPs cytotoxicity

For both *in vivo* and *in vitro* application of nanoconjugates, it is fundamental for them to show low cytotoxicity. In order to insure the safety of Au-peptide NPs *in vitro*, we performed cell death experiments on MCF7 cells. After 24 h of incubation with Au-peptide NPs at 4 nM and 8 nM concentration, cell death did not exceed 3% level, confirming low general cytotoxicity of the nanoparticles (**Fig. 42**)

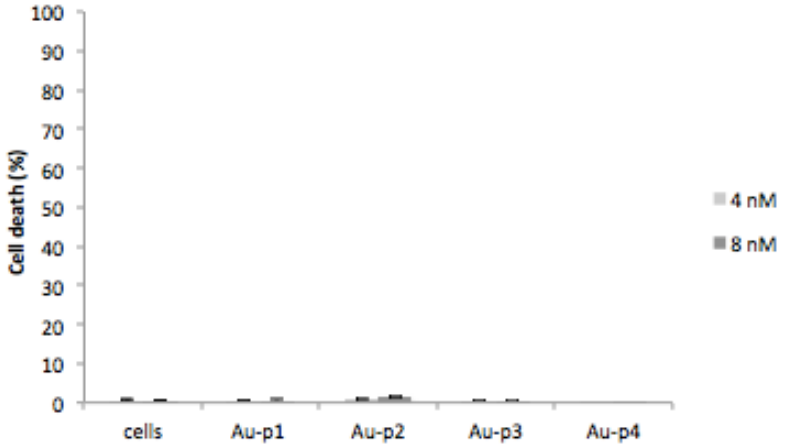

Fig. 42 Cell death assay with Au-peptide NPs. MCF7 cells were treated with AuNPs functionalized with peptide 1-4 (4 and 8 nM) for 24 h. Cells death was assessed by measuring exposure of Annexin V evaluated by flow cytometry. The percentage of cell death in untreated population was subtracted. The results are expressed as means ± S.D. of 3 individual experiments normalized on untreated cells.

Conclusions

In the last years, much of nanotechnologyes investigations focused on the possibility to produce nanoconjugates between nanoparticles and biomolecules. However, despite considerable progress, nowadays no structural and functional characterization studies of immobilized proteins are available. In this work, we aimed to evaluating the effect of proteins bioconjugation, in terms of structural characterization and oriented immobilization, onto nanoparticles surfaces.

We initially synthesized a Trastuzumab-modified iron oxide nanoparticle (TMNP) in order to study its conformational changes depending on the conjugation method. We demonstrated for the first time that accurate analysis of the FTIR signals in the 1500-1700 cm^{-1} absorption range may be a valuable method enabling the determination of protein conformational modifications in mAb conjugates. These studies revealed that mAb conjugation to the nanoparticles surface via a dicarboxylic PEG linker did not affect its structural properties maintaining its overall fold, unlike. mAb physically adsorbed onto the same nanoparticles. In this case mAb lost its native conformation. This simple and fast structural characterization tool is versatile and of wide utility because it might be easily applied to other typologies of proteins and nanoparticles. As the functionality of a protein is related to its native fold, our FTIR data provide preliminary evidence that the protein in this biohybrid nanoconjugate system retains its native conformation.

Subsequently, we studied conjugation strategies derived to control protein and peptide positioning on multifunctional nanoparticles. We developed three new modular approaches for the immobilization on iron oxide nanoparticles of peptide ligands selective for targeting to specific cancer cells. These methods take advantage of recombinant DNA technology to suitably modify protein sequence in view of defined experimental goals. In

particular, we produced an scFv antibody variant in N-terminal-linked fusion with SNAP; an HALO-U11 bimodular genetic fusion and a cutinase enzyme also fused with the small peptide U11. The advantages of these approaches are: 1) the targeting peptide was produced in fusion with a capture domain by recombinant expression, which allowed us to easily obtain the protein at high purity and avoided traditional chemical procedures; 2) the recombinant peptide was designed to achieve an efficient covalent conjugation to MNP functionalized with simple linkers in an orientation-controlled manner; 3) selective immobilization was accomplished by an enzymatic biorecognition event, which prevented nonspecific adsorption, provided that MNP were properly pegylated. The potential of this strategy for nanoparticles bioengineering was demonstrated studying the targeting efficiency of SSMFN on $HER2^+$ breast cancer cell line and of MNP-H11 and CUT-U11 on $uPAR^+$, breast cancer cell lines. This method is simple and versatile and offers a new solution for the covalent immobilization on MNP of active homing ligands direct to a broad spectrum of specific biomarkers. This approach can be considered of general value for the development of targeted nanoparticles for biomedical applications.

Finally we tried to conjugate the small peptide U11 and other four peptides (peptide 1-4) selected from a phage displayed peptide library, on gold nanoparticles (AuNPs). U11 peptide was shown to form β-sheets on the surface of liposomes when inserted at high concentrations. However, at low concentrations, the same peptide-lipid NP appear to rearrange into more separated structures.[173] Similarly, we observed that magnetite nanoparticles conjugated to U11 peptide were not able to bind $uPAR^+$ cells better than to $uPAR^-$ ones, probably, owing to disadvantageous peptide rearrangement or its low availability recognition.[79] Therefore, it is evident that the structure of targeting molecule and its distribution on the nanoparticle surface play an important role in both their colloidal stability and the interaction with cellular membrane receptors. Among different nanoparticles, we proved that AuNPs would be a good candidate for peptide immobilization because of the formation of self assembled monolayer on their surface.[190] Here, we have shown that biocompatible fluorescent AuNPs can be successfully derivatized with both U11 and peptides 1-4, thus efficient targeting to $uPAR^+$ and $HER2^+$ breast cancer cells, respectively. Peptides were inserted in a mixed monolayer of ligands imparting their stability, reducing their adsorption and reducing nonspecific interactions between biological target and AuNPs surface due to high surface density of PEG chain. This allows also for a better organization of the peptide on the nanoparticle surface to

avoid β-sheets formation. The simple and fast conjugation method of AuNPs with small peptides can be easily applied to a wide range of peptides. The production of stable nanoconjugates depends on the amount of immobilized peptides, which might be optimized when needed.

In summary, in this work, a new and versatile platform for biomolecules conjugation with a high control in terms of conformation and orientation, onto colloidal and multifunctional nanoparticles is presented.

Results from this work represent a solid base for the development of a new generation of nanoconjugates for medical and biotechnological applications.

Bibliography

[1] Kim, B. Y. S.; Rutka, J. T.; Chan, W. C. W. Nanomedicine. *N. Engl. J. Med* **2010**, *363*, 2434-2443.

[2] Archakov, A. I.; Ivanov, Y. D.; Analytical nanobiotechnology for medicine diagnostics. *Mol. Bio. Syst.* **2007**, *3*, 336-342.

[3] Pautler, M.; Brenner, S.; Nanomedicine: promises and challenges for the future of public health. Int. J. *Nanomedicine* **2010**, *5*, 803-809.

[4] Bawarski, W. E.; Chidlowsky, E.; Bharali, D. J.; Mousa, S. A. Emerging nanopharmaceuticals. *Nanomedicine* **2008**, *4*, 273-282.

[5] Ferrari, M. Cancer nanotechnology: opportunities and challenges. *Nat. Rev. Cancer* **2005**, *5*, 161-171.

[6] Alivisatos, A. P. Less is more in Medicine. *Sci. Am.* **2001**, 67-73.

[7] Peer, D.; Karp, J. M.; Hong, S.; Farokhzad, O. C.; Margalit, R.; Langer, R. Nanocarriers as an emerging platform for cancer therapy. *Nat. Nanotech*. **2007**, *2*, 751-760.

[8] McCarthy, T. D.; Karellas, P.; Henderson, S. A.; Giannis, M.; O'Keefe, D. F.; Heery, G.; Paull, J. R. A.; Matthews, B. R.; Holan, G. Dendrimers as drugs: discovery and preclinical and clinical development of dendrimer-based microbicides for HIV and STI prevention. *Mol. Pharm*. **2005**, *2*, 312-318.

[9] Davis, M. E.; Zuckerman, J. E.; Choi, C. H. J.; Seligson, D.; Tolcher, A.; Alabi, C. A.; Yen, Y.; Heidel, J. D.; Ribas, A. Evidence of RNAi in humans from systemically administered siRNA via targeted nanoparticles. *Nature* **2010**, *464*, 1067-70.

[10] Rsch-Genger, U.; Grabolle, M.; Cavaliere-Jaricot, S.; Nitschke, R.; Nann, T. Quantum dots versus organic dyes as fluorescent labels. *Nat. Methods* **2008**, *5*, 763-775.

[11] Sperling, R. A.; Riviera-Gil P.; Zhang, F.; Zanella, M.; Parak, W. J. Biological applications of gold nanoparticles. *Chem. Soc. Rev*. **2008**, *37*, 1896-1908.

[12] Liu, Z. A.; Li, X. L.; Tabakman, S. M.; Jiang, K. L.; Fan, S. S.; Dai, H. J. Multiplex multicolor Raman imaging of live cells with isotipically modified single walled carbon nanotubes. *J. Am. Chem. Soc*. **2008**, *130*, 13540-13541.

[13] Hobbs, S. K.; Monsky, W. L.; Yuan, F.; Roberts, G.; Griffith, L.; Torchilin, V. P.; Jain R. K. Regulation of transport pathways in tumor vessels: role of tumor type and microenvironment. *Proc. Natl. Acad. Sci. U.S.A.* **1998**, *95*, 4607-4612.

[14] Prencipe, G.; Tabakman, S. M.; Welsher, K.; Liu, Z.; Goodwin, A. P.; Zhang, L.; Henry, J.; Di, H. PEG branched polymer for functionalization of nanomaterials with ultralong blood circulation. J. Am. Chem. Soc. 2009, 131, 4783-4787.

[15] Alexis, F.; Pridgen, E.; Molnar, L. K.; Farokhzad, O. C. Factors affecting the clearance and biodistribution of polymeric nanoparticles. *Mol. Pharm*. **2008**, *5*, 505-515.

[16] Postuma-Trumpie, G. A.; Korf, J.; van Amerongen, A. V. Lateral flow (immuno)assay: its strengths weaknesses, opportunities and threats: a literature survey. *Anal Bioanal. Chem*. **2009**, *393*, 569-582.

[17] Nam, J. M.; Thaxton, C. S.; Mirkin, C. A. Nanoparticle-based bio-bar codes for the ultrasensitive detection of proteins. *Science* **2003**, *301*, 1884-1886.

[18] Thaxton, C. S.; Elghanian, R.; Thomas, A. D.; Stoeva, S. I.; Lee, J. S.; Smith, N. D.; Schaeffer, A. J.; Klocker, H.; Horninger, W.; Bartsch, G.; Mirkin, C. A. Nanoaprticle-based bio-barcode assay redefines “undetectable” PSA and biochemical recurrence after radical prostatectomy. *Proc. Natl. Acad. Sci. U.S.A*. **2009**, *106*, 18437-18442.

[19] Kho, K. W.; Shen, Z. X.; Zeng, H. C.; Soo K. C.; Olivo, M. Deposition method for preparing SERS-active gold nanoparticle substrates. *Anal. Chem*. **2005**, *77*, 7462-7471.

[20] Lammers, T.; Aime, S.; Hennink, W. E.; Storm, G.; Kiessling, F. *Theranostic nanomedicine. Acc. Chem.* Res. DOI: 10.1021/ar200019c.

[21] Michalet, X.; Pinaud, F. F.; Bentolila, L. A.; Tsay, J. M.; Doose, S.; Li, J. J.; et al. Quantum dots for live cells, in vivo imaging and diagnostic. *Science* **2005**, *307*, 538-544.

[22] Smith, A. M.; Duan, H.; Mohs, A. M.; Nie, S. Bioconjugated quantum dots for *in vivo* molecular and cellular imaging. *Adv. Drug Del. Rev*. **2008**, *60*, 1226-1240.

[23] Rhyner, M. N.; Smith, A. M.; Gao, X.; Mao, H.; Yang, L.; Nie, S. Quantum dots and multifunctional nanoparticles: new contrast agents for tumor imaging. *Nanomedicine* **2006**, *1*, 209-217.

[24] Harisinghani, M. G.; Barentsz, J.; Hahn, P. F.; Deserno, W. M.; Tabatabaei, S.; Van de Kaa, C. H.; et al. Noninvasive detection of clinically occult lymph-node metastases in prostate cancer. *N. Engl. J. Med*. **2003**, *348*, 2491-2499.

[25] Engenov, N. V.; Medarova, Z.; Dai, G.; Bonner-Weir, S.; Moore, A. In vivo imaging of islet transplantation. *Nat. Med*. **2006**, *12*, 144-148.

[26] Barnett, B. P.; Arepally, A.; Karmarkar, P. V.; Qian, D.; Gilson, W. D.; Walczak, P.; et al. Magnetic resonance-guided, real-time targeted delivery and imaging of magnetocapsules immunoprotecting pancreatic islet cells. *Nat. Med*. **2007**, *13*, 986-991.

[27] El-Boubbou, K.; Gruden, C.; Huang, X.; Magnetic Glyco-nanoparticles: a unique tool for rapid pathogen detection, decontamination, and strain differentiation. *J. Am. Chem. Soc*. **2007**, *129*, 13392-13393.

[28] Fortin, J. P.; Wilhelm, C.; Servais, J.; Menager, C.; Bacri, J. C.; Gazeau, F. Size-sorted anionic iron oxide nanomagnets as colloidal mediators for magnetic hypertermia. *J. Am. Chem. Soc*. **2007**, *129*, 2628-2635.

[29] Grzelczac, M.; Perez-Juste, J.; Mulvaney, P.; Liz-Marzàn, L. M. Shape control in gold nanoparticle synthesis. *Chem Soc. Rev*. **2008**, *37*, 1783-1791.

[30] Ghosh, P.; Han, G.; De, M.; Kim, C. K.; Rotello, V. M. Gold nanoparticles in delivery application. *Adv. Drug. Del. Rev*. **2008**, *60*, 1307-1315.

[31] Halas, N. J. Nanoscience under glass: the versatile chemistry of silica nanostructures, Perspectives, *ACS Nano* **2008**, *2*, 179-183.

[32] Tallury, P.; Payton, K. and Santra, S. Silica-based multimodal/multifunctional nanoparticles for bioimaging and biosensing applications. *Nanomedicine.* **2008**, *3*, 579–592.

[33] Chu, Z.; Huang, Y.; Tao, Q.; Li, Q. Cellular uptake, evolution, and excretion of silica nanoparticles in human cells. *Nanoscale* **2011**, *3*, 3291–3299.

[34] Council of the Canadian Academies. Small is different: a science perspective on the regulatory challenges of the nanoscale. July **2008**. (http://www.nanolawreport.com/)

[35] Schroeder, A.; Heller, D. A.; Winslow, M. M.; Dahlman, J. E.; Pratt, G. W.; Langer, R.; Jacks, T.; Anderson, D. G. Treating metastatic cancer with nanotechnology. *Nat. Rev. Cancer*. **2012**, *12*, 39-50.

[36] Craig, G. E.; Brown, S. D.; Lamprou, D. A.; Graham, D.; Wheate, N. J. Cisplatin-tethered gold nanoparticles that exhibit enhanced reproducibility, drug loading, and stability: a step closer to pharmaceutical approval? *Inorg. Chem.* **2012**, *51*, 3490–3497.

[37] Gibson, J. D.; Khanal, B. P.; Zubarev, E. R. Paclitaxel-functionalized gold nanoparticles. *J. Am. Chem. Soc.* **2007**, *129*, 11653–11661.

[38] Zhang, X.-Q.; Lam, X.; Xu, R.; Giljohann, D.; Ho, D.; Mirkin, C. A. Strategy for increasing drug solubility and efficacy through covalent attachment to polyvalent DNA-nanoparticle conjugates. *ACS Nano* **2011**, *5*, 6962–6970.

[39] You, J.; Zhang, G.; Li, C. Exceptionally high payload of doxorubicin in hollow gold nanospheres for near-infrared light-triggered drug release. *ACS Nano* **2010**, *4*, 1033-1041.

[40] Asadishad, B.; Vossoughi, M.; Alemzadeh, I. Upconversion Nanomaterials: Synthesis, Mechanism, and Applications in Sensing *Ind. Eng. Chem. Res.* **2010**, *49*, 1958–1963.

[41] Wang, F.; Wang, Y.-C.; Dou, S.; Xiong, M.-H.; Sun, T.-M.; Wang, J. Doxorubicin-tethered responsive gold nanoparticles facilitate intracellular drug delivery for overcoming multidrug resistance in cancer cells. *ACS Nano* **2011**, *5*, 3679–3692.

[42] Park, H.; Yang, J.; Lee, J.; Haam, S.; Choi, I.-H.; Yoo, K.-H. Multifunctional nanoparticles for combined doxorubicin and photothermal treatments. *ACS Nano* **2009**, *3*, 2919–2926.

[43] Zhang, X.; Chibli, H.; Mielke, R.; Nadeau. J. Ultrasmall gold-doxorubicin conjugates rapidly kill apoptosis-resistant cancer cells. *Bioconjugate Chem.* **2011**, *22*, 235–243.

[44] Alexander, C. M.; Dabrowiak, J. C.; Maye, M. M. Investigation of the drug binding properties and cytotoxicity of DNA-capped nanoparticles designed as delivery vehicles

for the anticancer agents doxorubicin and actinomycin D. *Bioconjugate Chem.* **2012**, *23*, 2061–2070.

[45] Luo, Y.-L.; Shiao, Y.-S.; Huang, Y.-F. Release of photoactivatable drugs from plasmonic nanoparticles for targeted cancer therapy. *ACS Nano* **2011**, *5*, 7796–7804.

[46] Choi, H. S.; Liu, W.; Liu, F.; Nasr, K.; Misra, P.; Bawendi, M. G.; frangioni, J. V. Design considerations for tumor-targeted nanoparticles. *Nat. Nanotechnol* **2010**, *5*, 42-47.

[47] Chomoucka, J.; Drbohlavova, J.; Huska, D.; Adam, V.; Kizek, R.; Hubalek, J. Magnetic nanoparticles and targeted drug delivering. *Pharmacol. Res*. **2010**, *62*, 144-149.

[48] De, M.; Ghosh, P. S.; Rotello, V. M. Applications of Nanoparticles in Biology. *Advanced Materials* **2008***, 20*, 4225–4241.

[49] Ghosh, P.; Han, G.; De, M.; Kim, C. K.; Rotello, M. V. Gold nanoparticles in delivery applications. *Adv. Drug Deliv. Rev.* **2008***, 60*, 1307–1315.

[50] Shellman, Y.; Howe, W. R.; Miller, L. A.; Goldstein, N. B., Pacheco, T. R.; Mahajan, R. L.; LaRue, S. M.; Norris, D. A. Hypertermia induces endoplasmic reticulum-mediated apoptosis in melanoma and non-melanoma skin cancer cells. *J. Invest. Dermatol.* **2008**, *128*, 949-956.

[51] Nam, J.; Won, N.; Jin, H.; Chung, H.; Kim, S. pH-Induced aggregation of gold nanoparticles for photothermal cancer therapy. *J. Am. Chem. Soc.* **2009**, *131*, 13639–13645.

[52] Khlebtsov, B. N.; Panfilova, E. V.; Terentyuk, G. S.; Maksimova, I. L.; Ivanov, A. V.; Khlebtsov, N. G. Plasmonic nanopowders for photothermal therapy of tumors. *Langmuir* **2012**, *28*, 8994–9002.

[53] Haba, Y.; Kojima, C.; Harada, A.; Ura, T.; Horinaka, H.; Kono, K. Preparation of poly(ethylene glycol)-modified poly(amido amine) dendrimers encapsulating gold nanoparticles and their heat-generating ability. *Langmuir* **2007**, *23*, 5243–5246.

[54] Ibrahimkutty, S.; Kim, J.; Cammarata, M.; Ewald, F.; Choi, J.; Ihee, H.; Plech, A. Ultrafast structural dynamics of the photocleavage of protein hybrid nanoparticles. *ACS Nano* **2011**, *5*, 3788–3794.

[55] Pitsillides, C. M.; Joe, E. K.; Wei, X.; Anderson, R. R.; Lin. C. P. Selective cell targeting with light-absorbing microparticles and nanoparticles. *Biophys J.* **2003**, *84*, 4023–4032.

[56] Ren, J.; Shen, S.; Pang, Z.; Lu, X.; Deng, C.; Jiang, X. Facile synthesis of superparamagnetic Fe_3O_4@Au nanoparticles for photothermal destruction of cancer cells. ***Chem. Commun.*** **2011**, ***47***, 11692-11694.

[57] Wang, J.; Zhu, G.; You, M.; Song, E.; Shukoor, M. I.; Zhang, K.; Altman, M. B.; Chen, Y.; Zhu, Z.; Huang, C. Z.; Tan, W. Assembly of aptamer switch probes and photosensitizer on gold nanorods for targeted photothermal and photodynamic cancer therapy. *ACS Nano* **2012**, *6*, 5070–5077.

[58] Chen, J.; Glaus, C.; Laforest, R.; Zhang, Q.; Yang, M.; Gidding, M.; Welch, M. J.; Xia, Y. Gold nanocages as photothermal transducers for cancer treatment. *Small* **2010**, *6*, 811–817.

[59] Cheng, L.-C.; Huang, J.-H.; Chen, H.-M.; Lai, T.-C.; Yang, K.-Y.; Liu, R.-S.; Hsiao, M.; Chen, C.-H.; Her, L.-J.; Tsai, D. P. Seedless, silver-induced synthesis of star-shaped gold/silver bimetallic nanoparticles as high efficiency photothermal therapy reagent. J Mater Chem, 22(5), 2244-2253. ***J. Mater. Chem.*** **2012**, ***22***, 2244-2253.

[60] Khan, S. A.; Singh, A. K.; Senapati, D.; Fan, Z.; Ray, P. C. Bio-conjugated popcorn shaped gold nanoparticles for targeted photothermal killing of multiple drug resistant Salmonella DT104 ***J. Mater. Chem.*** **2011**, ***21***, 17705-17709.

[61] Wust, P.; Hildebrandt, B.; Sreenivasa, G.; Rau, B.; Gellermann, J.; Riess, H.; Felix, R.; Schlag, P. M. Hypertermia in combined treatment of cancer. *Lancet Oncol*. **2002**, *3*, 487-497.

[62] Weissleder, R.; Mahmood, U. Molecular imaging. *Radiology* **2001**, *219*, 316-333.

[63] Corot, C.; Robert, P.; Idée, J. M.; Port, M. Recent advances in iron oxide nanocrystal technology for medical imaging. *Adv. Drug. Delivery Rev*. **2006**, *58*, 1471-1504.

[64] Mendoca Dias, M. H.; Lauterbur, P. C. Ferromagnetic particles as contrast agents for magnetic resonance imaging of liver and spleen. *Magn. Reson. Med*. **1986**, *3*, 328-330.

[65] Semelka, R. C.; Helmberger, T. K. Contrast agents for MR Imaging of the liver. *Radiology* **2001**, *218*, 27-38.

[66] Morawski, A. M.; Winter, P. M.; Crowder, K. C.; Caruthers, S. D.; Furhrhop, R. W.; Scott, M. J.; Robertson, J. D.; Abesdschein, D. R.; Lanza, G. M.; Wickline, S. A. Targeted nanoparticles for quantitative imaging of sparse molecular epitopes with MRI. *Magn. Reson. Med*. **2004**, *51*, 480-486.

[67] Lan, T.; Dong, C. Q.; Huang, X. Y.; Ren, J. C. Single particle technique for one-step homogeneous detection of cancer marker using gold nanoparticle probes. *Analyst* **2011**, *136*, 4247−4253.

[68] Popovtzer, R.; Agrawal, A.; Kotov, N. A.; Popovtzer, A.; Balter, J.; Carey, T. E.; Kopelman, R. Targeted gold nanoparticles enable molecular CT imaging of cancer. *Nano Lett.* **2008**, *8*, 4593–4596.

[69] Kim, D.; Park, S.; Lee, J. H.; Jeong, Y. Y.; Jon. S. Antibiofouling polymer-coated gold nanoparticles as a contrast agent for in vivo X-ray computed tomography imaging. *J. Am. Chem. Soc.* **2007**, *129*, 7661–7665.

[70] Guo, R.; Wang, H.; Peng, C.; Shen, M.; Pan, M.; Cao, X.; Zhang, G.; Shi. X. Theoretical exploration of the structural, electronic, and magnetic properties of ZnO nanotubes with vacancies, antisites, and nitrogen substitutional defects. *J. Phys. Chem.* **2010**, *114*, 60–66.

[71]Mallidi, S.; Larson, T.; Tam, J.; Joshi, P. P.; Karpiouk, A.; Sokolov, K.; Emelianov, Multiwavelength photoacoustic imaging and plasmon resonance coupling of gold nanoparticles for selective detection of cancer. S. *Nano Lett.* **2009**, *9*, 2825–2831.

[72] El-Sayed, I. H.; Huang, X.; El-Sayed, M. A. Surface plasmon resonance scattering and absorption of anti-EGFR antibody conjugated gold nanoparticles in cancer diagnostics: applications in oral cancer. *Nano Lett.* **2005**, *5*, 829–834.

[73] Huang, X.; El-Sayed, M. A. Gold nanoparticles: Optical properties and implementations in cancer diagnosis and photothermal therapy *Journal of Advanced Research* **2010**, *1*, 13–28.

[74] Shah, N. B.; Dong, J.; Bischof, J. C. Cellular uptake and nanoscale localization of gold nanoparticles in cancer using label-free confocal Raman microscopy. *Mol. Pharmaceutics* **2011**, *8*, 176–184.

[75] Occhipinti, E.; Verderio, P.; Natalello, A.; Galbiati, E.; Colombo, M.; Mazzucchelli, S.; Salvadè, A.; Tortora, P.; Doglia, S. M.; Prosperi, D. Investigating the structural biofunctionality of antibodies conjugated to magnetic nanoparticles. *Nanoscale* **2011**, *8*, 387-390.

[76] Corsi, F.; Fiandra, L.; De Palma, C.; Colombo, M.; Mazzucchelli, S.; Verderio, P.; Allevi, R.; Tosoni, A.; Nebuloni, M.; Clementi, E.; Prosperi, D. HER2 expression in breast cancer cells is downregulated upon active targeting by antibody-engineered multifunctional nanoparticles in mice. *ACS Nano* **2011**, *8*, 6383-6393.

[77] Colombo, M.; Sommaruga, S.; Mazzucchelli, S.; Polito, L.; Verderio, P.; Galeffi, P.; Corsi, F.; Tortora, P.; Prosperi, D. Site-specific conjugation of ScFvs antibodies to nanoparticles by bioorthogonal strain-promoted alkyne-nitrone cycloaddition. *Angew. Chem. Int. Ed. Engl*. **2012**, *161*, 496-499.

[78] Danhier, F.; Ansorena, F.; Silva, J. M.; Coco, R.; Le Breton, A.; Preat, V. PLGA-based nanoparticles: an overview of biomedical applications. *J. Controlled Release* **2012**, *161*, 505-522.

[79] Mazzucchelli, S.; Colombo, M.; Verderio, P.; Rozek, E.; Andreata, F.; Galbiati, E.; Tortora, P.; Corsi, F.; Prosperi, D. Orientation-controlled conjugation of haloalkane dehalogenase fused homing peptides to multifunctional nanoparticles for the specific recognition of cancer cells. *Angew. Chem. Int. Ed. Engl*. **2013**, *52*, 3121-3125.

[80] Jokerst, J. V.; Lobovkina, T.; Zare, R. N.; Gambhir, S. S. Nanoparticle PEGylation for imaging and therapy. *Nanomedicine* **2011**, *6*, 715-728.

[81] Mazzucchelli, S.; Verderio, P.; Sommaruga, S.; Colombo, M.; Salvadè, A.; Cprsi, F.; Galeffi, P.; Tortora, P.; Prosperi, D. Multiple presentation of Scfv800E6 on silica nanospheres enhances targeting efficiency toward HER-2 receptor in breast cancer cells. *Bioconjugate Chem*. **2011**, *22*, 2296, 2303.

[82] Huang, S.; Shao, K.; Kuang, Y.; Liu, Y.; Li, J.; An, S.; Guo, Y.; Ma, H.; He, X.; Jiang, C. Tumor targeting and microenvironment-responsive nanoparticles for gene delivery. Biomaterials, **2013**, 34, 5294-5302.

[83] Kocbek, P.; Kralj, S.; Kreft, M. E.; Kristl, J. Targeting intracellular compartments by magnetic polymeric nanoparticles. Eur. J. Pharm. Sci. **2013**, 50, 130-138.

[84] Moghimi, S. M.; Hunter, A. C.; Murray, J. C. Long-circulating and target-specific nanoparticle: theory to practice. *Pharmacol. Rev*. **2001**, *53*, 283-318.

[85] Moghimi, S. M.; Hunter, A. C. Poloxamers and poloxamines in nanoparticle engineering and experimental medicine. *Trends. Biotechnol* **2000**, *18*, 412-420.

[86] Montenegro, J. M.; Grazu, V.; Sukhanova, A.; Agarwal, S.; de la Fuente, J. M.; Nabiev, I.; Greiner, A.; Parak, W. J. Controlled antibody/(bio-)conjugation of inorganic nanoparticles for targeted delivery. *Adv. Drug. Deliv*. *Rev*. **2013**, *65*, 677-688.

[87] Barkey, N. M.; Tafreshi, N. K.; Josan, J. S.; De Silva, C. R.; Sill, K. N.; Hruby, V. J.; Gillies, R. J.; Morse, D. L.; Vagner, J. Development of melanoma-targeted polymer micelles by conjugation of a melancortin 1 receptor (MC1R) specific ligand. *J. Med. Chem*. **2011**, *54*, 8078-8084.

[88] Davis, M. E.; Chen Z. G.; Shin, D. M. Nanoparticle therapeutics: an emerging treatment modality for cancer. *Nat. Rev. Drug. Discov*. **2008**, *7*, 771-782.

[89] Powell Gray, B.; Li, S.; Brown, K. C. From phage display to nanoparticle delivery: functionalizing liposomes with multivalentpeptides improves targeting to a cancer biomarker. *Biocojug*. *Chem*. **2013**, *14*, 107-115.

[90] Petros, R. A.; De Simone, J. M. Strategies in the design of nanoparticles for therapeutic applications. *Nat. Rev. Drug Discovery*, **2010**, *9*, 615-627.

[91] Treuel, L.; Jiang, X.; Nienhaus, G. U. New views on cellular uptake and trafficking of manufactured nanoparticles. *J. R. Soc. Interface* **2013**, *10*, 20120939.

[92] Soenen, S. J. H.; Himmelreich, U.; Nuytten, N.; Pisanic, T. R.; Ferrari, A.; De Cuyper, M. Intracellular nanoparticle coating stability determines nanoparticle diagnostics efficacy and cell functionality. *Small* **2010**, *6*, 2136-2145.

[93] Heller, D. A.; Sharma, R.; Strano, M. S. Size-Dependent Cellular Uptake and Expulsion of Single-Walled Carbon Nanotubes: Single Particle Tracking and a Generic Uptake Model for Nanoparticles. ACS Nano, 2009, 3, 149-158.

[94] Herd, H.; Daum, N.; Jones, A. T.; Huwer, H.; Ghandehari, H.; Lehr, C. M. Nanoparticle geometry and surface orientation influence mode of cellular uptake. *ACS Nano* **2013**, *7*, 1961-1973.

[95] Verma, A.; Uzun, O.; Hu, Y.; Hu, Y.; Han, H. S.; Watson, N.; Chen, S.; Irvine, D. J.; Stellacci, F. Surface-structure-regulated cell-membrane penetration by monolayer-protected nanoparticles. *Nat. Mater*. **2008**, *7*, 588-595.

[96] Verma, A.; Stellacci, F. Effect of surface properties on nanoparticle–cell interactions. *Small*, **2010**, *6*, 12-21.

[97] Hamada, T.; Morita, M.; Miyakawa, M.; Sugimoto, R.; Hatanaka, A.; Vestergaard, M. C.; Takagi, M. Size-dependent partitioning of nano/microparticles mediated by membrane lateral heterogeneity. *J. Am. Chem. Soc*. **2012**, *134*, 13990-13996.

[98] Fujiwara, T.; Akita, H.; Harashima, H. Intracellular fate of octaarginine-modified liposomes in polarized MDCK cells. *Int. J. Pharm*. **2010**, *386*, 122-130.

[99] Kim, J. A.; Åberg, C.; Salvati, A.; Dawson, K. A. Role of cell cycle on the cellular uptake and dilution of nanoparticles in a cell population. Nat. Nanotech. 2012, 7, 62-68.

[100] Polyak, K. Heterogeneity in breast cancer. The Journal of Clinical Investigation 2011, 121, 3786-3788.

[101] Perez, E. A. Breast cancer management: opportunities and barriers to an individual approach. *Oncologist* **2011**, *16*, 20-22.

[102] Sorlie, T.; Perou, C. M.; Tibshirani, R.; Aas, T.; Geisler, S.; Johnsen, H.; Hastie, T.; Eisen, M. B.; van de Rijn, M.; Jeffrey, S. S.; Thorsen, T.; Quist, H.; Matese, J. C.; Brown, P. O.; Botstein, D.; Lønning, P. E.; Børresen-Dale, A. L. Gene expression patterns of breast carcinomas distinguish tumor subclasses with clinical implications. *Proc. Natl. Acad. Sci. U.S.A*., **2001**, *98*, 10869-10874.

[103] Perou, C. M.; Sørlie, T.; Eisen, M. B.; van de Rijn, M.; Jeffrey, S. S.; Rees, C. A.; Pollack, J. R.; Ross, DT.; Johnsen, H.; Akslen, L. A., Fluge, O.; Pergamenschikov, A.; Williams, C.; Zhu, S. X.; Lønning, P. E.; Børresen-Dale, A. L.; Brown, P. O.; Botstein, D. Molecular portraits of human breast tumors. *Nature* **2000**, *406*, 747-752.

[104] Hynes, N. E.; Lane, H. A. ERBB receptors and cancer: the complexity of targetedinhibitors. *Nat Rev Cancer* **2005**, *5*, 341–354.

[105] Burgess, A. W.; Cho, H. S.; Eigenbrot, C.; Ferguson, K. M.: Garrett, T. P. J.; Leahy, D. J.; et al. An open-and-shut case? Recent insights into the activation of EGF/ErbB receptors. *Mol Cell* **2003**, *12*, 541–552.

[106] Garrett, T. P.; McKern, N. M.; Lou, M.; Elleman, T. C.; Adams, T. E.; Lovrecz, G. O.; et al. The crystal structure of truncated ErbB2 ectodomain reveals an active conformation, poised to interact with other ErbB receptors. *Mol Cell* **2003**, *11*, 495–505.

[107] Citri, A.; Yarden, Y. EGF-ERBB signalling: towards the system level. *Nat Rev Mol Cell Biol* **2006**, *7*, 505–516.

[108] Sharma, S. V.; Settleman, J. ErbBs in lung cancer. *Exp Cell Res* **2009**, *315*, 557–571.

[109] Wieduwilt, M. J.; Moasser, M. M. The epidermal growth factor receptor family: biology driving targeted therapeutics. *Cell Mol Life Sci* **2008**, *65*, 1566–1584.è

[110] Faltus, T.; Yuan, J.; Zimmer, B.; Kramer, A.; Loibl, S.; Kaufmann, M.; et al. Silencing of the HER2/neu gene by siRNA inhibits proliferation and induces apoptosis in HER2/neu-overexpressing breast cancer cells. *Neoplasia*, **2004**, *6*, 786-795.

[111] Shukla, R.; Thomas, T. P.; Peters, J. L.; Desai, A. M.; Kukowska-Latallo, J.; Patri, A. K.; et al. HER2 specific tumor targeting with dendrimer conjugated anti-HER2 mAb. *Bioconjugate Chem* **2006**, *17*, 1109-1115.

[112] Cantero, D.; Friess, H.; Deflorin, J.; Zimmermann, A.; Bru¨ndler, M. A.; Riesle, E.;

Korc, M.; Bu¨chler, M. W. Enhanced expression of urokinase plasminogen activator and its receptor in pancreatic carcinoma. *Br. J. Cancer* **1997**, *75*, 388–395.

[113] Costantini, V.; Sidoni, A.; Deveglia, R.; Cazzato, O. A.; Bellezza, G.; Ferri, I.; Bucciarelli, E.; Nenci, G. G. Combined overexpression of urokinase, urokinase receptor, and plasminogen activator inhibitor-1 is associated with breast cancer progression - An immunohistochemical comparison of normal, benign, and malignant breast tissues. *Cancer* **1996***, 77*, 1079–1088.

[114] Gavrilov, D.; Kenzior, O.; Evans, M.; Calaluce, R.; Folk, W. R. Expression of urokinase plasminogen activator and receptor in conjunction with the ets family and AP-1 complex transcription factors in high grade prostate cancers. *Eur. J. Cancer* **2001***, 37*, 1033–1040.

[115] Andreasen, P. A.; Sottrupjensen, L.; Kjøller, L.; Nykjaer, A., Moestrup, S. K.; Petersen, C. M.; Gliemann, J. Receptor-mediated endocytosis of plasminogen activators and activator/inhibitor complexes. *FEBS Lett.* **1994***, 338*, 239–245.

[116] Danø, K.; Behrendt, N.; Høyer-Hansen, G.; Johnsen, M.; Lund, L. R.; Ploug, M.; Romer, J. Plasminogen activation and cancer. *Thromb. Haemost.* **2005***, 93*, 676–681.

[117] Behrendt, N. The urokinase receptor (uPAR) and the uPAR-associated protein (uPARAP/Endo180): membrane pro- teins engaged in matrix turnover during tissue remodeling. *Biol. Chem.* **2004***, 385*, 103–136.

[118] Myo¨ha¨nen, H.; and Vaheri, A. Regulation and interac- tions in the activation of cell-associated plasminogen. *Cell. Mol. Life Sci.* **2004***, 61*, 2840–2858.

[119] Blasi, F.; and Carmeliet, P. uPAR: a versatile signalling orchestrator. *Nat. Re*V*. Mol. Cell. Biol.* **2002***, 3*, 932–943.

[120] Andreasen, P. A.; Egelund, R.; and Petersen, H. H. The plasminogen activation system in tumor growth, invasion, and metastasis. *Cell. Mol. Life Sci.* **2000***, 57*, 25–40.

[121] Stoppelli, M. P.; Corti, A.; Soffientini, A.; Cassani, G., Blasi, F.; Assoian, R. K. Differentiation-enhanced binding of the amino-terminal fragment of human urokinase plasminogen- activator to a specific receptor on U937 monocytes. *Proc. Natl. Acad. Sci. U.S.A.* **1985***, 82*, 4939–4943.

[122] Hansen, A. P.; Petros, A. M.; Meadows, R. P.; Nettesheim, D. G.; Mazar, A. P.; Olejniczak, E. T.; Xu, R. X.; Pederson, T. M.,;Henkin, J.; Fesik, S. W. Solution structure of the amino-terminal fragment of urokinase-type plasminogen activator. *Biochemistry* **1994***, 33*, 4847–4864.

[123] Llinas, P.; Le Du, M. H.; Gårdsvoll, H.; Danø, K.; Ploug, M.; Gilquin, B.; Stura, E. A.; Me´nez, A. Crystal structure of the human urokinase plasminogen activator receptor bound to an antagonist peptide. *EMBO J.* **2005***, 24*, 1655–1663.

[124] Fetrow, J. S. Omega loops: nonregular secondary structures significant in protein function and stability. *FASEB J.* **1995***, 9*, 708–717.

[125] Huai, Q.; Mazar, A. P.; Kuo, A.; Parry, G. C.; Shaw, D. E.; Callahan, J.; Li, Y.; Yuan, C.; Bian, C.; Chen, L.; Furie, B.; Furie, B. C.; Cines, D. B.; Huang, M. Structure of human urokinase plasminogen activator in complex with its receptor. *Science* **2006***, 311*, 656–659.

[126] Thanou, M.; Kean, T. *Proc. Int. Symp. Controlled Release BioactiVe Mat. Controlled Release Soc. Vienna* **2006***,* 677.

[127] Medintz, I. Universal tools for biomolecular attachment to surfaces. *Nature* **2006**, *5*, 842.

[128] Torcello-Gomez. A.; et al. Adsorption of antibody onto Pluronic F68-covered nanoparticles: link with surface properties. *Soft Matter* **2011**, *7*, 8450-8461.

[129] Anand, G.; Sharma, S.; Dutta, A. K.; Kumar, S. K.; Belfort, G. Conformational transitions of adsorbed proteins on surfaces of varying polarity. *Langmuir* **2010**, *26*, 10803-10811.

[130] Apicella, A.; Soncini, M.; Deriu, M. A.; Natalello, A.; Bonanomi, M.; Dellasega, D.; Tortora, P.; Regonesi, M. E.; Casari, C. S. hydrophobic gold surface triggers misfolding and aggregation of the amyloidogenic Josephin domain in monomeric form, while leaving the oligomers unaffected. *PLoS ONE* **2013**, *8*, 1-8.

[131] Shang, W.; Nuffer, J. H.; Dordick, J. S.; Siegel, R. W. Unfolding of ribonuclease A on silica nanoparticle surfaces. *Nano Lett*. **2007**, *7*, 1991-1995.

[132] Shemetov, A. A.; Nabiev, I.; Sukhanova, A. Molecular interaction of proteins and peptides with nanoparticles. *ACS Nano* **2008**, *6*, 4585-4602.

[133] Chithrani, B. D.; Chan, W. C. Elucidating the mechanism of cellular uptake and removal of protein-coated gold nanoparticles of different sizes and shapes. *Nano Lett*. **2007**, *7*, 1542-1550.

[134] Mahon, E.; Salvati, A.; Baldelli Bombelli, F.; Lynch, I.; Dawson, K. A. Designing the nanoparticle-biomolecule interface for targeting and therapeutic delivery. *J. Control. Release* **2012**, *161*, 164-174.

[135] Sapsford, K. E.; Algar, W. R.; Berti, L.; Gemmill, K. B.; Casey, B. J.; Oh, E.;

Stewart, M. H.; Medintz, I. L. Functionalizing nanoparticles with biological molecules: developing chemistries that facilitate nanotechnology. *Chem. Rev*. **2012**, *113*, 1904-2074.

[136] Kabashin, A. V.; Evans, P.; Pastkovsky, S.; Hendren, W.; Wurtz, G. A.; Atkinson, R.; Pollard, R.; Podolskiy, V. A.; Zayats, A. V. Plasmonic nanorod metamaterials for biosensing. *Nat. Mater*. **2006**, *8*, 867-871.

[137] Tannous, B. A.; Grimm, J.; Perry, K. F.; Chen, J. W.; Weissleder, R.; Breakefield, X. O. Metabolic biotinylation of cell surface receptors for in vivo imaging. *Nat. Methods* **2004**, *3*, 391-396.

[138] Yang, L.; Mao, H.; Wang, Y. A.; Cao, Z.; Peng, X.; Wang, X.; Duan, H.; Ni, C.; Yuan, Q.; Adams, G.; Smith, M. Q.; Wood, W. C.; Gao, X.; Nie, S. Single chain epidermal growth factor receptor antibody conjugated nanoparticles for in vivo tumor targeting and imaging. *Small* **2009**, *5*, 235-243.

[139] Mazzucchelli, S.; Sommaruga, S.; O'Donnell, M.; Galeffi, P.; Tortora, P.; Prosperi, D.; Colombo, M. Dependence of nanoparticle.cell recognition efficiency from surface orientation of scFv targeting ligands. *Biomater. Sci*. **2013**, *1*, 1728-735.

[140] Leung, M. K. M.; Hagemeyer, C. E.; Johnston, A. P.; Gonzales, C.; Kamphuis, M. M.; Ardipradja, K.; Such, G. K.; Peter, K.; Caruso, F. Bio-click chemistry: enzymatic functionalization of PEGylated capsules for targeting applications. *Angew. Chem. Int. Ed. Engl*. **2012**, *51*, 7132-7136.

[141] Park, J.; An, K.; Hwang, Y.; Park, J.G.; Noh, H.-J.; Kim, J.-Y. Park, J.-H.; Hwang, N.-M.; Hyeon, T. Ultra-large-scale syntheses of monodisperse nanocrystals. *Nat. Mater.* **2004**, *3*, 891-895.

[142] Lin, C.-A. J.; Sperling, R. A.; Li, J. K.; Yang, T.-Y.; Li, P.-Y.; Zanella, M.; Chang, W. H.; Parak, W. J. Design of an Amphiphilic Polymer for Nanoparticle Coating and Functionalization. *Small* **2008**, *4*, 334-341.

[143] Turkevich, J.; Stevenson, P. C.; and Hiller, J. A study of the nucleation and growth processes in the synthesis of colloidal gold. *Discuss. Faraday Soc.* **1951**, *11*, 55-75

[144] Frens, G. Controlled Nucleation for the Regulation of the Particle Size in Monodisperse Gold Suspensions. *Nat.-Phys. Sci.* **1973**, *241*, 20-22.

[145] Haiss, W.; Thanh, N. T. K.; Aveyard, J.; Fernig, D. G. Determination of size and concentration of gold nanoparticles from UV-vis spectra. *Anal. Chem*. 2007, **79**, 4215-4221.

[146] Sommaruga, S.; Lombardi, A.; Salvadè, A.; Mazzucchelli, S.; Corsi, F.; Galeffi, P.; Tortora, P.; Prosperi D. Highly efficient production of anti-HER2 scFv antibody variant for targeting breast cancer cells. *Appl. Microbiol. Biotechnol.* **2011**, *91*, 613-621.

[147] Levy, R.; Thanh, N. T. K.; Doty, R. C.; Hussain, I.; Nichols, R. J.; Schiffrin, D. J.; Brust, M.; Fernig, D. G. Rational and combinatorial design of peptide capping Ligands for gold nanoparticles. *J. Am. Chem. Soc.* **2004**, *126*, 10076-10084.

[148] Colombo, M.; Corsi, F.; Foschi, D.; Mazzantini, E.; Mazzucchelli, S.; Morasso, C.; Occhipinti, E.; Polito, L.; Prosperi, D.; Ronchi, S.; Verderio, P. HER2 targeting as a two-sided strategy for breast cancer diagnosis and treatment: outlook and recent implications in nanomedical approaches. *Pharmacol. Res.* **2010**, *62*, 150-165.

[149] Plosker, G. L.; Keam, S. J. Extended-release intramuscular naltrexone. *Drugs* **2006**, 66, 449-475.

[150] Polito, L.; Colombo, M.; Monti, D.; Melato, S.; Caneva, E.; Prosperi, D. Resolving the structure of ligands bound to the surface of superparamagnetic iron oxide nanoparticles by high-resolution magic-angle spinning NMR spectroscopy. *J. Am. Chem. Soc*. **2008**, *130*, 12712-12724.

[151] Corsi, F.; De Palma, C.; Colombo, M.; Allevi, R.; Nebuloni, M.; Ronchi, S.; Rizzi, G.; Tosoni, A.; Trabucchi, E.; Clementi, E.; Prosperi, D. Towards ideal magnetofluorescent nanoparticles for bimodal detection of breast-cancer cells. *Small* **2009**, *5*, 2555-2564.

[152] Sun, C.; Du, K.; Fang, C.; Bhattari, N.; Veiseh, O.; Kievit, F.; Stephen, Z.; Lee, D.; Ellenbogen, R. G.; Ratner, B.; Zhang, M. PEG-Mediated Synthesis of Highly Dispersive Multifunctional Superparamagnetic Nanoparticles: Their Physicochemical Properties and Function In Vivo. *ACS Nano* **2010**, *4*, 2402-2410.

[153] Hu, F.; Wei, L.; Zhou, Z.; Ran, Y.; Li, Z.; Gao, M. Preparation of Biocompatible Magnetite Nanocrystals for In Vivo Magnetic Resonance Detection of Cancer. *Adv. Mater.* **2006**, *18*, 2553-2556.

[154] Lin, W.; Garnett, M. C.; Schacht, E.; Davis, S. S.; Illum, L. Preparation and in vitro characterization of HAS-mPEG nanoparticles. *Int. J. Pharm*. **1999**, *189*, 161-170.

[155] Susi, H.; Byler, D. M. Examination of the secondary structure of proteins by deconvolved FTIR spectra. *Methods. Enzymol.* **1986**, *130*, 290-311.

[156] Arrondo, J. L. R.; Goni, F. M. Structure and dynamics of membrane proteins as studied by infrared spectroscopy. *Prog. Biophys. Mol. Biol*. **1999**, *72***,** 367-405.

[157] Natalello, A.; Ami, D.; Brocca, S.; lotti, M.; Doglia, S. M. Secondary structure, conformational stability and glycosylation of a recombinant Candida rugosa lipase studied by Fourier-transform infrared spectroscopy. *Biochem. J*. **2005**, *385*, 511-517.

[158] Yustle, L.; Montero, J. C.; Esparís-Ogando, A.; pandiella, A. Stimulation of cleavage of membrane proteins by calmodulin inhibitors. *Cancer Res*. **2005**, *65*, 6801-6810.

[159] Park, K.; Lee, S.; Kang, E.; Kim, K.; Choi, K.; Kwon, I. C. New generation of multifunctional nanoparticles for cancer imaging and therapy. *Adv. Funct. Mater*. **2009**, *19*,1553-1566.

[160] Lee, J.-H.; Huh, Y.-M.; Jun, Y.-w.; Seo, Y.-w.; Jang, J.-t.; Song, H.-T.; Kim., S.; Cho, E.-J.; Yoon, H.-G.; Suh, J.-S.; Cheon, J. Artificially engineered magnetic nanoparticles for ultra-sensitive molecular imaging. *Nat. Med*. **2007**, *13*, 95-99.

[161] Kim, J.; Park, S.; Lee, J. E.; Jin, S. M.; Lee, J. H.; Lee, I. S.; Yang, I.; Kim, J.-S.; Kim, S. K.; Cho, M.-H.; Hyeon, T. Designed fabrication of multifunctional magnetic gold nanoshells and their application to magnetic resonance imaging and photothermal therapy**.** *Angew. Chem*. **2006**, *118*, 7918-7922.

[162] Lewin, M.; Carlesso, N.; Tung, C.-H.; Tang, X.-W.; Cory, D.; Scadden, D. T.; Weissleder, R. Tat peptide-derivatized magnetic nanoparticles allow in vivo tracking and recovery of progenitor cells. *Nat. Biotachnol*. **2000**, *18*, 410-414.

[163] Thanh, N. T. K.; Green, L. A. W. Functionalisation of nanoparticles for biomedical applications. *Nano Today* **2010**, *5*, 213-230.

[164] Haun, J. B.; Devaraj, N. K.; Hilderbrand, S. A.; Lee, H.; Weissleder, R. Bioorthogonal chemistry amplifies nanoparticle binding and enhances the sensitivity of cell detection. *Nat. Nanotechnol*. **2010**, *5*, 660-665.

[165] Mazzucchelli, S.; Colombo, M.; De Palma, C.; Salvadè, A.; Verderio, P.; Coghi, M. D.; Clementi, E.; Tortora, P.; Corsi, F.; Prosperi, D. Single-domain protein A-engineered magnetic nanoparticles: toward a universal strategy to site-specific labeling of antibodies for targeted detection of tumor cells. *ACS Nano* **2010**, *4*, 5693-5702.

[166] Montenegro, J.-M.; Grazu, V.; Sukhanova, A.; Agarwal, S.; de la Fuente, J. M.; Nabiev, I.; Greiner, A.; Parak, W. J. Controlled antibody/(bio-)conjugation of inorganic nanoparticles for targeted delivery. *Advanced Drug Delivery Reviews* **2013**, *65*, 677-688.

[167] Xu, C.; Xu, K.; Gu, H.; Zhong, X.; Guo, Z.; Zheng, R.; Zhang, X.; Xu, B. Nitrilotriacetic acid-modified magnetic nanoparticles as a general agent to bind histidine-tagged proteins *J. Am. Chem. Soc*. **2004**, *126*, 3392-3393.

[168] Long, M. J. C.; Pan, Y.; Lin H.-C.; Hedstrom, L.; Xu, B. Cell compatible trimethoprim-decorated iron oxide nanoparticles bind dihydrofolate reductase for magnetically modulating focal adhesion of mammalian cells. *J. Am. Chem. Soc*. **2011**, *133*, 10006-10009.

[169] Colombo, M.; Mazzucchelli, S.; Montenegro, J.-M.; Galbiati, E.; Corsi, F.; Parak, W. J.; Prosperi, D. Protein oriented ligation on nanoparticles exploiting O6-alkylguanine-DNA transferase (SNAP) genetically encoded fusion. *Small* **2012**, *8*, 1492-1497.

[170] Mazzucchelli, S.; Colombo, M.; Verderio, P.; Rozek, E.; Andreata, F.; Galbiati, E.; Tortora, P.; Corsi, F.; Prosperi, D. Orientation-controlled conjugation of haloalkane dehalogenase fused homing peptides to multifunctional nanoparticles for the specific recognition of cancer cells. *Angew. Chem. Int. Ed*. **2013**, *52*, 3121-3125.

[171] Hodneland, C. D., Lee, Y.-S.; Min, D.-H.; Mrksich, M. Selective immobilization of proteins to self-assembled monolayers presenting active site-directed capture ligands. *PNAS* **2002**, *99*, 5048-5052.

[172] Los, G. V.; Encell, L. P.; McDougall, M. G.; Hartzell, D. D.; Karassina, N.; Zimprich, C.; Wood, M. G.; Learish, R.; Ohana, R. F.; Urh, M.; Simpson, D.; Mendez, J.; Zimmerman, K.; Otto, P.; Vidugiris, G.; Zhu, J.; Darzins, A.; Klaubert, D. H.; Bulleit, R. F.; Wood, K. V. HaloTag: a novel protein labeling technology for cell imaging and protein analysis. *ACS Chem. Biol*. **2008**, *3*, 373-382.

[173] M. Wang, D. W. P. M. Löwik, A. D. Miller, M. Thanou, Targeting the urokinase plasminogen activator receptor with synthetic self-assembly nanoparticles. *Bioconjugate Chem*. **2009**, *20*, 32-40.

[174] Danhier, F.; Le Breton, A.; Préat, V. RGD-Based strategies to target alpha(v) beta(3) integrin in cancer therapy and diagnosis. *Mol. Pharm.* **2012**, *9*, 2961-2973.

[175] Hoffman, J. A.; Laakkonen, P.; Porkka, K.; Bernasconi, M.; Ruoslahti, E. In vivo and ex vivo selections using phage-displayed libraries, in Phage Display ed. T. Clackson and H. B. Lowman, *Oxford University Press, Oxford*, UK, **2004**, *266*, 171-192.

[176] Pasqualini, R.; Ruoslahti, E. Organ targeting in vivo using phage display peptide libraries. *Nature*, **1996**, *380*, 364-366.

[177] Arap, W.; Pasqualini, R.; Ruoslahti, E. Cancer treatment by targeted drug delivery to tumor vasculature in a mouse model. *Science*, **1998**, *279*, 377-380.

[178] Lee, M. H.; Kim, J.; Han, J. H.; Bhuniya, S., Sessler, J. L., Kang, C., and Seung Kim, J. Direct fluorescence monitoring of the delivery and cellular uptake of a cancer-targeted RGD peptide-appended naphthalimide theragnostic prodrug. *J. Am. Chem. Soc.* **2012**, *30*, 12668–12674.

[179] Park, J.; Singha, K.; Son, S.; Kim, J.; Namgung, R.; Yun, C.-O.; Kim, W. J. A review of RGD-functionalized nonviral gene delivery vectors for cancer therapy. *Cancer Gene Ther.* **2012**, *19*, 741-748.

[180] Ma, Y. Y.; Tao, H. Q. Role of urokinase plasminogen activator receptor in gastric cancer: a potential therapeutic target. *Cancer Biother. Radiopharm*. **2012**, *27*, 285-290.

[181] Bhattacharyya, S.; Singh, R. D.; Pagano, R.; Robertson, J. D.; Bhattacharya, R.; Mukherjee, P. Switching the targeting pathways of a therapeutic antibody by nanodesign. *Angew. Chem. Int. Ed.* **2012**, *51*, 1563-1567.

[182] Huang, Y.-F.; Liu, H.; Xiong, X.; Chen, Y.; Tan, W. Nanoparticle-mediated IgE-receptor aggregation and signaling in RBL mast cells. *J. Am. Chem. Soc.* **2009**, *131*, 17328-17334.

[183] Häkkinen, H. The gold–sulfur interface at the nanoscale. *Nat. Chem*. **2012**, *4*, 443-455.

[184] Hosta-Rigau, L.; Olmedo, I.; Arbiol, J.; Cruz, L. J.; Kogan, M. J.; Albericio, F. Multifunctionalized gold nanoparticles with peptides targeted to gastrin-releasing peptide receptor of a tumor cell line. *Bioconjugate Chem*. **2010**, *21*, 1070-1078.

[185] Kapoor, P.; Singh, H.; Gautam, A.; Chaudhary, K.; Kumar, R.; Raghava, G. P. S. TumorHoPe: a database of tumor homing peptides. *PlosOne* **2012**, *7*, e35187.

[186] Shadidi, M.; Sioud, M. Identification of novel carrier peptides for the specific delivery of therapeutics into cancer cells. *The FASEB Journal* **2003**, *17*, 256-258.

[187] Jie, L.-Y.; Cai, L.-L.; Wang, L.-J.; Ying, X.-Y.; Yu, R.-S.; Zhang, M.-M.; Du, Y.-Z. Actively-targeted LTVSPWY peptide-modified magnetic nanoparticles for tumor imaging. *International Journal of Nanomedicine* **2012**, *7*, 3981-3289.

[188] Ahmed, S.; Matthews, A. S.; Byeon, N.; Lavasanifar, A.; Kaur, K. Peptide arrays for screening cancer specific peptides. *Anal. Chem*. **2010**, *82*, 7533-7541.

[189] Matthews, A. S.; Ahmed, S.; Shanin, M.; Lavasanifar, A.; Kaur, K. Peptide modified polymeric micelles specific for breast cancer cells. *Bioconjugate Chem*. **2013**, *24*, 560-570.

[190] Ulman, A. Formation and structure of self-assembled monolayers. *Chem. Rev.* **1996**, *96*, 1533–1554.

List of personal publications

Verderio, P.; Avvakumova, S.; Alessio, G.; Bellini, M.; Colombo, M.; Galbiati, E.; Mazzucchelli, S.; Peñaranda Avila, J.; Santini, B.; Prosperi. D. Delivering colloidal nanoparticles to mammalian cells: a nano-bio interface perspective. *Adv. Healthcare Mat.* **2014**, DOI: 10.1002/adhm.201300602.

Mazzucchelli, S.; Colombo, M., Verderio, P.; Rozek, E.; Andreata, F.; Galbiati, E.; Tortora, P.; Corsi, F.; Prosperi, D. Orientation-controlled conjugation of HALO-fused homing peptides to multifunctional nanoparticles for specific recognition of cancer cells. *Angew. Chem. Int. Ed.* **2013**, *52*, 3121-3125.

Colombo, M.; Mazzucchelli, S.; Montenegro, J. M.; Galbiati, E.; Corsi, F.; Parak, W. J.; Prosperi, D. Protein oriented ligation on nanoparticles exploiting O_6-alkylguanine-DNA transferase (SNAP) genetically encoded fusion. *Small* **2012**, *8*, 1492-1497.

Occhipinti, E.; Verderio, P.; Natalello, A.; Galbiati, E.; Colombo, M.; Mazzucchelli, S.; Tortora, P.; Doglia, S. M.; Prosperi, D. Investigating the structural biofunctionality of antibodies conjugated to magnetic nanoparticles. *Nanoscale* **2011**, *3*, 387-390.

Acknowledgments

I wish to thank prof. Paolo Tortora and dott. Paolo Prosperi for supervising my work, always with a lot of patience. Their support gave me a passion and a self-confidence that led me to this important result.

I also wish to thank all of the NanoBioLab for help and kindness of these years.